Three-dimensional Quantitative Magnetic Resonance Imaging of Carotid Atherosclerotic Plaque

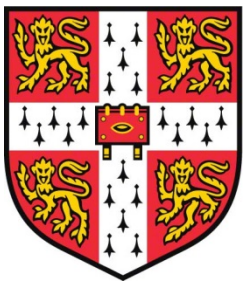

Jianmin Yuan

Hughes Hall

This dissertation is submitted for the degree of Doctor of Philosophy

Department of Radiology

University of Cambridge

May 2017

Declaration

I hereby declare that this dissertation is the result of my own work and includes nothing which is the outcome of work done in collaboration with others, except as specified in the text and Acknowledgements. The contents of this dissertation are original and have not been submitted in whole or in part for consideration for any other degree or qualification at the University of Cambridge or any other institution.

This dissertation contains fewer than 60,000 words, excluding figures, tables, equations and bibliography.

Acknowledgement

I gratefully thank my supervisor, Professor Jonathan Gillard, for his constant support, guidance and encouragement during my PhD, for his expertise in biomechanics, MRI, clinical and non-academic matters. Jonathan provided a friendly and very resourceful research environment for the people to work within the neuroradiology group. His knowledge in the field of radiology, language and management always made the work so inspiring.

I am thankful for Martin Graves and Andrew Patterson for the supervision, mentorship, support, and encouragement during the MRI work. Their broad knowledge of MR physics, sequence programming and statistics made me confident in facing the challenges and exploring new research arenas. The hours and days of discussion and preparing the manuscripts make me so proud to be associated with and work in this friendly and encouraging MRIS Unit (Magnetic Resonance Imaging and Spectroscopy Unit, on the Cambridge Biomedical Campus). They encouraged me to do my best, advised and supported me through the challenging times, such as dealing with referees' comments, technical malfunctions of the scanner, or especially, many other things in career and life. Martin's enthusiasm of the work and the pursuit of perfection was invaluable. His mastership of presentation and communication fostered an exceptional learning environment. Similarly, Andrew's knowledge and expertise of MRI physics and statistics provided me with invaluable assistants.

Ammara Usman, Sarah Hilborne, Jackie Mason and Gregory Makris worked tiredlessly recruiting patients for various clinical studies. Additionally, Ammara contributed to the interobserver measurements and gave me valuable feedback for various manuscrips. Her wide knowledge of clinical medicine enabled me to understand the clinical aspects of this research. Her earnestness and perseverance always inspires me.

Pascal Ruetten performed some of the volunteer studies together with me. The frequent discussions with him about pulse sequence programming and image reconstructions were great help for me.

I am grateful for Zhongzhao Teng's supervision of the biomechanics work that contributed to the first year report. Thanks to Yuan Huang, Shuo Wang, Jing He and Jyh-Miin Lin for their friendship and discussions, many of which occur over the hotpot in these years. Thanks to

Wafa Abutaleb, Aziz Tokgoz, Windy Phillips and all the other people in the Neuroimaging group for their helpful discussion, teamwork and friendship.

Tilak Das helped in the ulceration observation in the dynamic contrast-enhanced study in Chapter 3. He also gave valuable comments for the ulceration review manuscript included in the Chapter 1. I am grateful for his advice during the study and manuscript preparation.

It was a great pleasure to work with other MR physicists in the department. I am indebted to Andrew Priest, Andrew Gill, Joshua Kaggie, Richard Black, Frank Riemer and Hao Li. Their experience and knowledge about pulse sequence programming, post-process modelling, image reconstruction and computer languages helped me understand the work in much more depth.

Scott Reid (seconded to Cambridge from GE Healthcare) helped to implement the compressed sensing features used in Chapter 4 and 5. I am indebted to Scott for his experience and discussion in pulse sequence development.

All of the phantom, volunteer and patient studies were conducted in the MRIS Unit. This cannot have been achieved without the generous and friendly help from the Ilse Patterson, Dario Prudencio and all the other radiographers.

The amicable and harmonious environment created by the other PhD students and researchers within the Department, including Tess Wallace, Reem Bedair, Roido Manavaki, Surrin Deen, James Grist, Julia Carmona-Bozo, Laura Lechermann, Charlie Daniels, Jamie MacKay, Ayla Selamoglu and Fulvio Zaccagna contributed to the positive academic eco-system.

I would also thank the support staff in the Department of Radiology, Candice Anderson, Simone Matias Vegh, Catherine Munn, Anna Rygielska and Ralph Ball. Their generous help and coordination made the administration of this project so pleasant.

I also greatly appreciate the support of my College tutor, Jean Lambert, for her support throughout my PhD in Cambridge.

Lastly but most importantly, I am so grateful to my parents Shengliu Yuan, Binyu Huang, and additionally, Chen Weng, for their relentless support during these four years. Without you, none of this is possible.

Summary

Stroke is one of the leading causes of death and disability worldwide with 20% of ischemic strokes attributed to carotid atherosclerosis.

In recent years, morphological characteristics of atherosclerotic plaque such as a thin fibrous cap, large lipid-rich necrotic core, intraplaque haemorrhage and ulceration have shown correlations with subsequent clinical events. High resolution, multi-contrast magnetic resonance imaging (MRI) can qualitatively identify these features and monitor disease progression. Compared to traditional contrast weighted imaging, quantitative MRI could provide an objective assessment of disease. Therefore, the general *hypothesis* investigated in this thesis is:

Quantitative MRI methods can be used to acquire objective biomarkers of carotid vessel wall and atherosclerotic plaque, with high accuracy and good repeatability.

The research presented in this thesis describes the use of multiple quantitative MRI methods to evaluate the carotid vessel wall. These include dynamic contrast-enhanced (DCE) MRI analysis for the assessment of plaque inflammation/neovascularization and the development of black-blood quantitative T_2/T_2* mapping sequences for plaque component characterisation. The acceleration of the sequences was also investigated using a combination of compressed sensing (CS) and parallel imaging (PI).

Chapter 3 investigated the hypothesis that plaque functional characteristics and surface morphology can be evaluated using a high temporal and spatial resolution 4D contrast-enhanced MRI/MR angiography (MRA) sequence. Chapter 4 tested the hypothesis that magnetisation prepared 3D fast-spin-echo (FSE) is the best sequence for in vivo T_2 mapping. Four different black-blood T_2 mapping sequences were developed and compared in phantom and volunteers. Chapter 5 tested the hypothesis that the optimised iMSDE 3D FSE T_2 mapping sequence can be combined with CS and PI to further reduce the acquisition time without significantly affecting image quality and the measured T_2 relaxation times. Chapter 6 investigated the hypothesis that compressed sensing can be used to reduce the overall examination time of a comprehensive multi-contrast MRI protocol, comprising black-blood T_1 weighted, T_2 weighted and proton density weighted sequences. Finally, Chapter 7

investigated the hypothesis that accurate 3D vessel wall R_2* mapping can be achieved through black-blood preparation.

In summary, this thesis investigated the use of multiple quantitative MRI methods in evaluating the carotid vessel wall and atherosclerotic plaque. The results demonstrate that quantitative MRI is an accurate and reproducible method for the carotid plaque characterization.

Publications

Primarily manuscripts

1. **Yuan J**, Usman A, Reid SA, King KF, Patterson AJ, Gillard JH and Graves MJ. “Three-dimensional black-blood T_2 mapping with compressed sensing and data-driven parallel imaging in the carotid artery”. *Magnetic Resonance Imaging* 2017, 37:62-69.
2. **Yuan J**, Usman A, Das T, Patterson AJ, Gillard JH and Graves MJ. "Imaging carotid atherosclerosis plaque ulceration: comparison of advanced imaging modalities". *American Journal of Neuroradiology* 2017, 38(4):664-671.
3. **Yuan J**, Makris G, Patterson AJ, Usman A, Das T, Priest AN, Teng Z, Hilborne S, Prudencio D, Gillard JH and Graves MJ. "Relationship between carotid plaque surface morphology and perfusion: a 3D DCE-MRI study". Magnetic Resonance Materials in Physics, Biology and Medicine 2017, 1-9.
4. **Yuan J**, Usman A, Reid SA, King KF, Patterson AJ, Gillard JH and Graves MJ. “Three-dimensional black-blood multi-contrast protocol for carotid imaging using compressed sensing: a repeatability study”. (under review)
5. **Yuan J**, Patterson AJ, Ruetten PPR, Reid SA, Gillard JH and Graves MJ. “Comparison of black blood T_2 mapping sequences in carotid artery at 3T”. (under review)
6. **Yuan J**, Graves MJ, Patterson AJ, Priest AN, Ruetten PPR, Usman A and Gillard JH. “The development and optimisation of 3D black-blood R_2^* mapping of the carotid artery wall”. (under review)

Secondary manuscripts

7. **Yuan J**, Teng Z, Feng J, Zhang Y, Brown AJ, Gillard JH, Jing Z, Lu Q. "Influence of material property variability on the mechanical behaviour of carotid atherosclerotic plaques: A 3D fluid structure interaction analysis". *International journal for numerical methods in biomedical engineering* 2015, 31(8).
8. Teng Z, **Yuan J**, Feng J, Zhang Y, Brown AJ, Wang S, Lu Q, Gillard JH. "The influence of constitutive law choice used to characterise atherosclerotic tissue material properties on computing stress values in human carotid plaques". *Journal of Biomechanics* 2015, 48(14): 3912-3921.

9. Teng Z, Zhang Y, Huang Y, Feng J, **Yuan J**, Lu Q, Sutcliffe MPF, Brown AJ, Jing Z and Gillard JH. "Material properties of components in human carotid atherosclerotic plaques: A uniaxial extension study". *Acta biomaterialia* 2014, 10(12): 5055-5063.
10. Zhu C, Graves M, **Yuan J**, Sadat U, Gillard JH and Patterson AJ. "Optimization of Improved Motion-sensitized Driven-equilibrium (iMSDE) blood suppression for carotid artery wall imaging". *Journal of Cardiovascular Magnetic Resonance* 2014, 16: 61.

Primarily abstracts

1. **Yuan J**, Makris G, Patterson AJ, Usman A, Das T, Priest AN, Teng Z, Hilborne S, Prudencio D, Gillard JH and Graves MJ. "Combined High Resolution, Four Dimensional, CE-MRA and DCE-MRI of Carotid Atherosclerotic Plaque". ISMRM 24th Annual meeting, Singapore, 2016.
2. **Yuan J**, Usman A, Reid SA, King KF, Patterson AJ, Gillard JH and Graves MJ. "3D black blood T_2 mapping of the carotid artery wall with compressed sensing and data-driven parallel imaging". 22nd British Chapter of the ISMRM, Leeds, UK, 2016.
3. **Yuan J**, Usman A, Reid SA, King KF, Patterson AJ, Gillard JH and Graves MJ. "3D black blood imaging with compressed sensing of carotid artery: a reproducibility study". 22nd British Chapter of the ISMRM, Leeds, UK, 2016.
4. **Yuan J**, Makris G, Patterson AJ, Usman A, Das T, Priest AN, Teng Z, Hilborne S, Prudencio D, Gillard JH and Graves MJ. "High resolution simultaneous 4D CE-MRA and 3D DCE-MRI of carotid atherosclerotic plaques". 24th Postgraduate Symposium of the British Chapter of the ISMRM, London, 2016.
5. **Yuan J**, Usman A, Reid SA, King KF, Patterson AJ, Gillard JH and Graves MJ. "3D black blood T_2 mapping of the carotid artery wall with compressed sensing and data-driven parallel imaging". ISMRM 25th Annual meeting, Honolulu, HI, USA, 2017.
6. **Yuan J**, Usman A, Reid SA, King KF, Patterson AJ, Gillard JH and Graves MJ. "Three-dimensional black-blood multi-contrast protocol for carotid imaging using compressed sensing: a repeatability study". ISMRM 25th Annual meeting, Honolulu, HI, USA, 2017.
7. **Yuan J**, Patterson AJ, Ruetten PPR, Reid SA, Graves MJ and Gillard JH. "Comparison of black blood T_2 mapping sequences in carotid artery at 3T". ISMRM 25th Annual meeting, Honolulu, HI, USA, 2017.
8. **Yuan J**, Graves MJ, Patterson AJ, Priest AN, Ruetten PPR, Usman A and Gillard JH. "Optimization of 3D black-blood multi-echo T_2* weighted sequence in carotid artery". ISMRM 25th Annual meeting, Honolulu, HI, USA, 2017.

Secondary abstracts

9. **Yuan J**, Teng Z, Huang Y, Sutcliffe MPF and Gillard JH. "Atherosclerosis plaque mechanical modelling: Influence of material property and constitute law". 2nd UK Patient Specific Modelling Meeting, Edinburgh, 2014.
10. **Yuan J**, Teng Z, Huang Y, Sutcliffe MPF and Gillard JH. "Comparison of different strain energy functions in describing atherosclerotic plaque mechanical behaviors". 2nd UK Patient Specific Modelling Meeting, Edinburgh, 2014.

Abbreviations

2D	Two-dimensional
3D	Three-dimensional
ACS	Autocalibration signal
AIF	Artery input function
ARC	Autocalibrating reconstruction for Cartesian imaging
ASL	Arterial spin labelling
ASPIR	Adiabatic spectral inversion recovery
APS	Acquisitions-per-shot
bSSFP	Balanced steady-state free precession
CCA	Common carotid artery
CCC	Concordance correlation coefficient
CE	Contrast-enhanced
CEA	Carotid endarterectomy
CI	Confidence interval
CNR	Contrast-to-noise radio
CoV	Coefficient of variance
CPEO	Centric phase encoding order
CS	Compressed sensing
CTA	Computed tomographic angiography
DANTE	Delay alternating with nutation for tailored excitation
DCE	Dynamic contrast-enhanced
DDEO	Distance-determined encoding ordering
DICOM	Digital imaging and communications in medicine
DIR	Double inversion recovery
DISCO	Differential subsampling with Cartesian ordering
DTI	Direct thrombus imaging
DSA	Digital subtraction angiography
ECG	Electrocardiography
ECST	European carotid surgery trial
ESP	Echo spacing
ETL	Echo train length
FC	Fibrous cap
FLASH	Fast low-angle shot

FSE	Fast spin echo
FSPGR	Fast spoiled gradient echo
GRE	Gradient recalled echo
HR	Hazard ratios
ICA	Internal carotid artery
ICC	Interclass correlation coefficient
iMSDE	Improved motion sensitive driven equilibrium
IMT	Intimal-media thickness
IPH	Intraplaque haemorrhage
IQR	Interquartile range
KFRS	Kalman filtering registration and smoothing
LDL	Low-density lipoprotein
LRNC	Lipid-rich necrotic core
MCA	Middle cerebral artery
MESE	Multi-echo spin echo
MEFSE	Multi-echo fast-spin-echo
ME-FSPGR	Multi-echo fast spoiled gradient echo sequence
MIP	Maximum intensity projection
MRA	Magnetic resonance angiography
MRF	Magnetic resonance fingerprinting
MRI	Magnetic resonance imaging
MSDE	Motion sensitive driven equilibrium
MT	Magnetization transfer
NASCET	North American symptomatic carotid endarterectomy trial
NEX	Number of excitation
NMR	Nuclear magnetic resonance
PD	Proton density
PDw	Proton density weighted
PI	Parallel imaging
PK	Pharmacokinetics
QIR	Quadruple inversion recovery
QSM	Quantitative susceptibility mapping
RF	Radiofrequency
RFEO	Radial fan-beam encoding ordering
SAR	Specific absorption rate
SD	Standard deviation
SE	Spin echo

SMC	Smooth muscles cell
SNR	Signal-to-noise ratio
SPGR	Spoiled gradient recalled echo
SWI	Susceptibility weighted imaging
T_1w	T_1-weighted
T_2w	T_2-weighted
TE	Echo time
TI	Inversion time
TIA	Transient ischemic attack
TR	Repetition time
TRICKS	Time-resolved imaging of contrast kinetics
TOF	Time of flight
USPIO	Ultra-small superparamagnetic particles of iron oxide
VPS	Views per segment
VVI	Vasa vasorum imaging
XRA	X-ray contrast angiography

Contents

List of figures

List of Tables

Chapter 1 Stroke and carotid atherosclerotic disease

This thesis focuses on magnetic resonance imaging (MRI) as a non-invasive tool to quantify carotid atherosclerotic plaque properties in vivo. In this chapter, the importance of stroke and carotid atherosclerotic disease is described. The current limitations of carotid disease management and the use of MRI in assessing carotid plaque morphological features are reviewed. Part of this chapter has been published as a review paper in American Journal of Neuroradiology. 2017,38(4):664-671 [1].

1.1 Stroke and carotid atherosclerotic disease

Stroke is one of the leading causes of death and disability in the world, killing 4.4 million people each year and resulting in significant morbidity in 5,000 individuals per million in the population [2]. In the United Kingdom, stroke is the 3rd leading cause of death, accounting for 10% of all deaths, and also the most common cause of adult morbidity. Stroke related management costs the National Health Service (NHS) £9 billion a year (0.4% of the Gross Domestic Product, GDP) [3]. Although stroke is the commonest cause of mortality in China only 0.06% of the GDP (40 billion RMB annually) is spent on managing it [4].

Over 80% of the strokes are ischaemic. It is caused by the occlusion of blood vessels supplying oxygen and nutrients to the brain [5]. Rupture of atherosclerotic plaques located in the carotid arteries is a major cause of this kind of stroke, as shown in Figure 1.1.

Figure 1.1 Atherosclerotic plaque at carotid regions. Available online [6].

Carotid plaque rupture is found more frequently in symptomatic than asymptomatic patients (74% vs. 32%) [7]. However, the mechanism of plaque rupture remains poorly understood.

1.2 Pathology of atherosclerosis

Historical evidence of atherosclerosis includes the appearance of large calcified patches in the aortas of Egyptian mummies dating back ~3500 years [8]. The number of people who suffer from atherosclerotic disease continues to rise and parallels the spread of diet, lifestyle and other environmental risk factors associated with modernisation.

The pathogenesis of atherosclerosis includes initial stage disease which begins in childhood and adolescence with the appearance of fatty streaks [9]. These occur when the low-density lipoprotein (LDL) levels increase. The LDL complexes accumulate and enter the arterial intima. The fatty streaks are made up of smooth muscles cells (SMC), lipid-rich macrophages, foam cells, and the proteoglycan-collagenous matrix [10].

Early fibroatheroma occurs at the second stage of atherosclerosis [9]. At this point, the lesion accumulates numerous macrophage foam cells and activated inflammatory cells. The death of macrophages and smooth muscle cells stimulate further inflammatory processes. Large amounts of extracellular lipids forms into the lipid pool which contains cholesterol and cholesterol esters. The enlarging lipid-rich necrotic cores may ultimately occupy 30% - 50% of the artery wall volume [9]. Fibrous tissue forms a fibrous cap overlying the lipid pool to separate it from the lumen.

The fibrous cap is predisposed to macrophage and T-cell infiltration and becomes thin and weak. Atherosclerotic plaque with thin fibrous cap and large lipid pool is called vulnerable plaque and is prone to rupture without any warning.

More detailed biological and pathological processes during the disease initialisation, development, and plaque rupture are illustrated in Figure 1.2.

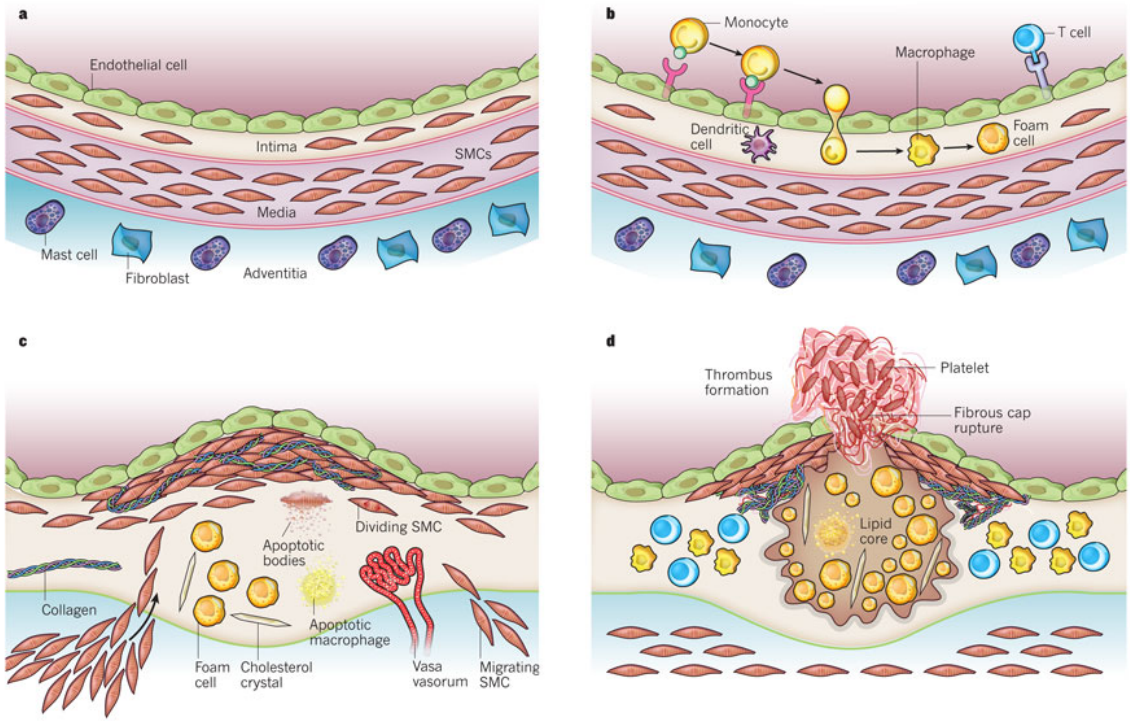

Figure 1.2 Formation, development, and rupture of atherosclerotic plaque. (a), the normal artery contains three layers, intima, media and adventitia; (b), adhesion of blood leukocytes to endothelial monolayer, maturation of monocytes into macrophages, and uptake of lipid, yielding foam cells; (c), migration of smooth muscle cells (SMCs) from the media to the intima during lesion progression. The apoptosis of macrophages and SMCs causes extracellular lipid to form the lipid and necrotic core. Vessel wall thickening causes hypoxia, resulting the formation of vasa vasorum in the plaque; (d), rupture of the fibrous cap causes thrombosis. With permission [11].

1.3 Current quantification of carotid disease and their limitation

Luminal stenosis, which is the current criterion for assessing the carotid disease severity, is important in clinical decision making. Patients with a high degree of stenosis (70 - 99% using North American Symptomatic Carotid Endarterectomy Trial (NASCET) measurement criteria) undergo a carotid endarterectomy (CEA) to remove the lesion [12].

The NASCET trial [13], studied 1212 patients from 50 centres across Canada and the United States who were randomised to either carotid endarterectomy (616 patients) or medical therapy (596 patients). This study found that CEA was efficient in reducing the stroke risk in patients only with severe narrowing (70 - 99%) [13]. However, the benefit of surgery was

reduced for moderate narrowing (50 - 69%). The patients with less than 50% stenosis did not benefit from CEA [14, 15] although strikingly 50% of strokes occur in patients with less than 50% stenosis using NASCET criteria.

The European Carotid Surgery Trial (ECST), showed that 44% of the 3018 patients with the symptomatic carotid disease had only < 30% stenosis using the ECST method [16]. The above stenosis measurement methods are illustrated in Figure 1.3. In the UK, the NASCET method is used as it is a more straightforward indicator of the stenosis, as the ICA is narrowed by the stenosis compared to the original diameter, while the ECST method has to estimate the full lumen diameter at the stenosis side.

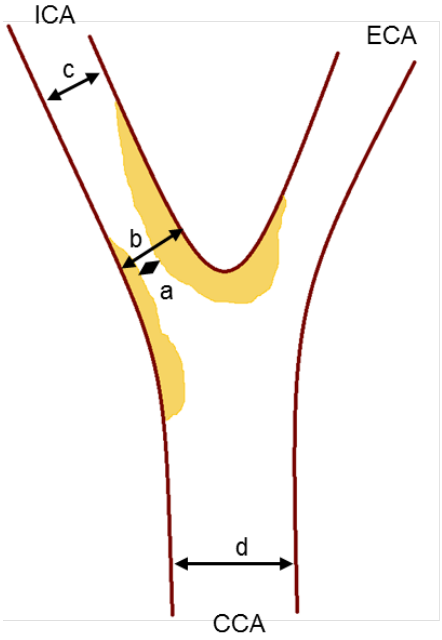

ECST stenosis: $\left(1-\frac{a}{b}\right)\times 100\%$

NASCET stenosis: $\left(1-\frac{a}{c}\right)\times 100\%$

Common carotid stenosis: $\left(1-\frac{a}{d}\right)\times 100\%$

ICA: internal carotid artery
ECA: external carotid artery
CCA: common carotid artery

Figure 1.3 Carotid lumen stenosis definitions in European Carotid Surgery Trial (ECST) [17], North American Symptomatic Carotid Endarterectomy Trial (NASCET) [13] and common carotid criteria [18].

Traditionally, X-ray angiography (XRA) was taken as the gold standard for carotid stenosis measurement. However, due to the invasive nature of XRA and the associated costs, duplex ultrasound is now the common technique for screening and measuring stenosis. As the flow velocity measured by duplex ultrasound reflects the degree of the stenosis, the Joint Working Group formed between the Vascular Society of Great Britain and Ireland, and the Society for Vascular Technology of Great Britain and Ireland recommended that the peak systolic velocity of < 125 cm/s for < 50% stenosis and 230 cm/s for ≥ 70% stenosis, with an

additional value of > 400 cm/s for ≥ 90% stenosis but less than near occlusion [19]. Figure 1.4 showed the relationship between peak systolic velocity with the angiographic diameter stenosis.

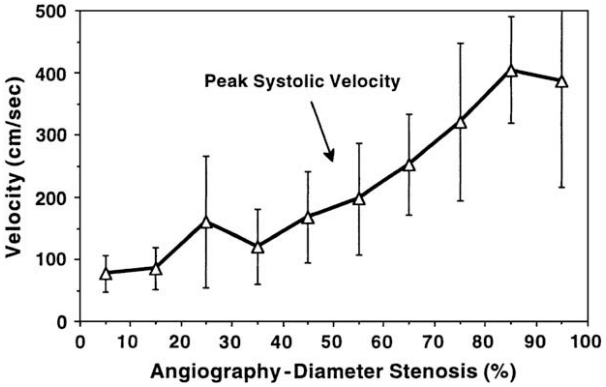

Figure 1.4 Relationship between duplex ultrasound peak systolic velocity vs. the stenosis by the NASCET criteria. With permission [19].

About 80% of plaque rupture occurs in patients with only moderate narrowing (< 69%) [20] Current luminal stenosis criteria cannot provide accurate assessment for this patient cohort. Therefore, additional biomarkers/analyses are needed.

In addition, conventional angiographic based techniques cannot capture lesions with outward remodelling, which might preserve lumen diameter (Figure 1.5) [21, 22].

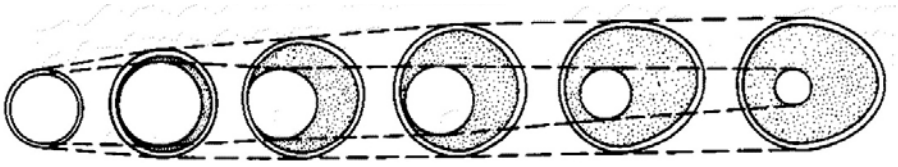

Figure 1.5 Early stages of lesion development involves lumen enlargement, which cannot be picked by the angiography. After a certain degree (around 40% of stenosis), the plaque development caused narrowing of the lumen. Reproduced with permission from [21], Copyright Massachusetts Medical Society.

1.4 Morphology of vulnerable plaque

1.4.1 Intraplaque components

Plaques with a large lipid pool (> 25% of plaque area) and thin fibrous cap (FC) (< 65 μm) [23] with a prominent macrophage infiltration are characterised as vulnerable plaques, as shown in Figure 1.6. Histological analysis of the CEA specimen suggests that plaque

morphology and compositional features may be different in symptomatic and asymptomatic patients. Plaque rupture was found more frequently in symptomatic patients than asymptomatic patients (74% vs. 32%) [7]; the necrotic core was twice as close to the lumen in symptomatic plaques as compared with asymptomatic plaques, the number of inflammation cell within the FC was three times higher [24] and the prevalence of intraplaque haemorrhage (IPH) is much wider [25].

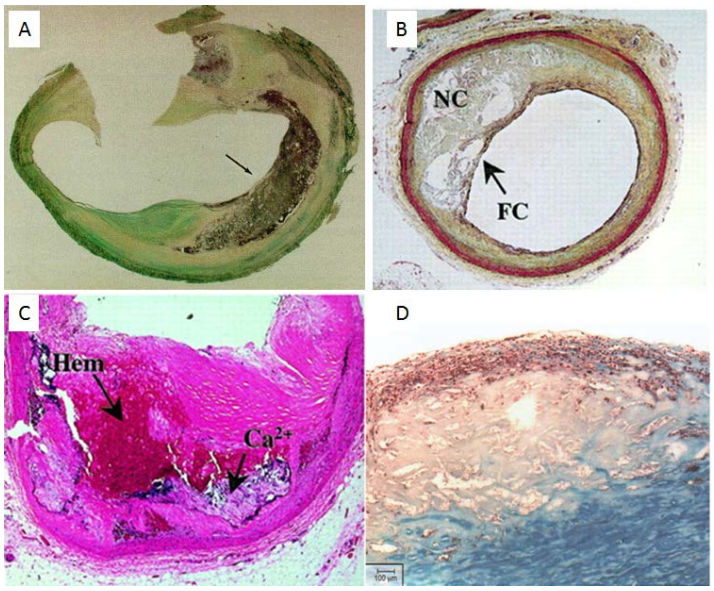

Figure 1.6 Histology of an atherosclerotic plaque. (A): A thin FC (arrow) and a ruptured FC at the top. With permission [7]; (B): Large necrotic core (NC) and overlying thin FC; (C): Plaque haemorrhage and calcification; and (D) Elastic Trichrome stained plaque showing FC with the abundant inflammatory macrophage cells appearing brown. With permission [26].

1.4.2 Plaque ulceration

Carotid plaque ulceration or surface irregularity is characterised as an indentation, fissure or erosion on the luminal surface of a plaque, exposing a portion of the inner plaque to direct contact with the circulating blood [27]. Various factors are involved in the pathogenesis of ulceration that includes the accumulation of inflammatory cells, proteolytic enzymes released by macrophages and local hemodynamic factors [28]. These factors weaken the fibrotic cap leading to plaque rupture and leaving behind the ulceration. These ulcerations act as a thromboembolic source allowing plaque components to be released into the blood. Ulcerated plaques are considered to be the main foci of cerebral microemboli [29].

Plaque ulceration is strongly correlated with ischemic stroke and coronary events with hazard ratios (HR) ranging from 1.2 to 7.7 [30-35], as summarised in Table 1.1. The hazard

ratio is comparable with other high-risk factors such as large lipid core (HR: 1.75) and intraplaque haemorrhage (IPH) (HR: 5.85) [36].

Studies	Study population	Cardiovascular events	Hazard Ratios (95% CI)	P value
Eliasziw et al, 1994 [30]	659	Ipsilateral stroke at 24 months	1.24 (0.61-2.52) – 3.43 (1.49-7.88)	-
Handa et al, 1995 [31]	214	Stroke events in average duration of 16 months	7.68 (2.15-27.40)	0.002
Rothwell et al, 2000 [32]	3007	Strokes occurring >2 years	2.75 (1.30-5.80)	0.01
Rothwell et al, 2000 [32]	3007	Ipsilateral ischemic stroke	1.80 (1.14-2.83)	0.01
Rothwell et al, 2000 [33]	3007	Previous myocardial infarction	1.82 (1.23-2.64)	<0.001
Rothwell et al, 2000 [33]	3007	Non-stroke vascular death	1.67 (1.15-2.44)	0.007
Rothwell et al, 2005 [34]	1130	5-year risk of ipsilateral ischemic stroke	2.03 (1.31-3.14)	0.002
Prabhakaran et al, 2006 [35]	1939	Ischemic strokes during a mean follow-up of 6.2 years	3.1(1.1-8.5)	-

Table 1.1 Summary of hazard ratios of carotid ulceration for future events risk in the published literature. With permission [1].

1.5 Multi-contrast MRI of carotid plaque

In 1998, Yuan et al. first demonstrated that MRI is highly accurate for carotid artery wall measurement in vivo compared to histology [37]. Since then, numerous studies have been undertaken to study carotid plaque components and quantify the size and area accordingly. The results demonstrated that MRI is capable of identifying the components, including calcium, lipid, IPH and FC with moderate to good accuracy [38]. An example of multi-contrast MRI is shown in Figure 1.7.

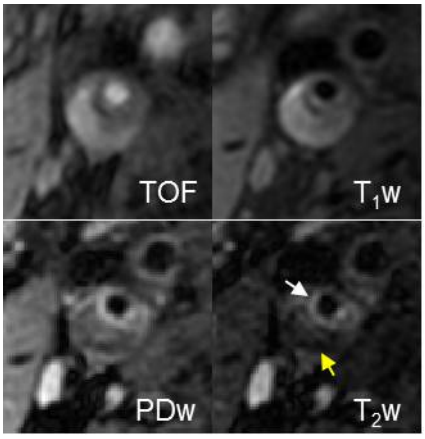

Figure 1.7 Multi-contrast MRI of carotid plaque with thin fibrous cap and large lipid core. The fibrous cap (white arrow) shows hyperintense signal on the T_2w image. The lipid core (yellow arrow) shows hypointense in the T_2w image. The images are acquired by the author.

Table 1.2 summarises the signal intensity of various plaque components on MR images with different weightings. It should be noticed that haemorrhage is classified into 3 categories according to its age: fresh haemorrhage (< 1 week) encompasses early clotting mechanisms, macrophages and inflammatory cell infiltration; recent haemorrhage (1 - 6 weeks) includes the combination of haemorrhagic debris, intact and degenerating red blood cells; old haemorrhage (> 6 weeks) in the plaque has mixed components in a heterogeneous substrate [39]. However, due to the long scanning time and expensive cost, currently MRI is not used clinically to evaluate the carotid disease.

	TOF	**T_1W**	**PDW**	**T_2W**
	0	0/+	0/+	-/0
IPH (fresh) [39]	+	+	-/0	-/0
IPH (recent) [39]	+	+	+	+
IPH (old) [39]	-	-	-	-
Dense (fibrous) tissue [40]	-/0	0	-/0	+
Loose matrix	0	-/0	+	+
Calcification [40]	-	-	-	-

Table 1.2 Tissue classification criteria using MRI. All signal intensities are relative to the adjacent sternocleidomastoid muscle. +: hyper-intense; 0: iso-intense; -: hypo-intense.

1.6 Imaging of carotid plaque and plaque ulceration

1.6.1 X-ray contrast angiography (XRA)

XRA has been widely used in large, randomised clinical trials in early years [13, 17]. Luminal stenosis measured from the projection of XRA was often used for carotid diseases management. XRA was a gold standard for observing carotid ulceration. Studies comparing angiographic surface morphology with detailed histology have concluded that ulceration detected by XRA was associated with plaque rupture, IPH and overall plaque instability [41]. An example of a carotid DSA demonstrating an ulcerated plaque is shown in Figure 1.8.

Figure 1.8 DSA image of two large ulcerations (arrows) of a right internal carotid artery. The figure is adapted with permission [1].

However, due to the subtraction procedure, observing intraplaque component using DSA is difficult. In addition, the use of XRA in the carotid imaging has several limitations. First, it is a high-cost procedure, time-consuming and requires adequate bed rest after the investigation. Second, the invasive nature of this procedure increases the risk of creating emboli resulting in subsequent cerebrovascular events [15, 42, 43]. Third, XRA is not safe in patients with coagulopathies and bleeding disorders. Fourth, for detecting the ulceration, the accuracy of XRA also depends on the degree of stenosis [44]. The rate of false positives and false negatives of DSA were high in identifying ulcerations [45]. One reason for this is that the XRA generally only uses a limited number of projections. This issue results in failures to detect ulceration [45, 46] and a tendency to underestimates stenosis [47].

Based on the above mentioned reasons there has been a trend to replace XRA with various cost effective, safer and less time-consuming carotid imaging modalities which are discussed below.

1.6.2 Ultrasound

Ultrasound was introduced as the first platform to visualise the in vivo human vessel and atherosclerosis [48]. The biggest advantage of ultrasound is the low cost. Carotid ultrasound helps to classify the plaque texture either as homogeneous (uniform consistency) or heterogeneous (non-uniform consistency) [49], determines the plaque location, count the plaque number, measure the intima-media thickness (IMT) and can also observe the plaque surface morphology [50]. The plaque type can be determined by using the ultrasound images. For instance, a soft plaque contains large lipid core appears echolucent in the image, while a plaque with lots of fibrous tissue and calcification appears as echogenic. An example of different types of carotid plaques in ultrasound images is shown in Figure 1.9.

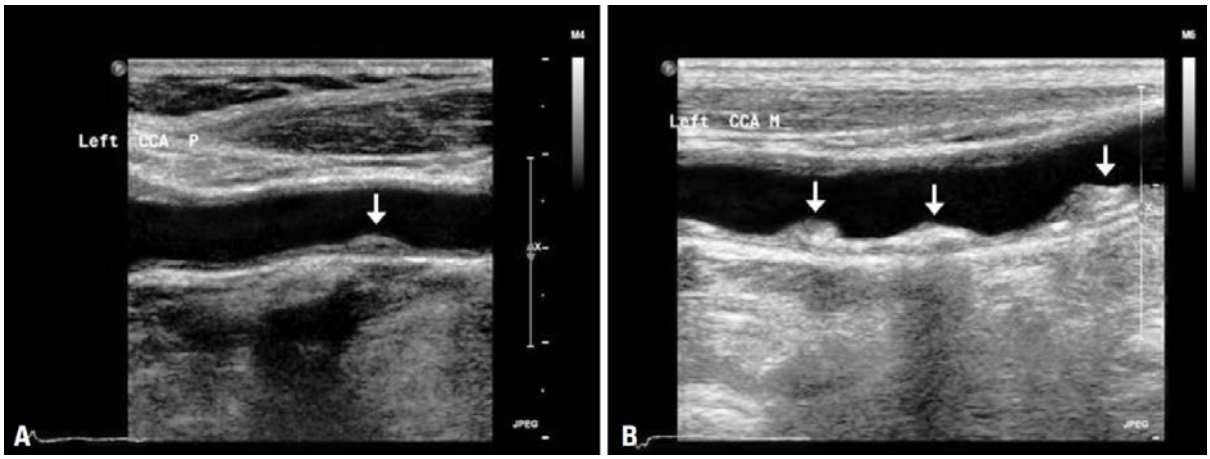

Figure 1.9 (A) A single low-risk plaque in shown. The plaque causes moderate stenosis and has a smooth homogenous surface. (B) Multiple complex high-risk plaques are shown. The plaques have focal calcification and irregular surface, and cause a higher degree of stenosis. With permission [50].

In ultrasound images, the plaque surface can be defined as smooth and regular, mildly irregular, or ulcerated; based on the plaque contour [51]. The application of colour-flow Doppler-assisted duplex imaging, which combines the B-mode and blood flow velocity information [52], can measure the flow dynamics in the carotid lumen, which is a useful tool for determining the stenosis and carotid ulceration. An example of ulceration in Doppler ultrasound is shown in Figure 1.10. However, it is still difficult to detect plaque ulceration using ultrasound due to various limitations. Firstly, the overall accuracy of using ultrasound against gold standard techniques (DSA) is not high (sensitivity and specificity range from 39 - 89% and 72% - 87%, respectively) [53-57]. Several studies have noted that its accuracy decreases with increasing degree of stenosis [56, 58], and has even failed to detect ulceration in high-grade stenosis [55]. Secondly, the intra-reader reproducibility of both B-mode and Doppler ultrasound is low (K ranges from 0.11 to 0.89 [56, 59-61]), which is not

sufficient for reliable diagnosis. These limitations are mostly due to the native imaging principle. Two-dimensional (2D) ultrasound can only obtain a 2D cut plane of the carotid area, this could introduce error when the ultrasound probe is not parallel to the vessel axis or the orientation of the ulceration [62]. Also, the presence of calcification reflects the acoustic wave which can obscure ulceration [62]. The recent development of 3D ultrasound, either using dedicated 3D probes or combining 2D probe and positioning sensors [61, 63], showed improved image quality, and could be more suitable for plaque morphology, echomorphology, stenosis and volume measurement and analysis [64, 65].

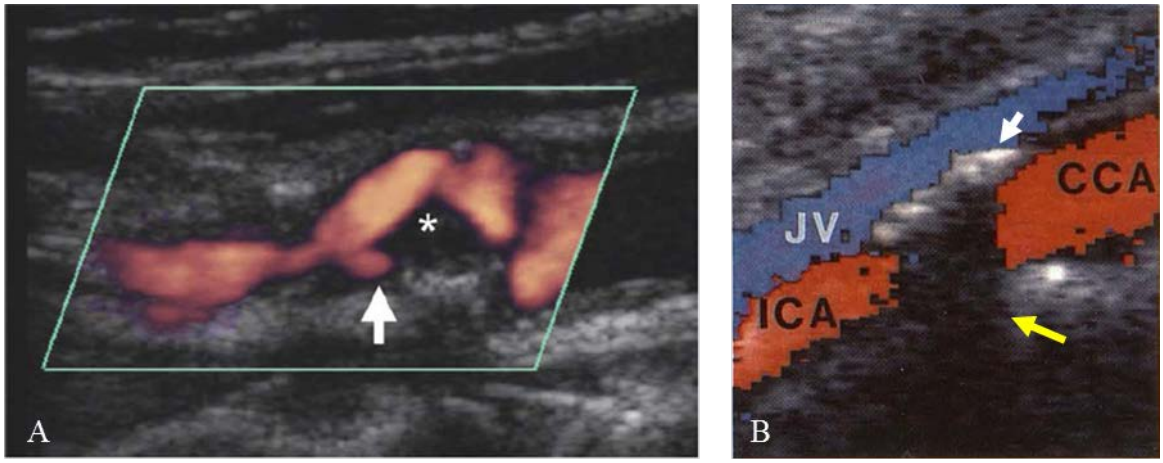

Figure 1.10 (A) Doppler ultrasound shows an internal carotid artery plaque ulceration (white arrow). The figure is adapted with permission [1]. (B) the calcification in the anterior vessel wall (white arrow) shadows the colour Doppler signal and opposite wall structures (yellow arrow). The figure is adapted with permission [1].

1.6.3 Computed Tomography Angiography (CTA)

CTA has been used widely for the head and neck imaging due to the fast acquisition with high resolution. Studies have shown that CTA can be used for characterization of plaque composition [66, 67], especially the calcification. Also, CTA would be suitable for detecting carotid ulceration. CTA showed high sensitivity (94%) and specificity (99%) in detecting ulceration, when comparing to the surgical observation [68]. However, as CTA is very sensitive for the carotid calcification, it might fail in detecting ulceration in heavily calcified plaques [69].

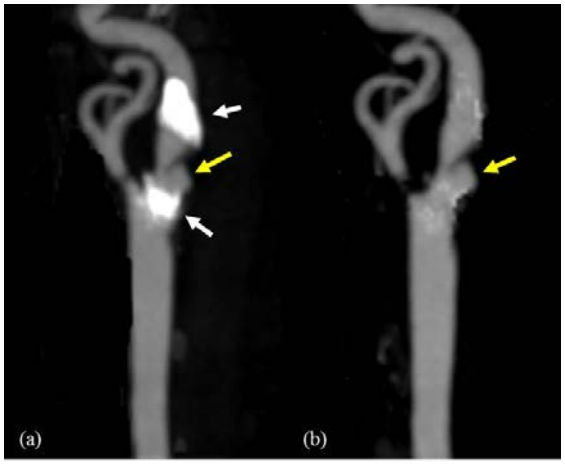

Figure 1.11 (a) An ulceration (yellow arrow) in a heavily calcified (white arrow) plaque. (b) the ulcer is clearer with calcification removed by dual energy CTA. (The images are processed by the author). With permission [1].

The recent development of dual-source CT, which uses two X-ray energies simultaneously to separate high density calcification and the contrast-enhanced lumen, has shown advantages for evaluating the densely calcified carotid stenosis and could be more accurate in evaluating plaque components [70, 71]. Figure 1.11 shows that the morphology of ulcerations cannot be visualised clearly by conventional CTA due to calcification, while dual-source CTA software could remove the calcification from the image, making the ulcer clearer.

Like XRA, a drawback of CTA is the use of ionising radiation. In imaging the neck vessels, the radiation dose of CTA is equivalent to or higher compared with DSA [72, 73]. Also, the use of contrast agents is not suitable for patients with significant renal disease [74].

1.6.4 MRI for ulceration imaging

Non-contrast enhanced Magnetic Resonance Angiography (MRA)

The most common method for MRA is time-of-flight (TOF) which relies on the high MRI signal from the moving blood, within the vessel lumen to create vascular contrast [75]. Both 2D, i.e. multi-slice [76] and 3D, i.e. volumetric TOF [75, 77] have been used for carotid artery imaging. One of the biggest advantages of MRA over DSA and US is that the images can be reformatted into any orientation after the acquisition.

However, one of the well-known limitations of TOF-MRA is that signal saturation and dephasing of the signal could lead to a signal loss from focal areas of complex flow [78]. The stenosis measurement accuracy of TOF is dependent on the wash-in efficiency of

unsaturated spins within the imaging slice/slab. For large ulcerations, the hemodynamic patterns of blood flow are complicated [79]. Ulceration detection could therefore be limited if the saturated spins do not get replaced by fresh unsaturated blood flow. Also, the orientation of the imaging slice/slab is important. TOF techniques are limited to the flow orthogonal or a certain angle to the imaging slices/slabs. The signal from flowing blood parallel to the imaging slices/slabs can become saturated [77]. In addition, the ulceration orientation, location, and shape could also influence the accuracy of measurements using TOF-MRA [79]. In recent years, other non-contrast enhanced MRA techniques have emerged claiming to overcome some of the limitations of TOF-MRA, including arterial spin labeling (ASL) [80, 81], inversion-recovery based methods [82], the quiescent interval low-angle shot (QLASH) method [83] and blood suppression based methods [84]. In particular, a hybrid of pseudo-continuous and pulsed ASL (hASL) with fast low-angle shot (FLASH) readout has shown comparable results in detecting carotid luminal irregularity with CE-MRA, which overcomes the limitation of TOF-MRA [81]. Since these methods have only recently been developed, more studies are necessary to validate their accuracy in detecting plaque ulceration.

Contrast-Enhanced MRA (CE-MRA)

CE-MRA is an MR imaging technique for vascular imaging that exploits the use of an intravenously administered paramagnetic contrast agent (i.e. a chelate of gadolinium) to shorten the T_1 relaxation time of the blood providing excellent contrast with the background tissues. Since the images are no longer dependent on the inflow of the blood, CE-MRA produces high-quality images in a short time frame and may reduce some of the drawbacks associated with TOF-MRA. In one study the prevalence of plaque ulceration was 86% in a symptomatic patient cohort compared to 36% in an asymptomatic patient group; indicating that CE-MRA could be used for detecting ulceration [85]. CE-MRA has also been shown to detect more ulcers than TOF-MRA [79]. Figure 1.12(a, b) shows an internal carotid artery with several ulcerations demonstrated by CE-MRA, however all were missed by TOF-MRA. In addition, CE-MRA has the advantage of visualising ulceration in calcified plaques which is one of the limitations of standard CTA (Figure 1.12c).

Although CE-MRA shows a high level of accuracy in detecting plaque ulceration, it is still a relatively expensive examination. MRI is not suitable for patients with contraindications such as implanted devices. Lastly, the contrast agents should not be used in patients with renal impairment, which may limit its wider application.

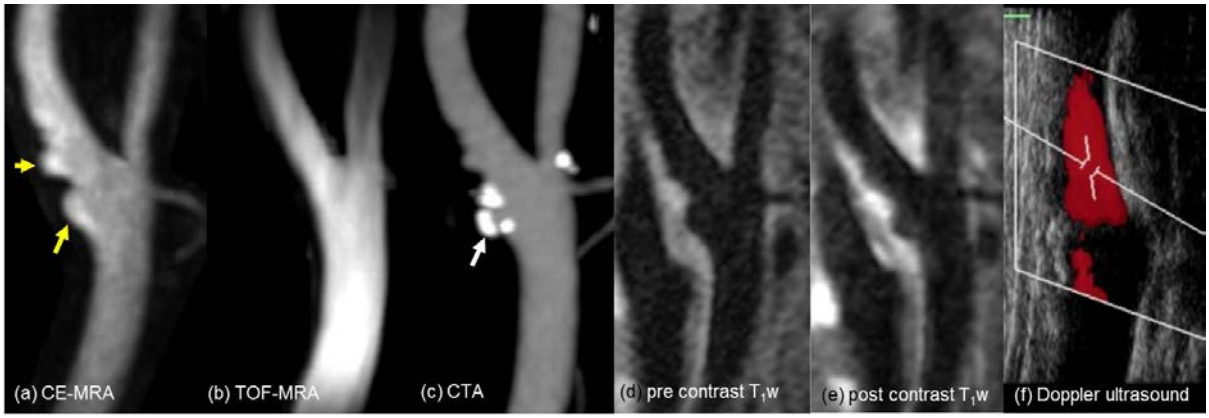

Figure 1.12 High-resolution MRI, CTA and ultrasound of the left carotid artery of a 77-year old man. Ulcerations (yellow arrow) are shown clearly on CE-MRA (a), pre- and post-contrast black blood T_1w (d, e) images, however missed on TOF-MRA (b). The calcification on CTA (c, white arrow) brings difficulty when observing ulceration. The Doppler ultrasound (f) shows no ulceration in the internal carotid artery. (The MR images are acquired by the author. The CT and ultrasound images are processed by the author.) With permission [1]

Blood suppressed MR Morphological imaging

High-resolution standard MR sequences are widely used for carotid morphological imaging, however the signal from flowing blood in the lumen makes it difficult to identify the vessel wall. Blood suppression is usually achieved through a signal preparation scheme applied prior to the imaging sequence. The most commonly used schemes including double or quadruple inversion recovery (DIR or QIR) [86, 87], motion sensitive driven equilibrium (MSDE) [88], and delay alternating with nutation for tailored excitation (DANTE) [89]. These blood suppressed techniques will be introduced in detail in the subsequent chapter. Multi-contrast cross-sectional MRI with blood could also be used for ulceration detection [90, 91]. Figure 1.12(d,e) shows an example of carotid ulceration in DANTE prepared pre- and post-contrast T_1w images.

In summary, this chapter introduces the formation, progression of carotid atherosclerosis plaque, current limitation of the management and the use of MRI in assessing plaque vulnerabilities. One of the high-risk features, carotid ulceration, can be detected by multiple imaging modalities. CE-MRA may be the best method due to high accuracy. But further work is warranted to study the effectiveness of non-contrast enhanced MRA in looking at the ulceration.

Chapter 2 Principles of Magnetic Resonance Imaging

This chapter describes the basic magnetic resonance imaging (MRI) principles and some of the advanced techniques used in this thesis, including the pulse sequences, image contrast mechanisms and blood suppression techniques.

2.1 Nuclear magnetic resonance

The phenomenon of nuclear magnetic resonance (NMR) was first demonstrated by Felix Bloch in 1946 at Stanford University [92] and Edward Purcell at the Massachusetts Institute of Technology [93]. They shared the Nobel Prize in Physics in 1952 for their discoveries.

Spin

The atomic nuclei are characterised by an intrinsic angular momentum spin. The nuclei with an even number of protons and even number of neutrons have a zero-angular momentum. Nuclei with odd numbers of nucleons have a non-zero angular momentum and their magnitude $|J|$ and projection in the z-direction J_z are given by:

$$|J| = \hbar[I(I+1)]^{1/2}, J_z = \hbar m_I \tag{2.1}$$

where $\hbar$ is the Plank's constant divided by 2π, I is the nuclear spin quantum number (0, 1/2, 1, …) and m_I is the magnetic quantum number (-*I*, -*I*+1, …, 0, …, *I*-1, *I*). For the hydrogen nucleus, *I* = 1/2 so that m_I can either be -1/2 or +1/2. As a result, there are only two possible orientations for *J*, in which the spins align with the +z (spin-up state) or –z (spin-down state) direction. Since the nucleus is electrically charged, the rotating spin generates an electric current flow around the rotation axis. This results in a magnetic field, which is associated with magnetic dipole moment μ:

$$\mu = \gamma J \tag{2.2}$$

where γ is the gyromagnetic ratio. For ^1H nucleus, $\gamma/2\pi$ = 42.57 MHz/T. The gyromagnetic ratio for other nuclei are shown in Table 2.1.

In the presence of a static magnetic field (*B*), the energy difference between the two states of protons is:

$$\Delta\epsilon = \Delta\mu B = \gamma\hbar\Delta m_I B = \gamma\hbar\left[\frac{1}{2} - \left(-\frac{1}{2}\right)\right] B = \gamma\hbar B \tag{2.3}$$

Given De Broglie's equation:

$$\Delta \mathrm{E} = \hbar\omega \tag{2.4}$$

where ω is the Larmor frequency. Then

$$\omega = \frac{\Delta\epsilon}{\hbar} = \gamma B \tag{2.5}$$

The ω describes the angular frequency that the magnetic dipoles processes in the presence of a magnetic field (*B*).

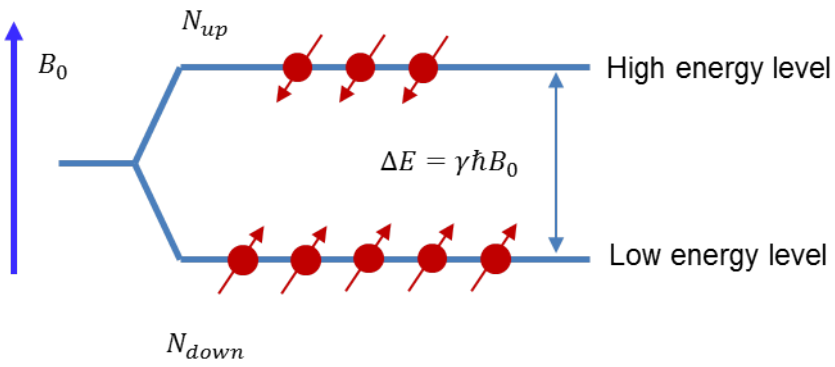

Figure 2.1 Boltzmann distribution of the protons at the present of magnetic field B_0. There are more spins at the low energy level (N_{down}) than the high energy level (N_{up}).

The spins split into two energy states according to the Boltzmann distribution at the temperature T (Figure 2.1):

$$\frac{N_{up}}{N_{down}} = exp(\Delta\epsilon/\kappa_B T) \tag{2.6}$$

where N_{up} and N_{down} are the number of the spins at the spin up and spin down state. κ_B is the Boltzmann constant and *T* is the absolute temperature. As the energy difference is very small between the two states, the low energy state is only slightly more populated than the high energy state (about 10 up spins more per million).

Nucleus	^{1}H	^{13}C	^{14}N	^{19}F	^{13}Na	^{31}P
Gyromagnetic Ratio, $\boldsymbol{\gamma}$ (MHz/T)	42.58	10.66	3.02	40.27	11.3	17.19

Table 2.1 Gyromagnetic ratio of different nuclei.

2.2 Magnetic Resonance Imaging

In 1973, Paul Lauterbur [94] applied NMR to imaging by using a linear magnetic field gradient to provide spatial localisation of the NMR signal. Peter Mansfield introduced the concept of slice-selection which can be used for 2D excitation [95] and Edelstein with colleagues proposed the standard method of 2D image encoding [96].

Paul Lauterbur and Peter Mansfield shared the 2003 Noble prize in Physiology or Medicine "for their discoveries concerning magnetic resonance imaging".

2.2.1 MR system

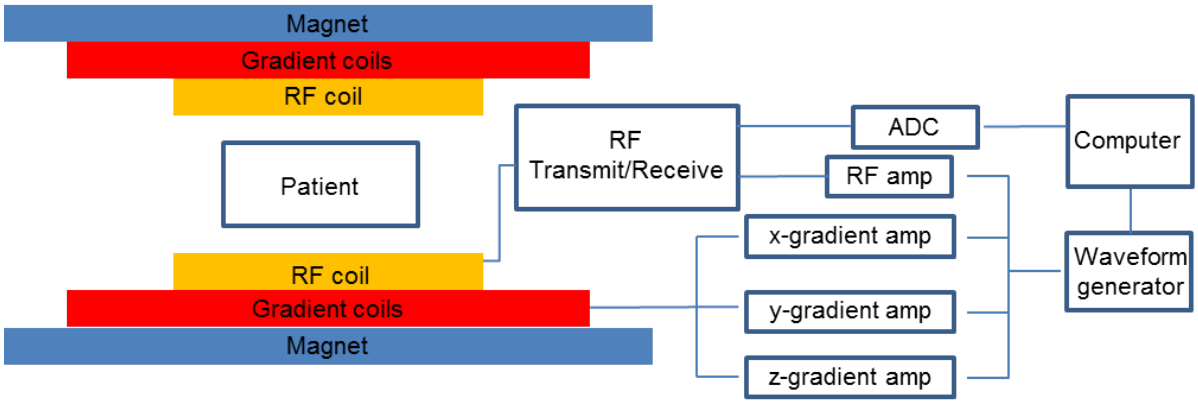

Figure 2.2 MRI system overview. ADC: Analog-to-Digital Converter.

There are three main components in an MRI system, comprising a magnet to create a strong static field (B_0), gradient coils to generate the linear magnetic field gradients, and a radiofrequency (RF) system to transmit energy to the object and then detect the MRI signal from the object.

Magnet

A strong static magnetic field is required to cause the Zeeman splitting in the protons, as shown in Equation 2.6. A permanent magnet is often used for low field system such as 0.35 T MRI. Nowadays, most clinical system uses superconducting coils to generate high magnetic fields such as 1.5 T or 3 T. The superconducting coils are immersed in liquid helium at a temperature of 4 K (-269 ℃). At such low temperature, the resistance of the coils drops to zero that allows strong current to go through without generating any heating. The strong current inside the coils generates a stable magnetic field through the scanner bore where the patient lies. To achieve perfect homogeneity of the magnetic field, ferromagnetic blocks are used as passive shimming and currents are generated in the coils to generate active shimming.

Gradients

Three orthogonal gradient coil pairs are placed inside the magnetic bore; they are used to generate orthogonal gradients which can be used for signal localisation. If the current goes through the gradient coil, the coil generates a linearly varying magnetic gradient along a certain direction. For the X and Y direction, a Golay configuration is used to generate the transverse magnetisation. For the Z direction, a Maxwell pair can be used. The three axes gradient coil setup is shown in Figure 2.3.

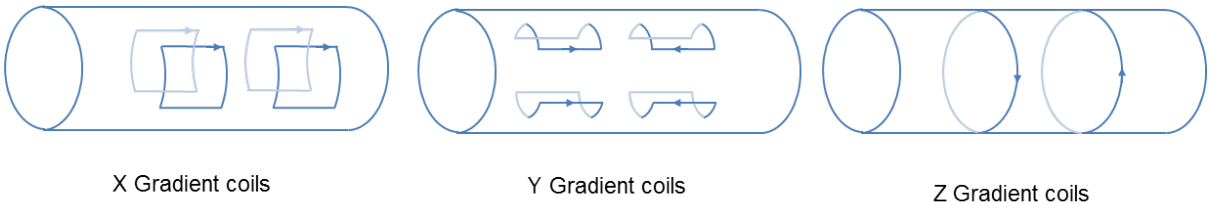

Figure 2.3 Gradient coils are used to generate location variation gradient in three axes.

Radiofrequency (RF) system

RF coils generate the RF which transmits into the imaging subject and excite the spins from the low energy state to the high energy state. Usually a large volume coil, referred to as the body coil, is used to provide a uniform RF magnetic field across a large field of view. After the transmitting RF is turned off, the spins at high energy level release the extra energy and return back to low energy level, and the system returns back to the equilibrium state. This process forms the MR signal, with includes the spatial information (described below), which is received by the RF coils to generate an image. The surface coils can be designed to receive RF signal according to the imaging region, such as a head coil, carotid coil, breast coil and knee coil et al. The surface coil has high sensitivity over a specific target region. The RF field that is transmitted is referred to as the B_1^+ field, and the RF field that is received is referred to as the B_1^- field.

2.2.1 Spin relaxation

MR signals are formed after the RF transmitting pulse, when the spins precess in the transverse plane. Early NMR studies showed that two different relaxation times can describe the spin relaxation phenomenon. The first is called the longitudinal or spin-lattice relaxation which describes the relaxation or recovery of the longitudinal magnetisation along M_z. This mechanism describes the process of spins releasing their energy to the surrounding environment and returning to the equilibrium state. This is phenomenologically described as a first order recovery, i.e., an exponential recovery. The T_1 is the time constant for this

recovery, is used to describe the recovery of the longitudinal magnetisation from zero to (1-1/e) of the equilibrium state. The second mechanism is called spin-spin relaxation, which describes the dephasing of the spins inside the object. Individual spins are influenced by the local fields caused by the surrounding spins. The interaction between the spins causes the overall spin dephasing, with no energy changes in this process. The rate that describes the overall dephasing is called T_2 relaxation, or spin-spin relaxation. It describes the overall spin phase decays from 1 to 1/e. In reality, the spins in the imaging subject also experience local field inhomogeneity, caused by local tissue environment, which may accelerate the spin-spin relaxation. The rate of the dephasing caused by the spin-spin and local field inhomogeneity is called T_2* relaxation. The relationship between T_2 and T_2* relaxation is:

$$\frac{1}{T_2^*} = \frac{1}{T_2} + \gamma \Delta B \tag{2.7}$$

where the $\gamma \Delta B$ describes the local field inhomogeneity. The T_1, T_2 and T_2* relaxation curves are shown in Figure 2.4.

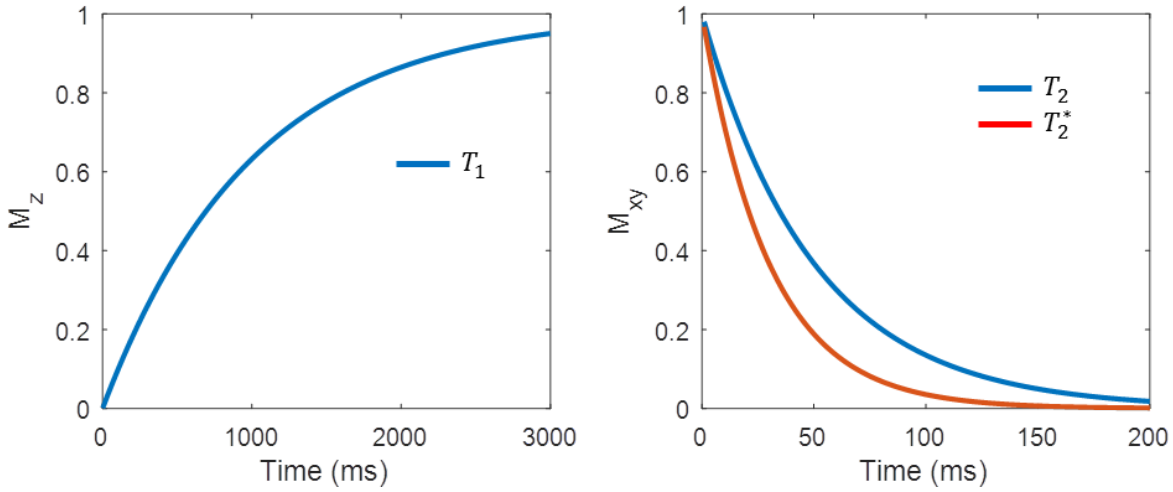

Figure 2.4 Longitudinal and transverse magnetization of simulated relaxations with T_1 = 1000, T_2 = 50 and T_2* = 30 ms.

Bloch equations

The phenomenon of the magnetisation relaxation can be described using Bloch equations [92]. The Bloch equations come from the motion of the magnetisation:

$$\frac{\mathrm{d}M_x(t)}{\mathrm{dt}} = \gamma\left(M_y B_z - M_z B_y\right) - \frac{M_x}{T_2}$$

$$\frac{\mathrm{d}M_y(t)}{\mathrm{dt}} = \gamma\left(M_z B_x - M_x B_z\right) - \frac{M_y}{T_2} \tag{2.8}$$

$$\frac{\mathrm{d}M_z(t)}{\mathrm{dt}} = \gamma\left(M_x B_y - M_y B_x\right) - \frac{M_z - M_0}{T_1}$$

where $M_{x,y,z}$ is the magnetisation along X, Y and Z axis, and B_x and B_y are the B_1 field in the X and Y direction. $B_x = B_1 \cos(\omega t)$ and $B_y = B_1 \sin(\omega t)$.

When the transmitting RF is turned off, the transmitting field B_1 is zero, then the Bloch equation becomes

$$\frac{\mathrm{d}M_x(t)}{\mathrm{dt}} = \omega_0 M_y - \frac{M_x}{T_2}$$

$$\frac{\mathrm{d}M_y(t)}{\mathrm{dt}} = \omega_0 M_x - \frac{M_y}{T_2} \tag{2.9}$$

$$\frac{\mathrm{d}M_z(t)}{\mathrm{dt}} = -\frac{M_z - M_0}{T_1}$$

Using a 90° excitation pulse as an example, immediately after the transmitting RF, the initial magnetisation are $M_{x,y} = M_0$ and $M_z = 0$. Therefore, the Bloch equation becomes:

$$M_x(t) = M_0 cos(\omega t) exp(-t/T_2)$$

$$M_y(t) = M_0 sin(\omega t) exp(-t/T_2) \tag{2.10}$$

$$M_z(t) = M_0\left(1 - exp(-1/T_1)\right)$$

This shows that the X and Y component is processing at the Larmor frequency. The T_2 relaxation time describes the rate of dephasing. The longitudinal magnetisation recoveries at the rate of T_1.

2.2.2 Slice selection

For a given 2D slice selective magnetic gradient (G_z, parallel to B_0), the precession frequency of the spins at location z can be described as

$$\omega_z = \gamma(B_0 + zG_z) \tag{2.11}$$

When both the slice selective gradient and RF pulse are applied simultaneously, the RF pulse will only excite the protons with the same precession frequency, as shown in Figure 2.5. By changing the centre frequency of the RF, the scanner can select different slices accordingly.

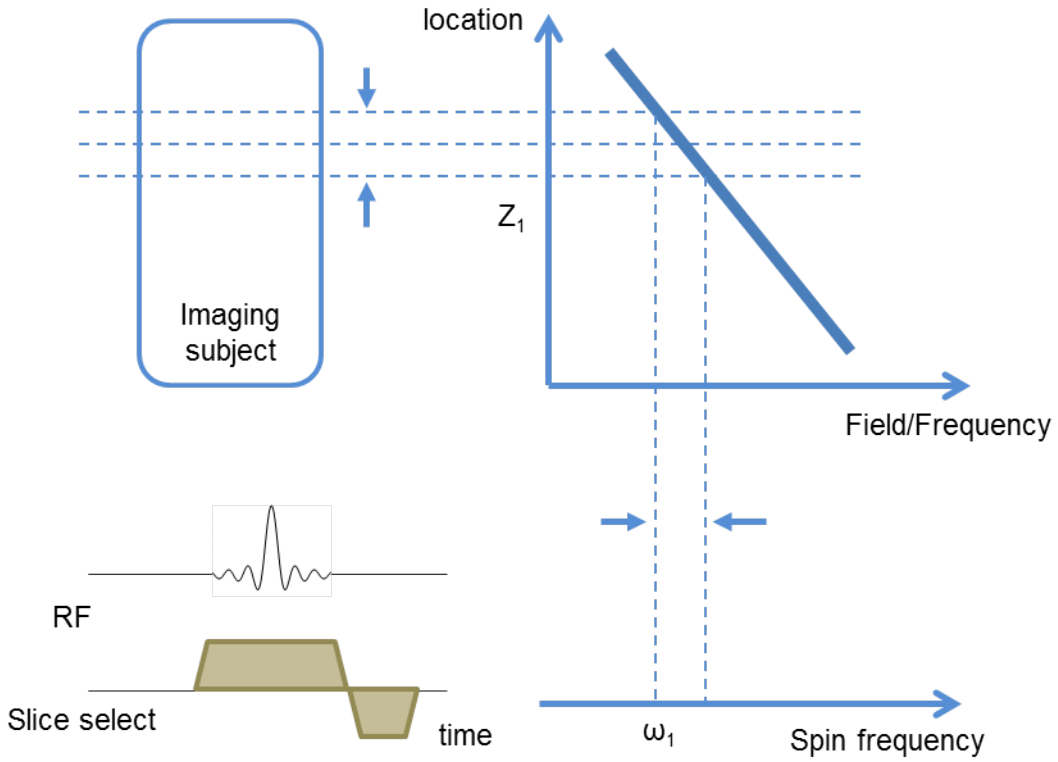

Figure 2.5 Diagram of the slice-selective pulse. A linear gradient is applied together with a sinc type RF pulse. Due to the linear gradient, only a slice of the imaging subject possesses the same frequency with the RF pulse. So only a certain slice can be selected in the slice-selective module.

2.2.3 Phase encoding

After the slice selection, the spins within the selected slice plane are then encoded through phase and frequency encoding. Initially, the spins in the plane process with the same Larmor frequency and spin phase. During the phase encoding, a gradient G_{PE} is applied along phase encoding direction, e.g., Y axis. With this gradient, the spin frequencies change slightly from the Larmor frequency, according to Equation 2.11. After a short period of time, the G_{PE} is switched off. The spins return back to the same frequency again, while different phase is accumulated according to their position along the Y axis. Therefore, the spin phase contains the information about the spin location in the Y direction.

2.2.4 Frequency encoding

After the phase encoding, during the readout, a frequency encoding gradient G_{FE} is applied along X direction. The spins at different location process at a different frequency. Therefore the acquired signal contains a range of frequencies. After the data acquisition, an inversion Fourier transform is performed and the signal with different frequency can be separated. An example of frequency encoding and inversion Fourier transform is shown in Figure 2.6.

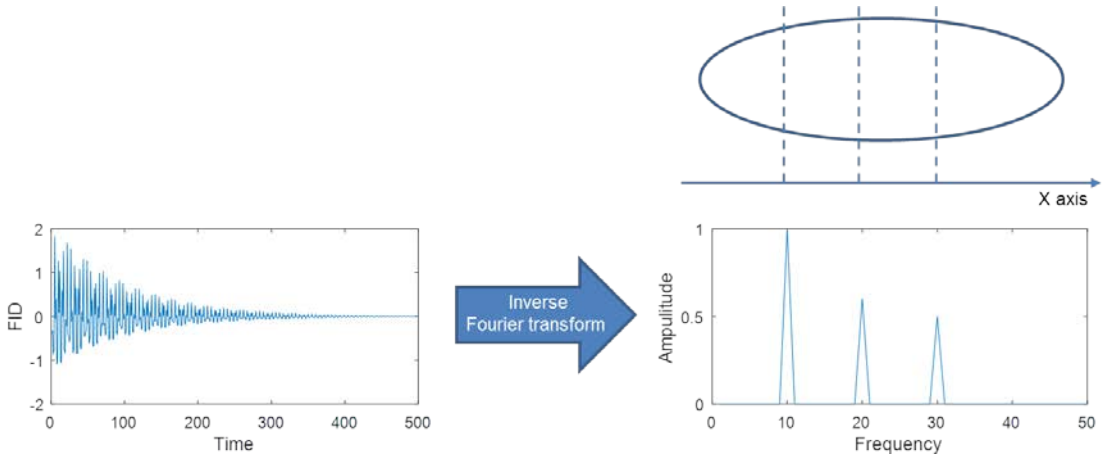

Figure 2.6 An example showing the frequency encoding. The frequency encoding gradient G_{FE} is applied along the X direction during the readout. The acquired signal consists a range of frequencies. The inverse Fourier transform could separate different signal according to the frequency.

2.2.5 *k*-space formation

The MRI image in the frequency domain is called *k*-space, which represents the spatial frequencies in the MR image. The *k*-space is the Fourier transform of the MR image. Each *k*-space point contains the spatial frequency of and phase information about every pixel in the image.

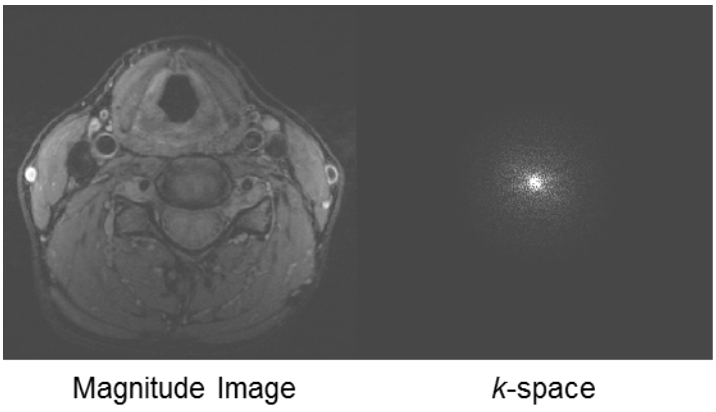

Figure 2.7. Magnitude image of a healthy volunteer and its corresponding *k*-space.

The phase encoding gradient is applied in a cycle, with each time changing the gradient amplitude, together with a frequency encoding step. Each step acquires a line of *k*-space (k_y). The element signal at the position **r**(x,y) can be described as:

$$M(x,y,t) = \rho(x,y)e^{i\omega t} \tag{2.12}$$

The magnitude M_0 depends on the spatial position in the subject with different proton density $\rho(x)$. If the phase and frequency encoding gradients are applied within the imaging plane, an additional phase term is added that depends on the time and location

$$M(x,t) = \rho(x)e^{i(\omega t+\varphi(x,y,t))} = \rho(x)e^{i\omega t}e^{i[\varphi(x,y,t)]} \tag{2.13}$$

The phase φ is from the time course of the phase and frequency encoding gradient

$$\varphi(x,y,t) = \int_0^t \Delta\omega(x,y,\tau)d\tau = \int_0^t \gamma\Delta B(x,y,\tau)d\tau = \int_0^t \gamma(G_{FE}(\tau)x + G_{PE}(\tau)y)d\tau = \gamma\int_0^t G_{FE}(t)d\tau\, x + \gamma\int_0^t G_{PE}(t)d\tau\, y = 2\pi k_x(t)x + 2\pi k_y(t)y \tag{2.14}$$

and where $k(t)$ is the *k*-space position that is introduced by the gradient

$$k(t) = \frac{\gamma}{2\pi}\int_0^t G(t)d\tau \tag{2.15}$$

Therefore the total signal intensity is

$$M(x,y,t) = \iint \rho(x,y)e^{i\omega t}\, e^{2\pi i[k_x(t)x+k_y(t)y]}dxdy \tag{2.16}$$

This equation reveals that the MRI signal can be described as the Fourier transformation of the spatial varying proton density $\rho(x)$, which can be selectively sampled using time varing gradient fields.

2.2.6 *k*-space trajectory

The previous section describes how the readout gradients determine the position of the *k*-space. Thus the *k*-space trajectory can be calculated through the applied gradients pulses. Several 2D *k*-space trajectories are illustrated in Figure 2.8.

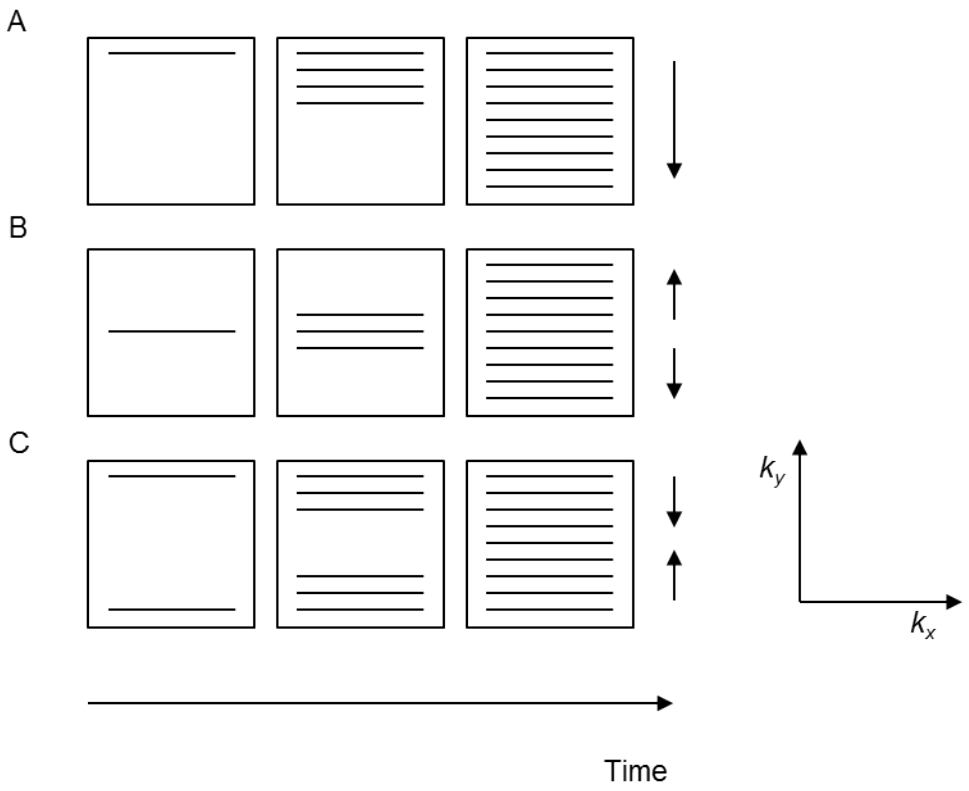

Figure 2.8 Three examples of 2D *k*-space view orderings. (A) Normal linear order. (B) Centre out and centre in order (C).

2.2.7 Three-dimensional imaging

Three-dimensional (3D) imaging extends 2D slice excitation into 3D volume excitation. A thick slab is excited in the 3D method for spatial encoding. A second phase encoding process, along the Z direction, is cycled through together with Y axis phase encoding and X axis frequency encoding. After the signal acquisition, the signals are processed using a 3D inverse Fourier transform to reconstruct the imaging volume. The 3D imaging usually acquires a line of k_x within one repetition time (TR), and the filling order in the k_y-k_z plane varies, some of these orders are illustrated in Figure 2.9.

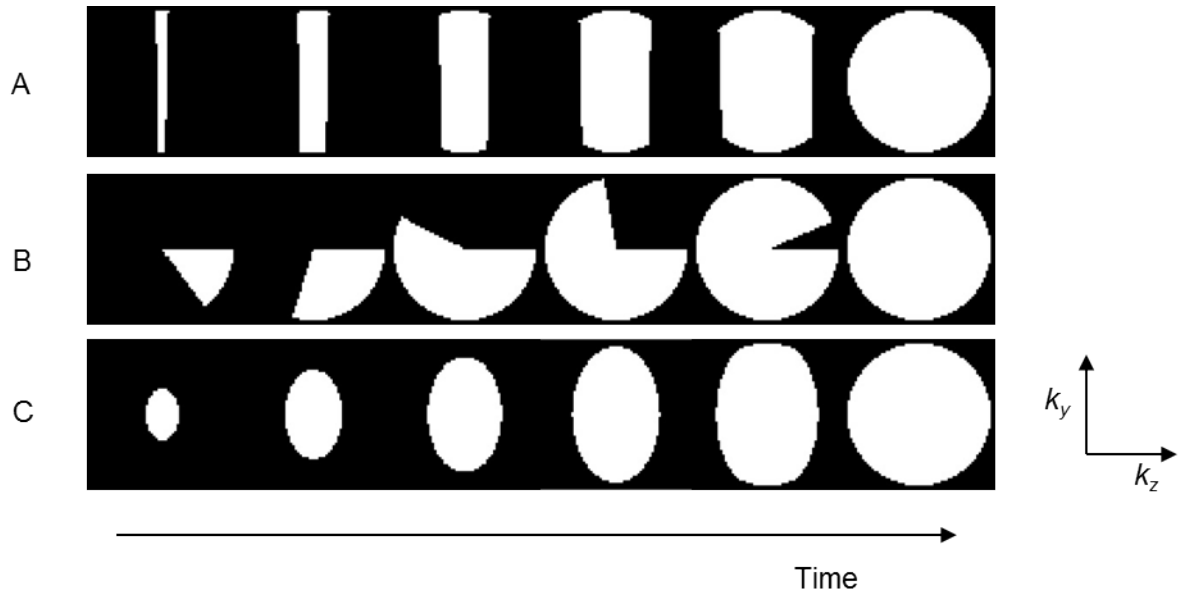

Figure 2.9 Three-dimensional *k*-space filling orders. (A) Centric out: the data acquisition starts from the centre of the k_z, and then acquires the both side of k_z. (B) Radial fan beam: the *k*-space points were first sorted by their polar angle into different segments, and in each segment, the points are acquired by their distance to the *k*-space centre. (C) Elliptic out: the data acquisition starts from the *k*-space centre to the edges.

2.2.8 Magnitude, phase, real and imaginary MR signal

The MR signal is of complex form, as Figure 2.10 shows.

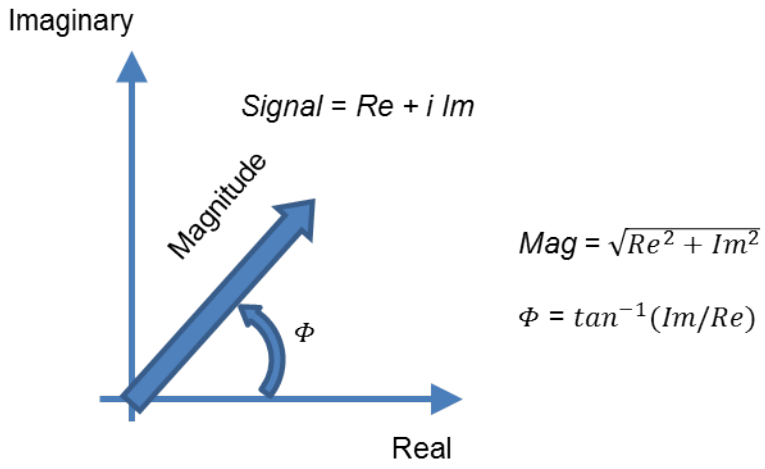

Figure 2.10 The complex MRI signal and its relationship with magnitude, phase, real and imaginary signal.

After the Fourier transformation, the complex image is manipulated into different types of images. Normally, the magnitude images are shown. Magnitude images are the absolute value of sum of square of real and imaginary parts. It shows mainly the anatomy of the

tissue. However, other images may be used for as well. For example, the phase image, calculated as the angle between the real and imaginary image, could be used for flow measurement. Figure 2.11 shows an example of four types of images.

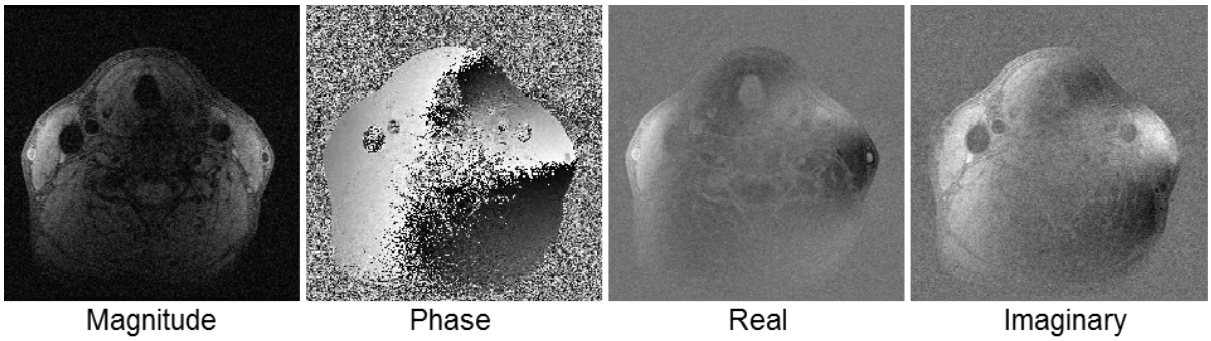

Figure 2.11 Four different types of images.

It has to be noted that the noise in the complex image is the white noise, which means it has equal intensity at different frequencies, or a constant power spectral density. However, after the real and imaginary combination, the MR magnitude images no longer have white noise. The noise distribution becomes Rician in the magnitude image. The Gaussian and Rician noise distribution are shown in Figure 2.12.

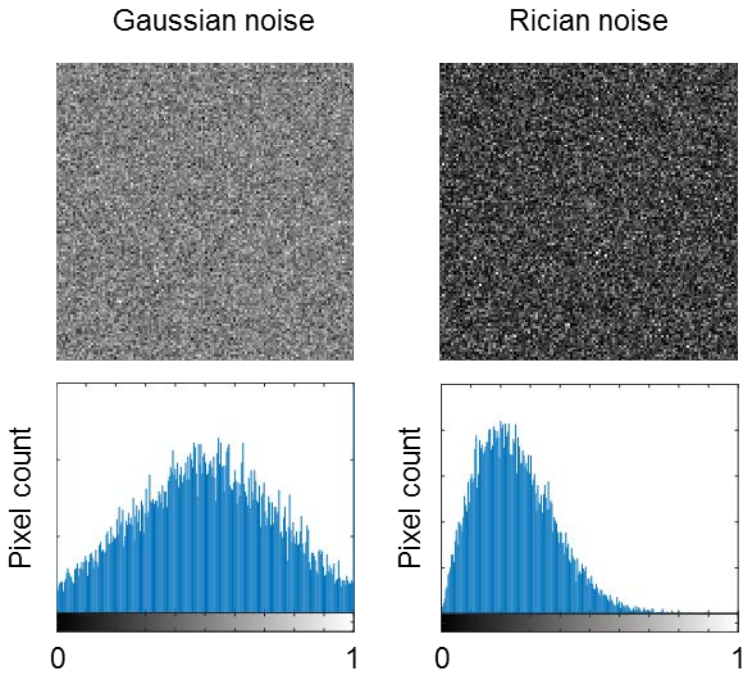

Figure 2.12 Examples of Gaussian and Rician noise images and their histograms.

The Gaussian and Rician distribution can be described as:

$$\mathrm{f}(x|\mu,\sigma^2) = \frac{1}{\sqrt{2\pi\sigma^2}} e^{-\frac{(x-\mu)^2}{2\sigma^2}} \tag{2.17}$$

$$\mathrm{f}(x|\mu,v,\sigma) = \frac{x}{\sigma^2} e^{-\frac{x^2+v^2}{2\sigma^2}} I_0\left(\frac{xv}{\sigma^2}\right) \tag{2.18}$$

where μ is the mean of the distribution, v is the noise and σ is the standard deviation.

2.2.9 Basic sequences

Spin echo

A spin echo is generated by a 90˚ excitation pulse followed by an 180˚ refocusing pulse. After the 90˚ pulse, the net magnetisation (the total magnetisation of all the spins) is tipped from the longitudinal direction into the transverse x-y plane. The spins then begin to dephase due to spin-spin relaxation and B_0 non-uniformity plus other susceptibility effects. After a certain time (half of the echo time, TE/2), the 180˚ pulse flips the transverse magnetisation, effectively inverting the phase. Since the phase is inverted the dephasing caused by the B_0 non-uniformity and other susceptibility effects is reversed and the spins will naturally rephase. forming a spin echo after a further time period of TE/2. The true spin-spin interactions are not rephased hence the signal is affected by T_2 decay. The pulse sequence of the spin-echo is shown as Figure 2.13A. The TE is defined as echo time.

In the spin echo, the signal is not affected by the B_0 non-uniformity as this effect is reversed by the refocusing 180˚ pulse. Therefore, the amplitude of the spin echo decreases purely with T_2 relaxation.

$$I(TE) = M_0 e^{-TE/T_2} \tag{2.19}$$

Gradient echo

The gradient recalled echo (GRE) sequence uses a gradient reversal instead of 180˚ RF pulse to produce the echo (Figure 2.13B). GRE typically uses a small flip angle pulses to avoid longitudinal magnetisation saturation when using short TRs. The B_0 non-uniformity is not compensated in the GRE, which makes the image T_2* weighted. Normally, a spoil gradient is applied at the end of GRE sequence, to eliminate any residue magnetisation and achieve short TR. This type of sequences is called spoiled GRE (SPGR). The signal intensity in SPGR is given by the following equation

$$I = M_0 \frac{\sin(\alpha)(1-e^{-TR/T_1})}{1-\cos(\alpha)e^{-TR/T_1}} e^{-TE/T_2^*} \quad (2.20)$$

where α is the flip angle, TR is the repetition time and TE is the echo time.

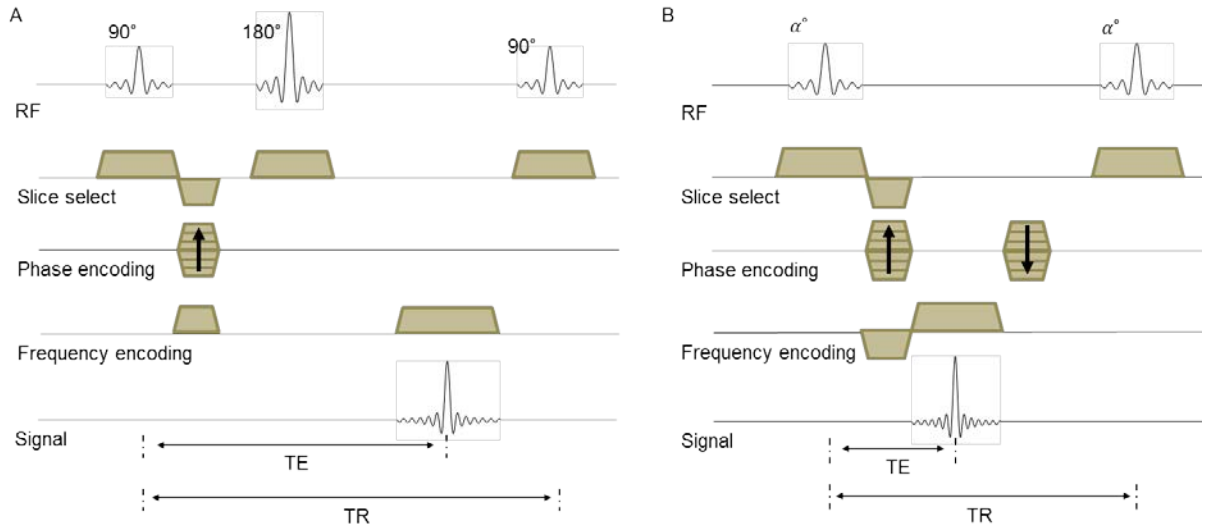

Figure 2.13 Diagrams of spin echo (A) and gradient echo without gradient spoiling sequence (B).

Fast spin echo (FSE)

FSE uses a train of refocusing pulses after the first excitation pulse, as Figure 2.14 shows. Multiple spin echoes are encoded as separate *k*-space lines within one TR. The number of echoes acquired in a single TR is called the echo train length (ETL). The time interval between two refocusing pulses is known as the echo spacing (ESP), and the time from the 90˚ pulse to the echo that is phase encoded closest to the centre of *k*-space centre is known as the effective TE, since the signals in the centre of *k*-space, i.e. the low spatial frequencies primarily affect the image contrast.

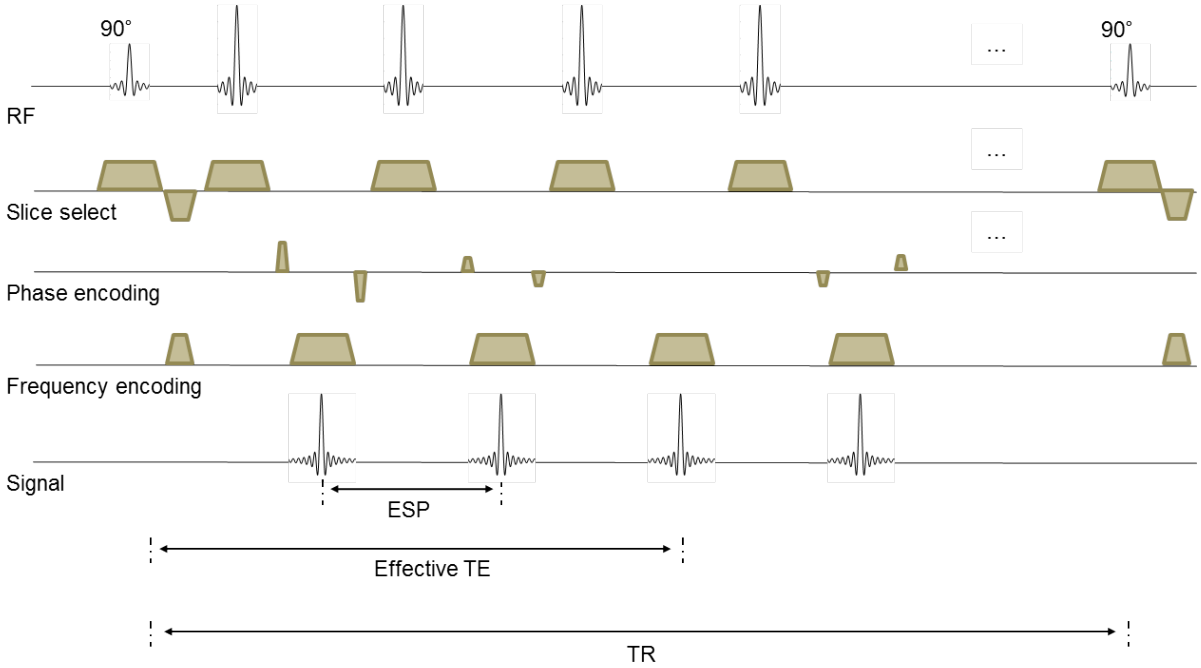

Figure 2.14 Diagram of a fast spin echo sequence. The number of echoes per TR is called Echo Train Length (ETL). ESP: echo spacing. The refocusing RFs can be 180° pulses or with variable flip angles. The signals in the diagram are only for demonstration and do not represent the actual amplitudes.

Due to scanning time, the 3D imaging requires more *k*-space lines in one TR thus a longer ETL is generally used to keep acquisition times as short as possible. If all the refocusing pulses are 180˚, the signals will decay rapidly according to the T_2 relaxation, leading to imaging blurring in the phase encode direction [97]. A series of refocusing pulse with variable flip angles can be used to reduce this effect. A simulation experiment demonstrating this principle is shown in Figure 2.15. The Bloch simulation is using a custom algorithm based on the code from Brian Hargreaves at Stanford University (http://mrsrl.stanford.edu/~brian/bloch/), using Matlab (MathWorks, Natick, MA, USA). The algorithm considers the rotation matrix of magnetisations in the three-dimensional space. By modulating the flip angles of the refocusing RF pulses, a static pseudo steady state may be established that exhibits relatively high signal for long ETLs [98, 99].

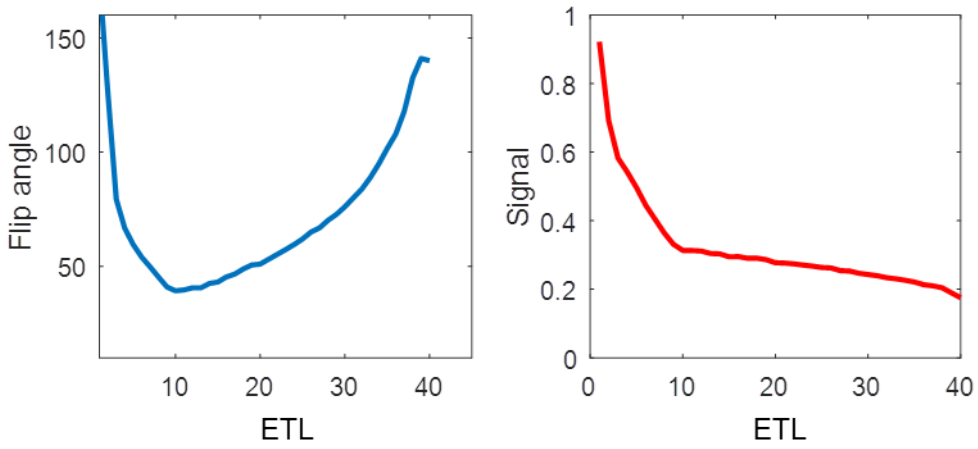

Figure 2.15 Diagram of 3D FSE flip angles and signal vs. ETL. ETL = 40 and MR properties of T_1 = 1000 ms, T_2 = 50 ms, esp = 4 ms are used in the simulation.

2.3 Contrast mechanisms

The spin relaxation described above could form three different types of image contrast, i.e. proton density (PD), T_1 and T_2 weighting. Different tissues, for example, have different T_1 and T_2 values [100]. Table 2.2 shows the common tissue T_1 and T_2 relaxation time at 1.5 T and 3 T [101-103].

Tissue	1.5 T		3 T	
	T_1 (ms)	T_2 (ms)	T_1 (ms)	T_2 (ms)
Skeletal muscle	1008 ± 20	44 ± 6	1412 ± 13	50 ± 4
White matter	884 ± 50	72 ± 4	1084 ± 45	69 ± 3
Gray matter	1124 ± 50	95 ± 8	1820 ± 114	99 ± 7
Blood	1441 ± 120	290 ± 30	1932 ± 85	275 ± 50
Plaque fibrous tissue	933 ± 272	60 ± 13	-	56 ± 9
Plaque lipid core	1044 ± 304	47 ± 14	-	37 ± 5

Table 2.2 T_1 and T_2 of common tissues at 1.5 T and 3 T.

2.3.1 Proton Density weighted contrast

In a PDw image, the tissue with a higher concentration of protons produces a higher signal and appears hyperintense in the image. In order to obtain a PDw image, the effect of T_1 and T_2 relaxation should be minimised. For example, in the spin echo sequence the TE should be as short as possible to minimise T_2 effects. Furthermore, a long TR is required to allow full T_1 recovery to minimise T_1 effects. Since TE cannot be infinitely short and TR cannot be infinitely long we refer to the contrast as proton density weighted.

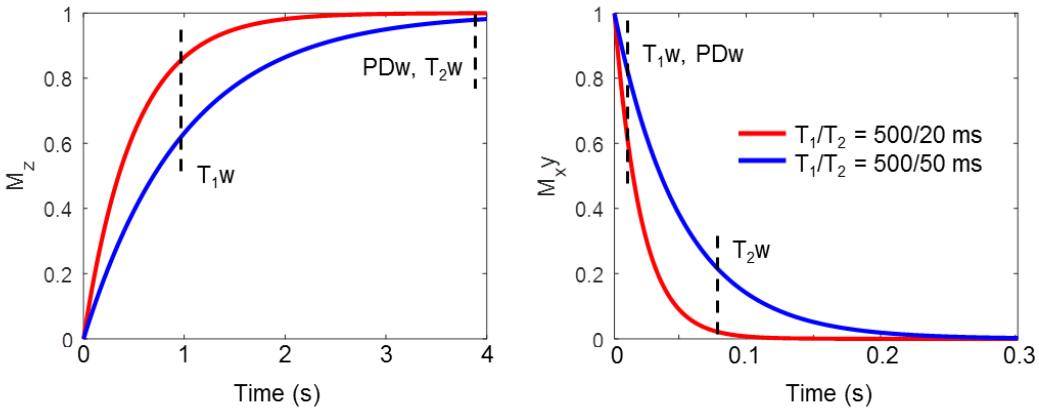

Figure 2.16 Diagram of signal evolution in generating image contrast using spin echo. The red and blue line represents two tissues with different T_1/T_2 values (red: T_1/T_2 = 500/20 ms, blue: T_1/T_2 = 1000/50 ms). Left: longitudinal magnetisation recovery and TR time. Right: transverse magnetisation dephases and TE times. Short TR and TE results in T_1w images. Long TR and short TE results in PDw image; Long TR and long TE results in T_2w images.

2.3.2 T_1 weighted contrast

In the T_1w images, the T_2 relaxation should be minimised by the use of the shortest possible TE. In T_1w images, the contrast is primarily controlled by the TR. With short TR, the image contrast is mainly determined by the tissue T_1 values. Tissues with short T_1 time have a faster longitudinal magnetisation recovery than tissues with longer T_1 times (Figure 2.16 left), resulting in signal hyperintensity.

2.3.3 T_2 weighted contrast

Similar to PDw images, the TR should be long enough to allow substantial recovery of longitudinal magnetisation. To introduce a T_2 weighting effect, the TE should also be long to allow sufficient spin-spin relaxation (Figure 2.16 right). Tissues with long T_2 result in signal hyperintensity in the image.

2.4 Quantitative measurements

In addition to traditional contrast weighing methods, MRI can also be used to quantify the tissue relaxation times. In carotid plaque imaging, quantitative MRI has been used to quantify the relaxation times of plaque components, such as fibrous tissue, lipid core, intraplaque haemorrhage, and calcification [104, 105], both in-vivo [104, 106, 107] and ex-vivo [102, 107-109]. Quantitative MRI allows direct measurement of the MR properties of plaque components, which mitigates the need to perform relative signal comparisons and

overcomes variability introduced by the surface coil position and field non-uniformities [110]. Quantitative measurements may therefore be more suitable across different MRI systems and multi-centre studies.

2.4.1 Quantitative T_1 measurement

There are several methods that can be used for T_1 measurement.

Inversion-recovery method

In an inversion-recovery sequence, an 180˚ pulse is applied to invert all the magnetisation within the imaging plane into the $-M_z$ direction. The magnetisations then recover via T_1 relaxation. The amount of T_1 recovery is controlled by the time interval between the 180˚ inversion pulse and the excitation pulse, known as the inversion time (TI). To achieve accurate T_1 measurement, the TR needs to be long and TE needs to be short enough. The T_1 relaxation time could be calculated from multiple acquisitions with different TIs:

$$I(TI) = M_0(1 - 2e^{-\frac{TI}{T_1}}) \tag{2.21}$$

The inversion recovery method is mainly used in 2D imaging. The T_1 measurement accuracy depends on the inversion pulse efficiency. Inaccurate flip angles caused by RF transmit field (B_1^+) nonuniformity may cause errors in T_1 measurement. Also, as the sequence needs to be repeated several times to achieve different TI time, the scanning time for this method is relatively long. However, poor slice profile in 2D may cause inaccuracy in the inversion recovery based T_1 measurement, especially at the edges of the imaging slice.

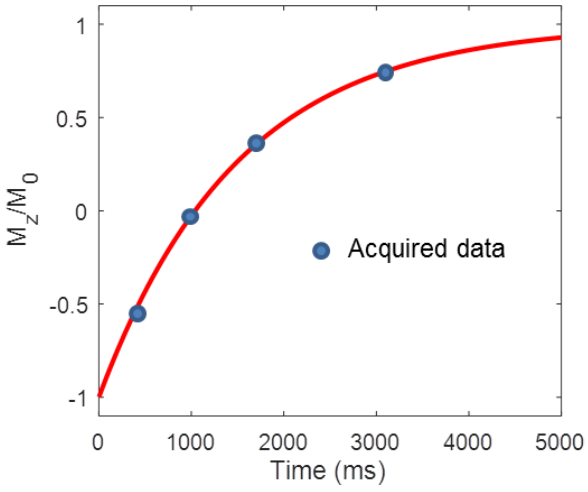

Figure 2.17 Inversion recovery based T_1 calculation. The material property of T_1 = 1500 ms is used for simulation.

Variable flip-angle method

This method determines the tissue T_1 value based on the spoiled gradient-echo signal shown in Equation 2.20. If the T_2^* effect can be ignored using the short TE, the signal intensity is a non-linear function of the flip angle α. Thus the measured signal at variable flip angles can be fitted to calculate the T_1 and M_0.

The method can be achieved in fast 3D T_1 mapping compared to the inversion pulse method, which overcomes the poor slice profile limitation in the 2D imaging. However, it requires very uniform flip angle throughout the image volume to get an accurate T_1 measurement. Therefore, additional B_1^+ nonuniformity correction is needed for large field-of-views.

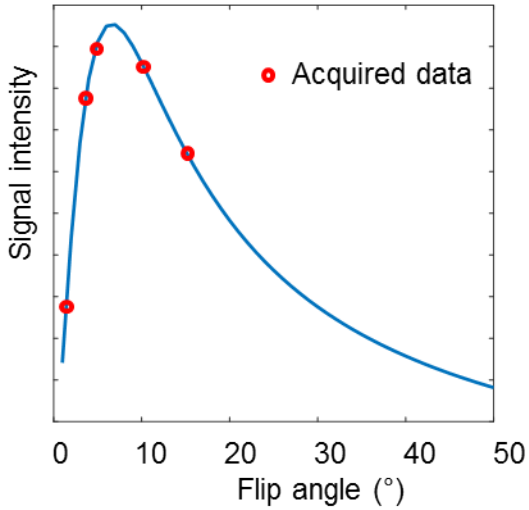

Figure 2.18 T_1 measurement using variable flip angle 3D SPGR sequence. Images are acquired at different flip angles. In this example, 2°, 3°, 5°, 10° and 15° is used.

2.4.2 Quantitative T_2 measurement

Quantitative T_2 measurement requires a long TR multi-echo spin-echo based sequence. The signal decays following the spin-spin relaxation described in Equation 2.19. Images with multiple echo times are needed for exponential fitting to calculate the T_2 values in the tissue. In real imaging cases, the images normally contain the noise floor, as Figure 2.19 shows.

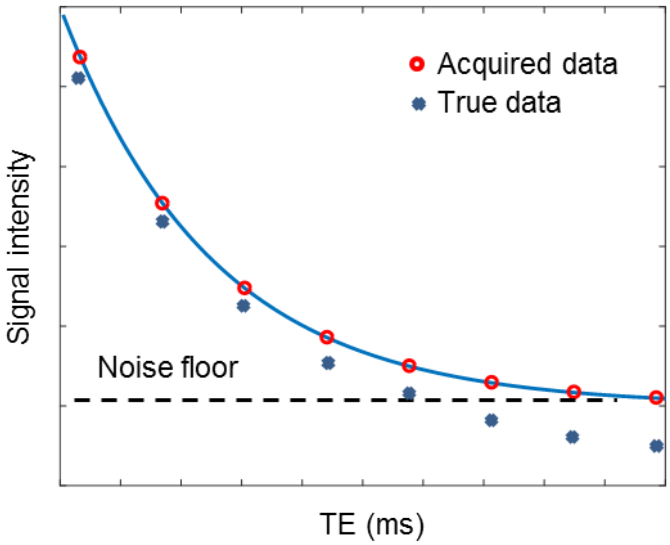

Figure 2.19 T_2 decay with image noise floor. The exist of noise floor will make calculated T_2 value to be higher than the true value.

With the noise floor, the Equation 2.19 becomes

$$I(TE) = M_0 e^{-TE/T_2} + offset \tag{2.22}$$

where the *offset* is the noise floor. Several methods could be used to take the noise floor into consideration. One method is to use a three-parameter fitting for each of the pixels. However, it requires more than three echoes in the sequence, which may be limited in some of the applications. Another method is to consider the noise floor is constant in the image, and subtract the noise floor before performing the two parameter fitting. Because of the sum-of-squares algorithm, the noise in the magnitude image has a Rician distribution [111]. Miller's method can be used to eliminate the noise [112]. In Miller's method, the complex signal can be written as

$$A = A_R + iA_I \tag{2.23}$$

where A_R and A_I are the real and imaginary part of the signal. If only the magnitude image is used, then

$$M = (A_R^2 + A_I^2)^{1/2} \tag{2.24}$$

The same consideration for the noise component:

$$N = N_R + iN_I \tag{2.25}$$

where the noise has standard deviation $\delta = (\langle N_R^2 \rangle)^{1/2}$ and average of zero. If the noise appears in the image:

$$S = A + N = (A_R + N_R) + i(A_I + N_I) \tag{2.26}$$

The magnitude image would be

$$M = [(A_R + N_R)^2 + (A_I + N_I)^2]^{1/2} \tag{2.27}$$

If we consider the square of the images:

$$M^2 = (A_R + N_R)^2 + (A_I + N_I)^2 = A_R^2 + A_I^2 + 2A_R N_R + 2A_I N_I \tag{2.28}$$

And

$$\langle M^2 \rangle = A_R^2 + A_I^2 + 2A_R \langle N_R \rangle + 2A_I \langle N_I \rangle = A^2 + 2\delta^2 \tag{2.29}$$

the noise contribution can be considered as a normal distribution with an average of zero. The corrected image is

$$M_c^2 = M^2 - M_0^2 \tag{2.30}$$

Therefore, the T_2 fitting can be simplified as two parameter fitting:

$$I^2(TE) = I_0^2 e^{-2TE/T_2} \tag{2.31}$$

This method can be applied to sequences of limited echo numbers.

2.4.3 Quantitative T_2* measurement

Similar to T_2 measurement, the T_2* measurement can be obtained using a multi-echo gradient echo based sequence. The signal decay in the GRE sequence is similar to spin-echo (SE) sequence, with the consideration of local field inhomogeneity. Miller correction is also applied to the T_2* measurement.

$$I(TE) = M_0 e^{-TE/T_2^*} \tag{2.32}$$

2.5 Blood suppression techniques

For vessel wall imaging, the flowing blood in the lumen produces artefacts which may make it difficult to identify the vessel wall, therefore blood suppressing preparation schemes are often required. Several blood suppression techniques which have been used in this thesis are described below.

2.5.1 Double inversion recovery (DIR)

Double Inversion recovery has been used extensively for vessel wall imaging. The DIR uses two 180˚ pulses to prepare the spins. Figure 2.20 shows the diagram of DIR preparation. The first 180˚ is non-selective which inverts all the magnetisations to $-M_z$. The second selective 180˚ pulse plays out immediately after the first one and selectively re-inverts the magnetisation within the imaging plane back to $+M_z$. The slice thickness for DIR pulse is usually thicker than the imaging slice to improve the blood suppression effectiveness. After the two pulses, the magnetisation inside the imaging plane remains unchanged while the spins outside the imaging plane undergo T_1 recovery from the $-M_z$ state. Due to the blood flow, the blood inside the imaging plane is gradually replaced by the blood outside the plane. The 90° excitation pulse is applied after a set time interval (of the inversion time, or TI) at which the blood signal crosses zero and hence should not generate any signal. An example of 2D FSE sequence with and without DIR is shown in Figure 2.21.

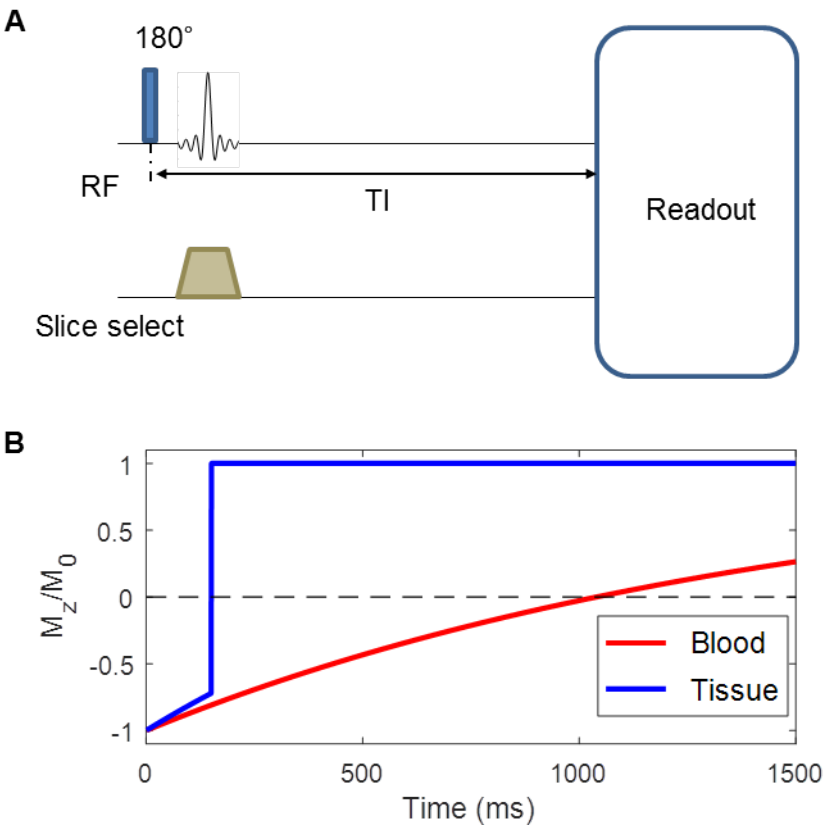

Figure 2.20 (A) Diagram of double inversion recovery (DIR). (B) Bloch simulation of blood outside the imaging plane and tissue inside the imaging plane responses to the preparation. Blood T_1 of 1500 ms is used in the simulation.

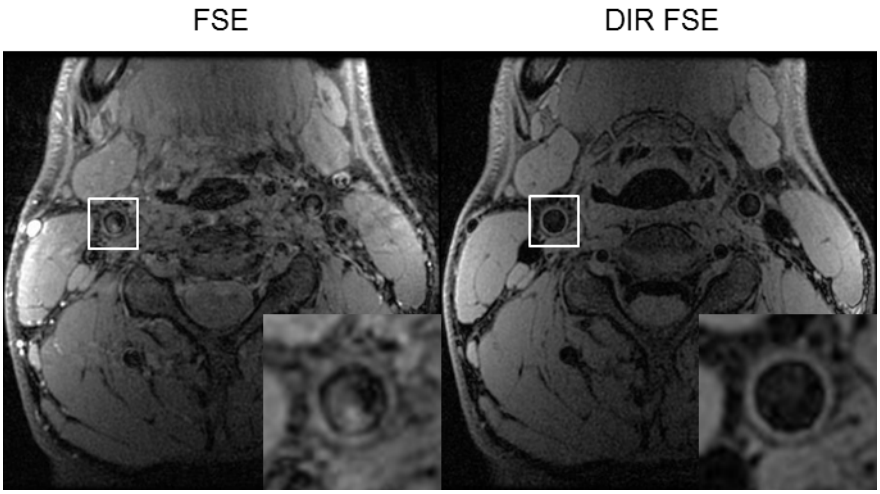

Figure 2.21 Example of 2D FSE without (left) and with DIR preparation (right).

2.5.2 Quadruple inversion rectory (QIR)

The DIR method described above utilises the T_1 recovery of the blood to achieve the desired suppression and hence requires prior knowledge of the blood T_1 value. However, if images are acquired post administration of a contrast agent, the considerable T_1 shortening effect of

the agent will render the blood suppression ineffective since the T_1 is unknown and hence the appropriate TI cannot be calculated. Therefore, QIR was introduced to achieved adequate blood suppression which is less sensitive to the T_1 changes in the blood, and also to ensure that there were no variable magnetisation transfer effects by using a different TI pre and post contrast [87]. QIR consists of two double-inversion modules followed by two delays, as shown in Figure 2.22(A). Within each double inversion, a non-selective RF pulse is applied immediately followed by a slice-selective pulse. The signal for the blood is:

$$I = 1 - \frac{2\exp(-TI_2/T_1)[1-\exp(-TI_1/T_1)]}{1-\exp(-TR/T_1)} \tag{2.33}$$

In Figure 2.22(B), blood with a wide range of T_1 values can be suppressed.

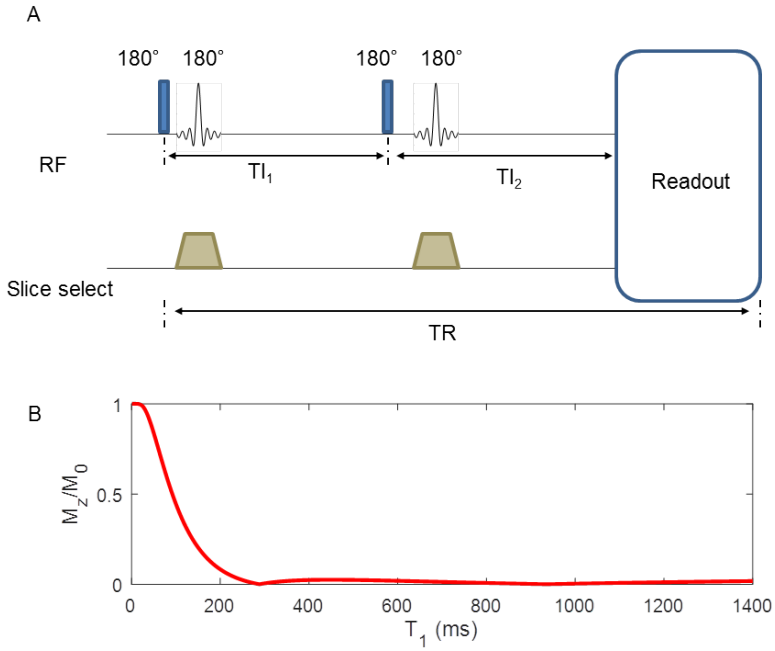

Figure 2.22 (A) Diagram of quadruple inversion recovery (QIR). (B) Bloch simulation of QIR response of varies blood T_1 values. TR = 800 ms, TI_1 = 373 ms and TI_2 = 126 ms are used in the simulation.

Due to the complicated flow patterns caused by the carotid bifurcation, the 2D blood suppressions mentioned above are frequently compromised by artefacts, which bring difficulty when segmenting the vessel wall. This is mainly due to the insufficient blood suppression. In recent years, three-dimensional blood suppression techniques which use non-selective pulses were introduced to achieve better blood suppression.

2.5.3 Motion sensitive driven equilibrium (MSDE) and improved MSDE (iMSDE)

The MSDE and iMSDE blood suppression methods were introduced by Wang et al in 2007 [88] and 2010 [113]. They comprise two non-selective 90˚ pulses to tip-down and tip-up the magnetisations of both blood and tissue in the preparation. Between the two 90˚ pulses, MSDE method utilises a single non-selective 180˚ pulse with two crusher gradients to dephase the moving spins (Figure 2.23A); The iMSDE method utilises two non-selective 180˚ pulses and four crusher gradients for dephasing (Figure 2.23B). The iMSDE method demonstrates better soft tissue Signal-to-Noise Ratio (SNR) and Contrast-to-Noise Radio (CNR) and is less influenced by the transmit field non-uniformity with respect to the MSDE method [113].

To consider the mechanism of MSDE preparation, the phase shifts of the moving spins can be described as [114]

$$\varphi = \gamma \int \boldsymbol{G}(t)\boldsymbol{x}(t)dt \tag{2.34}$$

where γ is the gyromagnetic ratio, $\vec{G}(t)$ is the gradient amplitude and $\vec{x}(t)$ is the location of the spins. The $\vec{x}(t)$ can be expanded with the the Taylor series:

$$x(t) = x_0 + \boldsymbol{v}_0 t + \frac{1}{2}\boldsymbol{a}_0 t^2 + \cdots \tag{2.35}$$

so the phase can be written as

$$\varphi = \gamma \int \boldsymbol{G}(t)\left(x_0 + \boldsymbol{v_0} t + \frac{1}{2}\boldsymbol{a_0} t^2 + \cdots\right) dt \tag{2.36}$$

$$\varphi = \gamma m_0(t) x_0 + \gamma m_1(t)\boldsymbol{v_0} + \frac{\gamma}{2} m_2(t)\boldsymbol{a_0} + \cdots \tag{2.37}$$

The m_n is defined as the nth gradient moment:

$$m_n(t) = \int_0^t G(u)u^n du \tag{2.38}$$

For moving spins, the higher order terms can be omitted [115]; so the signal attenuation in a voxel depends on the velocity distribution within this voxel $\kappa(v)$ and is proportional to the first gradient moment $m_1(t)$:

$$\eta = \mu \int_0^{\infty} \kappa(v) e^{-j\gamma\bar{v}\int_0^{t-} G(u)udu} dv = \mu \int_0^{\infty} \kappa(v) e^{-j\gamma m_1(t)\bar{v}} dv \quad (2.39)$$

where the signal attenuation coefficient η is used to describe the signal lose caused by the velocity distribution and first gradient moment, v is the velocity of the moving spins.

For the non-moving spins, the gradients either side of the 180˚ pulses are compensated and are therefore not influenced by the dephasing gradients. The static tissue undergoes the T_2 decay during the MSDE or iMSDE preparation.

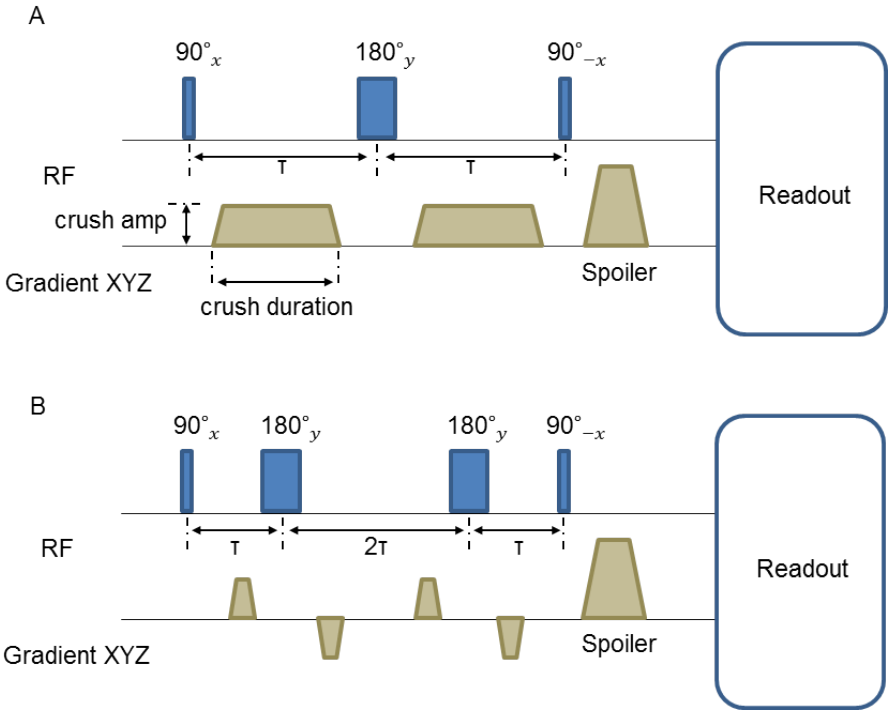

Figure 2.23 Diagram of original MSDE (A) and (B) improved (iMSDE) preparation.

2.5.4 Delay alternating with nutation for tailored excitation (DANTE)

The DANTE blood suppression method was introduced by Li et al in 2012 [89]. It comprises a train of small flip angle pulses with interleaved gradients pulses, as shown in Figure 2.24. To consider a spin with a constant velocity v along the applied gradient, the phase accumulation of the spins between the (n-1)th and nth pulse is described as

$$\Delta\varphi(n) = \gamma \int_{(n-1)t_D}^{nt_D} \vec{G}(t)\vec{x}(t)dt = \gamma\left(x_0 + \frac{1}{2}v\right)Gt_D + n\gamma vGt_D^2 = \varphi_0(v) + n\varphi_1(v) \quad (2.40)$$

where γ is the gyromanetic ratio, x(t) is the location of the spin at time t. This phase can be understood as a constant phase increment (φ_0) and a time-varying, increasing increment ($n\varphi_1$).

For the static spins, the phase will increase linearly with fixed increment, leading to a phase coherent signal. For the moving spins, the phase increment increases with the time (n), resulting in overall quadratic phase. The quadratic or higher order phase accumulation will result in magnetisation spoiling [116], achieving the black-blood effect.

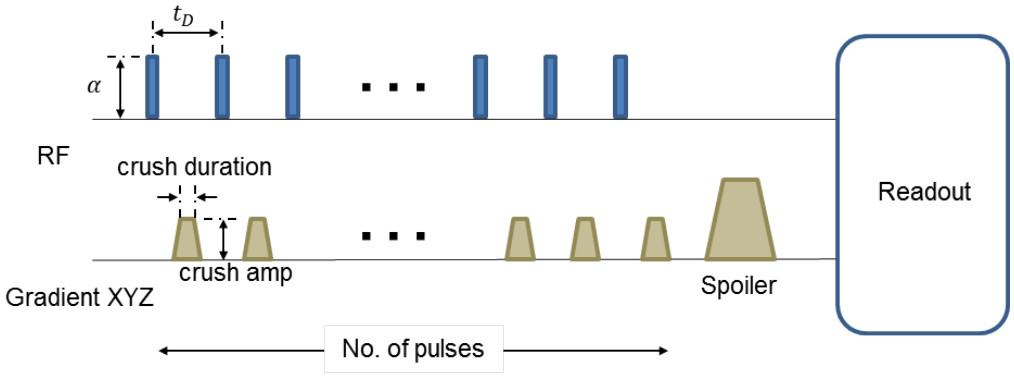

Figure 2.24 Diagram of DANTE preparation. A train of RF and gradient pulses is used in the preparation. α is the flip angle. t_D is the repetition time of the DANTE pulses.

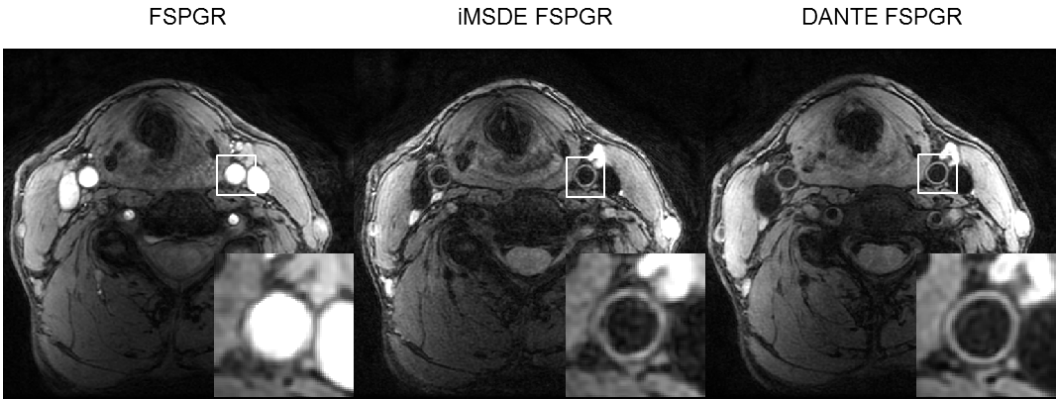

Figure 2.25 An example of volunteer images using fast spoiled gradient echo sequence (FSPGR), without blood suppression (left), with iMSDE (middle) and DANTE preparation (right).

Chapter 3 Relationship between carotid plaque surface morphology and perfusion: a 3D Dynamic contrast-enhanced MRI study

This chapter evaluates the relationship between plaque surface morphology and neovascularization using a high temporal and spatial resolution 4D contrast-enhanced MRI/MRA sequence. The specific hypotheses for this chapter are

> *[Hypothesis 1]* plaque functional characteristics and surface morphology can be evaluated using a high temporal and spatial resolution 4D contrast-enhanced MRI/MRA sequence.
>
> *[Hypothesis 2]* there is a difference in pharmacokinetic parameters between the ulcerated and smooth carotid plaques.

Aspects of this work have been published in Magnetic Resonance Materials in Physics, Biology and Medicine (2017): 1-9 [117].

3.1 Theory

Dynamic Contrast-Enhanced (DCE)-MRI has been demonstrated as a non-invasive method to quantify the extent of neovasculature within diseased tissue, for instance, tumour [118] or carotid plaques [119, 120], with high accuracy and reproducibility. It acquires high temporal resolution MR images before and after the injection of gadolinium (Gd) based contrast agents. Image acquisition normally uses a time-resolved spoiled gradient echo sequence [121]. The acquired signal intensity was given by Equation 2.20. With short TE and TR, the T_2* effect can be eliminated, thus the tissue T_1 can be calculated from the image signal directly.

The use of gadolinium could reduce the tissue's T_1 value. The relationship between the gadolinium concentration and inversion of T_1 value is approximately linear

$$r[Gd] = \frac{1}{T_1} - \frac{1}{T_{1,0}} \tag{3.1}$$

where the r is the reflexivity of the contrast agent, and $T_{1,0}$ is the original T_1 of the tissue without contrast agent. By measuring the signal changes before and after the injection, the gadolinium concentration in the tissue can be calculated.

To calculate the pharmacokinetic parameters, several factors need to be considered, including:

Artery input function (AIF)

The AIF describes how the contrast concentration changes with time in the vessels feeding the tissue of interest. It therefore governs the rate that contrast will go into the tissue of interest. There are currently four categories of determining the AIF:

1. Gold standard AIF

The gold standard AIF requires an arterial catheter inserted into the subject [122]. This method could accurately measure the contrast concentration in plasma (C_p) at the subject level over time. However, obvious disadvantages for this technique are (a) its invasive approach is inconvenient for patients; and (b) it is not suitable for tissues without large feeding vessels, such as in the breast.

2. Population-based AIF

Population-based AIFs measure the blood supply in a number of subjects and uses the average value for subsequent larger population studies [123]. The biggest advantage of this method is that no additional measurement is required and it's very easy and simple to apply. Limitations of this technique are that the individual variations in each of the subject AIFs are ignored.

3. Subject-based AIF

This method measures the specific AIF of each subject [124, 125]. In each scan, the AIF is measured from the artery lumen. This method considers individual variability which ensures the DCE result to be more accurate. However, this method requires that big vessels must be inside the region of interest which may not be suitable for some situations, such as the breast. Image artefact due to motion may also influence the accuracy of this method.

4. Reference tissue based AIF

This method uses the signal changes in a well characterised, healthy reference tissue (such as muscle), to calibrate the contrast concentration within the region of interest [126]. The

signal change in the healthy tissue is used to inversely derive the AIF [126]. However, this method can only apply to the simple DCE models which do not model v_p [127].

Compartmental models

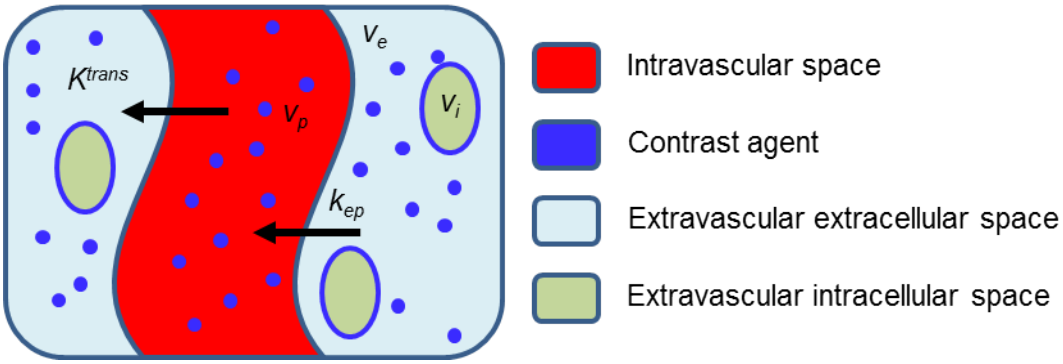

Figure 3.1 A schematic tracer of kinetic modelling. K^{trans} and k_{ep} is the forward and reverse transfer constant from the blood plasma to tissue. v_p, v_e and v_i are the volume fraction of blood plasma and extravascular extracellular/intracellular space.

Parameters related to tissue neovascularization (shown in Figure 3.1) can be calculated by analysing the concentration curves. The relationship between the kinetic parameters can be described as:

$$\frac{\mathrm{d}C_e(t)}{\mathrm{dt}} = \frac{K^{trans}}{v_e}[C_p(t) - C_e(t)] \tag{3.2}$$

$$C_t(t) = v_p C_p(t) + v_e C_e(t) \tag{3.3}$$

$$1 = v_p + v_e + v_i \tag{3.4}$$

where C_p is concentration change over time in plasma and C_t is the concentration in tissue, K^{trans} is the forward transfer constant from blood plasma to tissue and k_{ep} is the reverse constant. v_p, v_e and v_i are the volume faction of blood plasma and extravascular extracellular/intracellular space.

There are several pharmacokinetic models to solve the above equations. The Toft's model is the most commonly used DCE model [128]. It measures the signal changes in plasma (C_p) and tissue (C_t) to calculate the forward transfer constant K^{trans} and reverse constant k_{ep}, and assume that the tissue is weakly vascularized (v_p = 0).

$$C_t(t) = K^{trans} \int_0^t C_p(t') e^{-k_{ep}(t-t')}\, dt' \quad (3.5)$$

However, Toft's model may not be suitable for tissues like a tumour which is heavily vascularized. Thus, the extended Toft model overcomes this limitation by considering the vascular contribution [129]

$$C_t(t) = v_p C_p(t) + K^{trans} \int_0^t C_p(t') e^{-k_{ep}(t-t')}\, dt' \quad (3.6)$$

If the reverse constant k_{ep} can be eliminated, then the extended Toft model can be simplified using Patlak's model [130]

$$C_t(t) = v_p C_p(t) + K^{trans} \int_0^t C_p(t')\, dt' \quad (3.7)$$

For carotid imaging, the carotid artery can provide sufficient information about the AIF and Patlak's model has been shown to be the most reproducible [120]. We have therefore chosen to use subject-based AIFs and Patlak's model to investigate *[Hypothesis 1]* and *[Hypothesis 2]*.

3.2 Introduction

The appearance on X-ray angiography of plaque surface irregularity, or ulceration, has been correlated with increased risk of ischemic stroke [32]. This correlation applies for both moderate and severe stenosis [32]. Histological analysis of the carotid plaques after endarterectomy also indicates that ulceration is significantly more common in symptomatic patients compared with embolic stroke [29]. Ulceration has also been associated with high-risk factors including plaque rupture, intraplaque haemorrhage and a large lipid-rich necrotic core (LRNC) [41], indicating this is a sensitive marker of plaque instability [41] and risk of stroke [7, 30, 32]. Noninvasive imaging modalities offer high accuracy for ulcer detection as well as stenosis measurement [131-133]. Among different imaging modalities, contrast-enhanced MR angiography provides high-resolution imaging allowing visualisation of plaque ulceration [1, 79, 131].

In this study we applied a 4D sequence [134] which acquires data suitable for contrast enhanced (CE) MRA and dynamic contrast-enhanced (DCE) MRI processing. DCE-MRI has been demonstrated as a non-invasive method to quantify the extent of neovasculature within

carotid plaques with high accuracy and reproducibility [120, 135]. Previous studies using DCE-MRI have shown that plaque neovascularization is closely associated with high-risk features, such as inflammation [136], and is related to ischemic events [137]. In this study, we investigated the correlation between plaque surface morphology and neovascularization.

3.3 Materials and Methods

Experimental Methods

The study protocol was reviewed and approved by the local ethics committee and written informed consent was obtained (the patients are from MRCON study: Evaluation of role of contrast enhanced MRI in carotid atherosclerosis. R&D number: A092483. REC reference number:13/EE/0421). Twenty-one patients who had a carotid stenosis of at least 40% on Duplex ultrasound using NASCET criteria [138] were recruited. Ten were symptomatic (nine males, mean age 72 years, range: 59-86 years) with a recent history (less than 6 months) of transient ischemic attack (TIA), and eleven were asymptomatic (seven males, mean age 78 years, range: 68-87 years).

MRI protocol

Imaging was performed on a 3 T system (MR750, GE Healthcare, Waukesha, WI), using a four channel phased-array neck coil (PACC, MachNet, Roden, The Netherlands). The Time-Resolved Imaging of Contrast KineticS (TRICKS) method [134] was performed to obtain 4D CE-MRI and MRA data with a reconstructed spatial resolution of 0.3×0.3×0.7 mm^3. A coronal imaging slab was centred at the carotid bifurcation on the side with the highest degree of stenosis. The coronal acquisition plane was chosen to minimise the inflow artefact from the blood, and achieve better longitudinal coverage. No spatial saturation was applied. Total acquisition time was 6 min 23 s, to obtain a mask image and 30 view-shared phases with a temporal resolution of 10.6 s. Coincident with the third phase, a bolus of 0.1 mmol/kg Gd-DTPA (Gadovist, Bayer Schering, Berlin, Germany) was administered using a power injector at the rate of 3 mL/s followed by a 20 mL saline flush. The CE-MRA data was obtained by subtracting the mask image from the multi-phase acquisition. In addition, for plaque component determination, the following sequences were also performed in the coronal plane: pre- and post-contrast 3D T_1-weighted (T_1w) DANTE-prepared fast spin echo [139], 3D TOF and 3D direct thrombus imaging (MR-DTI, inversion time of 300 ms) [140]. Detailed imaging parameters are listed in Table 3.1. Total scanning time was approximately 30 mins.

Sequence	3D TOF	Pre/Post-contrast BB T_1w 3D FSE	3D DTI	4D DCE/MRA
Flip angle (°)	20	Variable flip angle	30	20
TE/TR (ms)	2.2/5.9	16.9/540	4.2/8.6	1.5/3.9
FOV (mm×mm×mm)	140×140×64	140×140×67	160×160×66	140×140×62
Acquired pixel size (mm×mm×mm)	0.5×0.5×2.0	0.6×0.6×1.4	1.0×1.0×1.0	0.6×0.6×1.4
Reconstruction pixel size (mm×mm×mm)	0.5×0.5×2.0	0.3×0.3×0.7	0.3×0.3×1.0	0.3×0.3×0.7
NEX	2	2	1	1
Receiver Bandwidth (±kHz)	31.25	62.5	25	62.5
Acquisition Time	1 min 35 s	2×6 min 26 s	4 min 42 s	6 min 23 s*

Table 3.1 Scanning parameters of the high-resolution 3D protocol. * temporal resolution of 10.6 s.

Image analysis

The T_1w and DCE images were reformatted into the axial plane with a 0.7 mm slice thickness using a dedicated workstation (AW4.6, GE Healthcare, Buc, France). For each patient, the carotid arteries on both sides were analysed. Carotid vessel wall and lumen boundaries at each slice were manually drawn according to the T_1w images, using a DICOM (Digital Imaging and Communications in Medicine) viewer (OsiriX 5.5.2, Pixmeo, Geneva, Switzerland). The plaque was defined as a focal wall thickness ≥ 1.5 mm [141]. The subtracted CE-MRA image at the fifth phase, which had the highest image contrast in the carotid artery, was used for morphological analysis. Plaque surface morphology was classified as either ulcerated/irregular or smooth using maximum intensity projection (MIP) images derived from the CE-MRA images, based on previously published standards [41], by two experienced reviewers, both having more than two years of experience in carotid imaging. The two reviewers were blinded to the patients' clinical information and made their judgment independently. The classification results from the first reviewer were used for further analysis. Luminal stenosis was measured for each plaque on both CE-MRA MIP and

3D pre-contrast T_1w images separately according to the NASCET criteria [138, 142]. The stenosis measurements obtained from the CE-MRA MIP images were used for further analysis as previous work has demonstrated that this method has high Intra- and inter-observer agreement [32]. IPH was defined as hyperintense signal using the DTI technique.

Pharmacokinetic modeling

Images from the 4D data were processed using the University of Washington (Seattle) Vasa Vasorum Imaging (VVI) tool [119]. This approach firstly applies a Kalman Filtering Registration and Smoothing (KFRS) algorithm, to reduce the noise level in the image and correct patient motion [143]. A two-compartment Patlak model is then used to generate a parametric map known as the "vasa vasorum image (VVI)" showing partial plasma volume (v_p) in shades of red and transfer constant (K^{trans}) in shades of green. The relationship between blood and tissue signal concentration is modelled as Patlak model (Equation 3.7).

Lumen and wall boundaries manually segmented from T_1w images were copied to the VVI. Manual adjustments were performed, as necessary to co-register the ROIs to the VVIs, by the reviewers who were blinded to the final results. Further details of the analysis can be found in Kerwin et al [119]. Adventitial pharmacokinetics (PK) measurements were calculated by averaging all the pixels along the wall boundary. Plaque PK measurements were calculated by averaging all the pixels between the wall and lumen boundary. The overall PK parameters of each plaque were calculated as the mean value across all the plaque containing slices. To test the interrater reproducibility of this method, two reviewers performed the analysis independently for all of the patients.

The PK parameter differences were evaluated using both linear and non-linear assumptions for signal intensity and Gd concentration. For the linear assumption, the signal intensity of each pixel at different frame was used directly in the Patlak model (Equation 3.7) to calculate the PK parameters. For the non-linear assumption, the signal intensity was used to calculate the pixel T_1 values in enhanced images based on Equation 2.20, with the first unenhanced image as the initial state. Then Equation 3.1 was used to convert the pixel T_1 values to actual Gd concentration (mmol/L). T_1 and $T_{1,0}$ (s) is the current and native pixel T_1 values (blood $T_{1,0}$ = 1500 ms and vessel wall $T_{1,0}$ = 1000 ms from the literature value [144] were used). The corrected Gd concentration was then applied again to the 28 arteries using the Patlak model. The calculated PK parameters were then compared with the results from the linear assumption.

Statistical analysis

The statistical analysis was performed using R (version 3.2.2, R Development Core Team, Vienna, Austria) [145]. The Shapiro–Wilk's test was used to test normality assumptions. The Kappa statistic was performed to evaluate interrater agreement in ulceration detection. The Student's t-test was used to compare the PK parameters for smooth versus ulcerated/irregular plaques defined by the first reviewer, and also to compare haemorrhage and non-hemorrhage plaques. Pearson's correlation was used to assess the relationship between PK parameters and luminal stenosis. The concordance correlation coefficient (CCC) was reported to assess the relationship between the stenosis measured by CE-MRA and 3D T_1w images. The CCC and Bland-Altman plots were used to compare the differences between linear and non-linear assumptions of image signal and Gd concentration. The inter-rater agreement in PK parameters was assessed using the intraclass correlation coefficient (ICC). A Chi-squared test was used to compare proportions of patients with IPH. Parametric distributions were presented as the mean ± standard deviation (SD). p-values < 0.05 were considered statistically significant.

3.4 Results

Of the 21 patients, three patients did not finish the examination due to discomfort, four carotid arteries were excluded from data analysis due to motion artefacts and four arteries were excluded due to occlusion. The rest of the images were of diagnostic quality, and used for further analysis. Atherosclerotic plaques were identified in the remaining 28 arteries, with a mean luminal stenosis of 44% (range 10 to 80%). Fourteen plaques were classified as ulcerated/irregular and fourteen were classified as smooth. Of the 28 arteries analysed, the two independent reviewers were in agreement for plaque surface morphology classification in 26 (93%) cases ($\kappa = 0.79$; 95% CI, 0.56 to 1.00). There was no evidence to suggest that the PK parameters (K^{trans} and v_p in adventitia and plaque) were not normally distributed ($p > 0.05$). For the luminal stenosis, the correlation between CE-MRA and 3D T_1w was good ($r = 0.89$).

The images in Figure 3.2 are from a symptomatic patient, with a 52% stenosis on the right side. The plaque contains a large IPH. Figure 3.2(C) shows the intra-luminal and adventitial signal change with time following contrast agent administration.

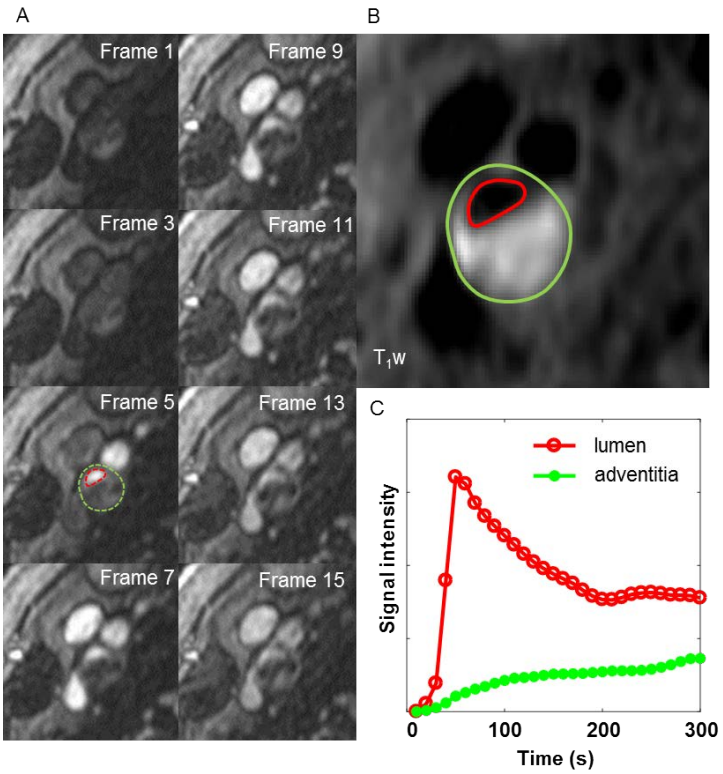

Figure 3.2 (A) shows DCE images at different time frames at a single slice location within an internal carotid artery (ICA) branch of the plaque. The dashed red and green lines in frame 5 show the boundary of carotid lumen and adventitia. (B) shows the corresponding black blood T_1w image with red and green lines delineating the lumen and wall boundary. (C) represents the mean signal intensity time course within the lumen (red) and adventitia (green). With permission [117].

Figure 3.3 is the same artery and shows the multi-contrast MR images and calculated VVI. An ulceration can be clearly seen on the CE-MRA images, but is not so apparent on the 3D TOF-MRA. Surface irregularity can be observed in both pre- and post-contrast T_1w images. The MR-DTI shows a large region of IPH. The VVI shows regions of high K^{trans} around the ulceration and at the adventitia boundary, with a relatively low K^{trans} inside the IPH.

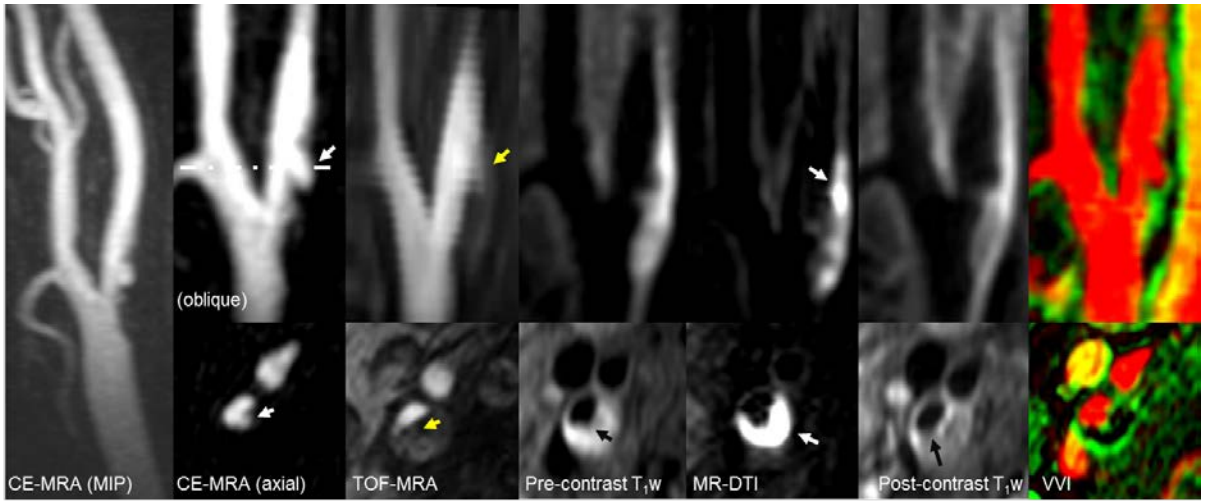

Figure 3.3 An ulcerated plaque in the multi-contrast MR protocol, including MIP from CE-MRA, oblique and axial reformat of CE-MRA, TOF-MRA, T_1w, DTI, CE-T_1w and VVI. The white arrow in CE-MRA suggests the ulcer arises perpendicularly from the lumen. The ulcer can be clearly seen on the CE-MRA images, while it is not clearly visible on the TOF-MRA images. The pre-contrast T_1w image shows the lumen surface irregularity, and a thin or ruptured FC can be seen on the post-contrast T_1w images (black arrow). The hyperintense area on MR-DTI represents a large intraplaque haemorrhage/thrombus (white arrow). The VVI shows the v_p in red channel, ranging from 0 to 65%, and K^{trans} in green channel, ranging from 0 to 0.5 min^{-1}. The VVI shows a high K^{trans} region around the ulceration and at the adventitia. With permission [117].

Figure 3.4 shows an example of smooth plaque with corresponding VVI. The adventitial and plaque K^{trans} in ulcerated/irregular plaques were significantly higher compared to smooth plaques (Figure 3.5A and B, adventitial $K^{trans:}$ 0.079 ± 0.018 vs. 0.064 ± 0.011 min^{-1}, p = 0.02; plaque K^{trans}: 0.065 ± 0.013 vs. 0.055 ± 0.010 min^{-1}, p = 0.03, respectively). Whilst v_p demonstrated no significant difference between groups (Figure 3.5C and D, adventitial $v_{p:}$ 9.3 ± 5.3% vs. 9.8 ± 4.8%, p = 0.81; plaque $v_{p:}$ 13.5 ± 5.5% vs. 11.8 ± 4.9%, p = 0.32, respectively).

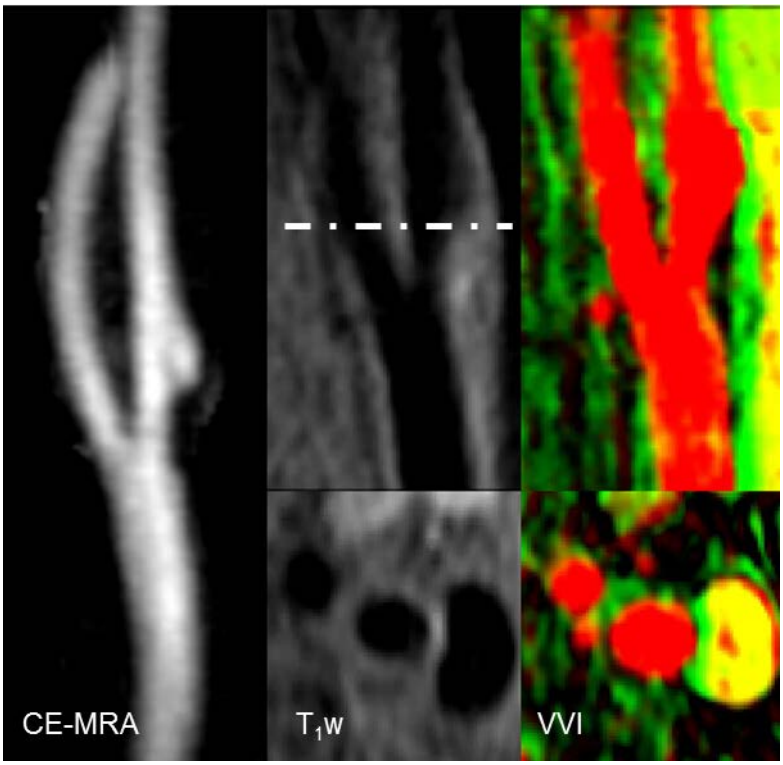

Figure 3.4 Images from a symptomatic patient with a smooth plaque and 20% stenosis. There were no regions of high K^{trans} observed within the plaque. The VVI shows the v_p in red channel, ranging from 0 to 65%, and K^{trans} in green channel, ranging from 0 to 0.5 min^{-1}.

Positive correlations between adventitial K^{trans} and v_p with the degree of stenosis were observed (r = 0.46, p = 0.01 for adventitial K^{trans}; r = 0.55, p = 0.01 for adventitial v_p, respectively). While no significant correlation was observed for plaque K^{trans} or v_p with stenosis (r = 0.23, p = 0.24 for plaque K^{trans}; r = 0.13, p = 0.96 for plaque v_p, respectively).

The non-linear correction of signal intensity with Gd concentration had little influence on the calculated PK values. Figure 3.6 shows VVI computed using the linear and non-linear assumptions and compare signal intensity with Gd concentration. The CCC comparing the linear and non-linear assumptions for adventitial K^{trans}, plaque K^{trans}, adventitial v_p and plaque v_p were: 0.95, 0.93, 0.99 and 0.99, respectively. There was highly significant concordance between the linear or non-linear assumptions (all $p < 0.001$). Figure 3.7 demonstrated the Bland-Altman plots comparing both assumptions.

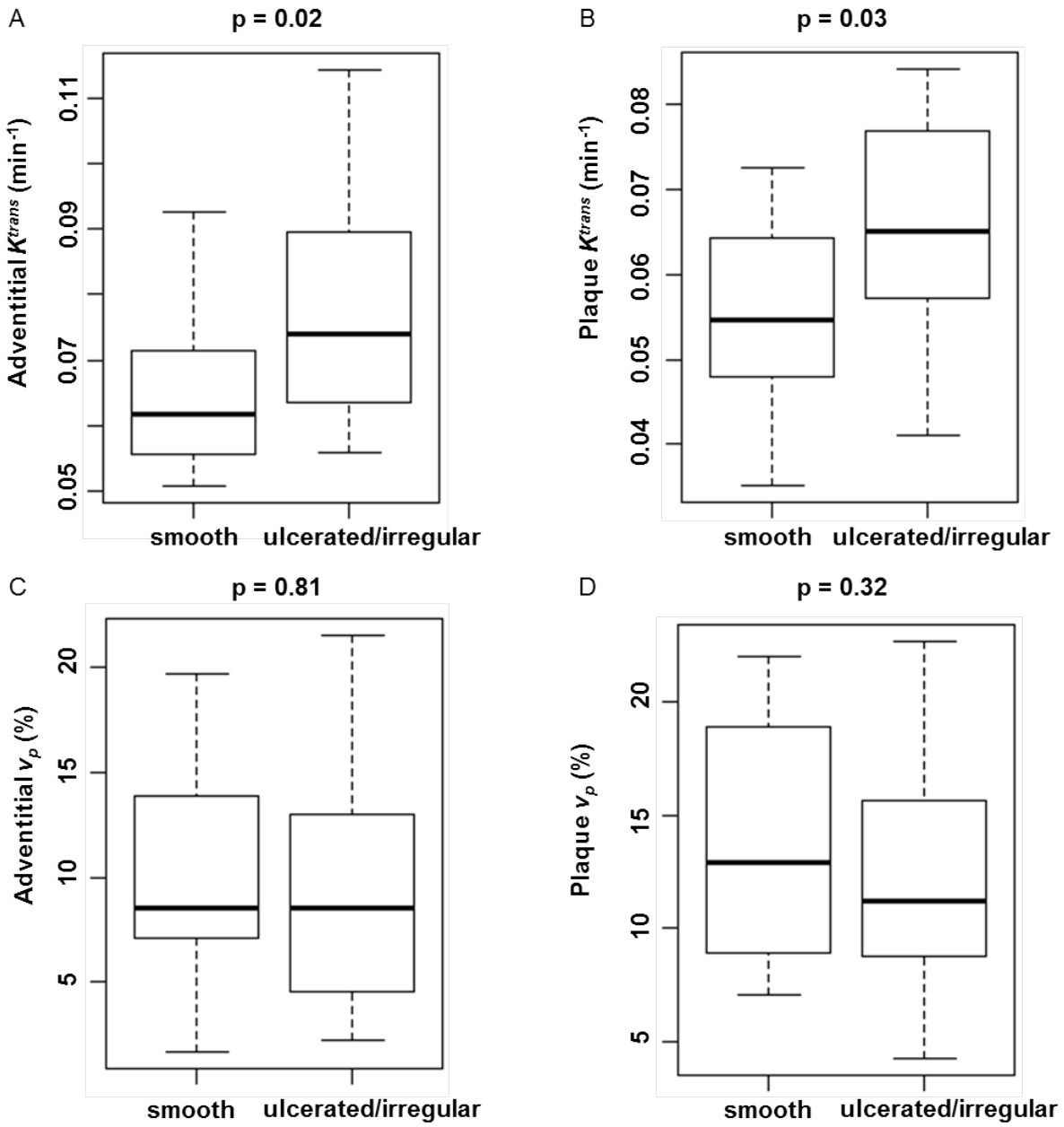

Figure 3.5 (A) and (B) show statistically significant differences in the distributions of K^{trans} for smooth plaques versus ulcerated plaques for adventitial and plaque K^{trans} respectively. The distributions of v_p in smooth and ulcerated plaques were not significantly different within the adventitia (C) or plaque (D). With permission [117].

IPH was found in eight plaques. Within this group, six arteries had ulcerated plaques and two had smooth plaques. In the 20 plaques without IPH, we noted that smooth plaques were more common (12 had smooth plaques), however, these respective proportions were not significantly different (p = 0.28). Plaques with haemorrhage have higher mean adventitial K^{trans} values compared with plaques with no haemorrhage (0.078 ± 0.019 vs. 0.069 ± 0.015 min^{-1}), however the difference was not significant (p = 0.2).

The agreement for the four measured DCE parameters between the two reviewers was good. The ICC for adventitial K^{trans}, plaque K^{trans}, adventitial v_p and plaque v_p are 0.88, 0.93, 0.81 and 0.71, respectively.

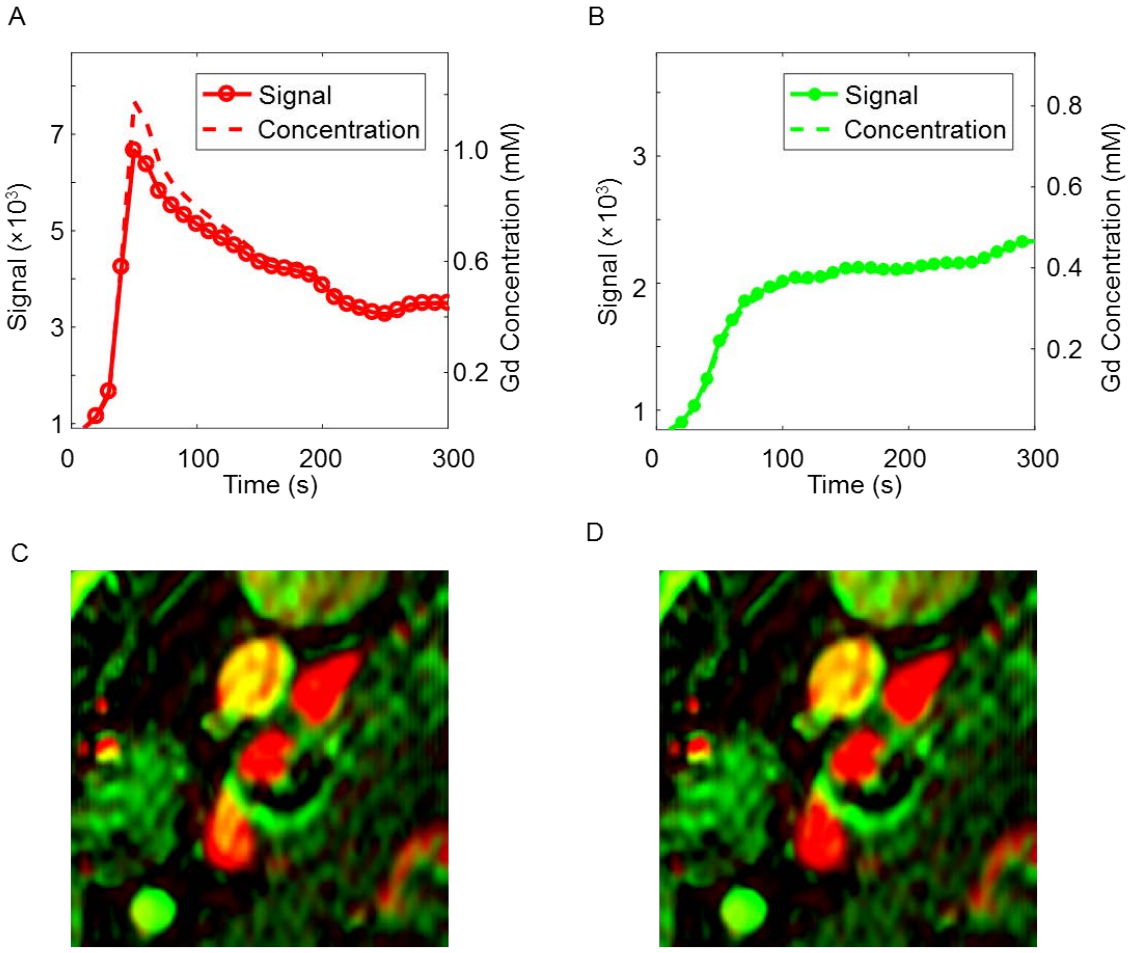

Figure 3.6 (A) and (B) show plots of signal intensity and the derived Gd concentration in the lumen and adventitia respectively. Comparison of the results of VVIs using linear (C) and non-linear (D) assumptions.

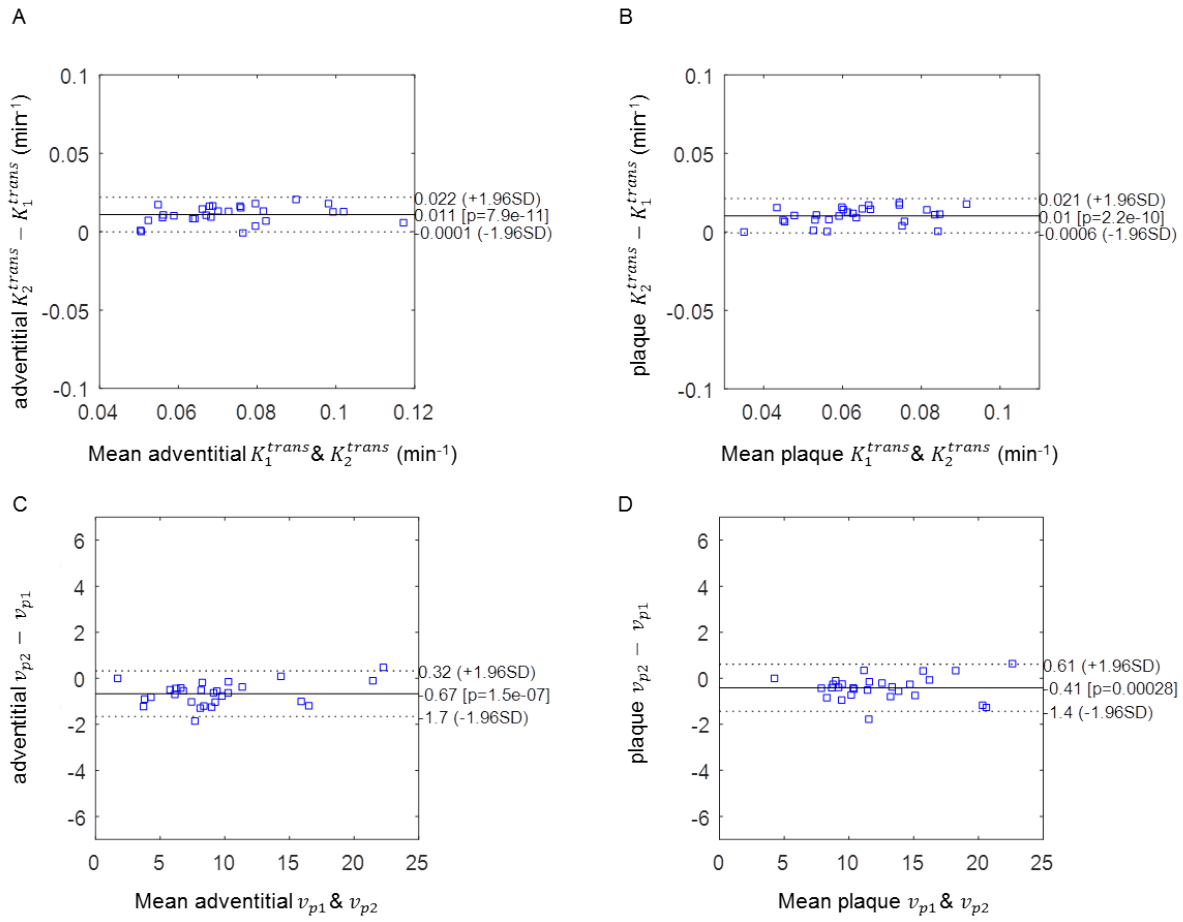

Figure 3.7 Bland-Altman plots of the PK parameters derived after modelling the linear and non-linear relationships between signal intensity and Gd concentration. Note that K_1^{trans} and v_{p1} represent the linear model, and K_2^{trans} and v_{p2} represent the non-linear model. With permission [117].

3.5 Discussion

To the best of our knowledge, this is the first application of a 4D sequence to acquire both high spatial and temporal resolution DCE-MRI and CE-MRA of the carotid artery, allowing for combined morphological and functional assessment of carotid atherosclerosis from a single contrast administration. The results show that adventitial and plaque K^{trans} were higher in ulcerated/irregular plaques compared to smooth plaques. Adventitial K^{trans} and v_p were also positively correlated with the degree of luminal stenosis.

Carotid plaque ulceration, characterised as an intimal defect with the intraplaque component exposed to the lumen [29], can form emboli and thrombosis leading to ischemic neurologic symptoms. Sitzer et al. showed plaque ulceration and lumen thrombus is the main sources of cerebral microemboli [29]. Multiple studies have also shown that plaque ulceration is

associated with cerebral infarcts, TIA and amaurosis fugax [30, 32]. In this study, plaque enhancement could be observed in both smooth and ulcerated plaques and the derived VVI showed significant differences in PK parameters between both of these plaque types. The results demonstrate that ulcerated plaques are more prevalent to neovascularization and possibly inflammation. Plaque ulceration or fibrous cap discontinuity may induce more inflammatory cell infiltration into the plaque, which in turn further weakens the fibrous cap and eventually causes the plaque to rupture. This suggests quantitative analysis of DCE-MRI could provide similar information compared with conventional contrast-enhanced morphological images in identifying lesions at higher risk.

While only adventitial K^{trans} and v_p are correlated with luminal stenosis, no significant correlation was observed between whole plaque PK values and the stenosis. This might be due to a lower sensitivity as a result of averaging PK parameters across the whole plaque region. While various plaque components such as IPH, lipid core and fibrous tissue have different PK values [146], simple averaging of PK parameters across the plaque region may be insufficient for quantitative analysis and risk stratification. A positive correlation between luminal stenosis and adventitial K^{trans} and v_p was observed in this study, indicating a relationship between plaque growth and adventitial neovascularization. These microvessels within the atherosclerotic lesion have shown a close association with inflammatory cells [147] which indicate that these could serve as a pathway for the macrophage entry into the plaque that leads to chronic inflammation hence promoting plaque development.

The presence of IPH has also been found to be associated with increased adventitial K^{trans} [148]. In our study, plaques with IPH had higher adventitial K^{trans}, however the difference was not significant. The reason for this may be due to lack of statistical power, as only a small number of plaques (eight) contained IPH. Although the exact etiology of the IPH is still unclear it is suggested that most likely the rupture of fragile and leaky neovessels that vascularize the developed plaque leads to IPH [149]. The histopathological evidence also supports the relationship of IPH to the presence of neovessels [150]. The relationship between PK parameters and surface morphology also applies to the plaques without IPH, indicating ulceration and a high degree of stenosis were two other factors, apart from IPH, which could present with increased plaque neovascularization and inflammation.

The use of multi-contrast MRI allows for detailed analysis of plaque composition and vulnerability assessment, which could provide more insight than simple luminal stenosis measurements [151]. This study demonstrates that a combined 4D DCE-MRI/MRA acquisition in combination with multi-contrast 3D sequences can aid in the identification of

high-risk plaque features. Our study also demonstrates that these features can be obtained in a clinically acceptable scan time of approximately 30 mins.

There are several limitations in this study. Firstly, no histological validation was performed on the plaques. However the correlation between DCE-MRI and neovascularization as well as inflammation has been demonstrated in previous studies [119, 135, 136], and CE-MRA is considered reliable for observing plaque surface morphology [79, 131]. The second limitation is that only a small patient cohort was included in this study. Finally, the view-ordering sequence used in this study could smooth the temporal information, especially during the injection period. However, this is thought not to be a large effect and other studies have used similar analysis for various applications, including breast [152, 153], prostate [154] and in an animal model [155].

3.6 Conclusion

This study investigated the relationship between PK modelling with carotid plaque surface morphology by simultaneously acquiring 4D DCE-MRI and CE-MRA. Adventitial and plaque K^{trans} from the DCE-MRI analysis is significantly higher in ulcerated plaques than smooth ones. Also, adventitial K^{trans} and v_p are correlated with luminal stenosis.

The obtained results prove the specific hypotheses in this chapter that *[Hypothesis 1]* plaque functional characteristics and surface morphology can be evaluated using a high temporal and spatial resolution 4D contrast-enhanced MRI/MRA sequence and *[Hypothesis 2]* the pharmacokinetic parameters are different between ulcerated and smooth plaques.

Chapter 4 A comparison of black-blood T_2 mapping sequences for carotid vessel wall imaging at 3 T: an assessment of accuracy and repeatability

This chapter documents experiments to test the accuracy and repeatability of four different black-blood T_2 mapping sequences which were developed specifically for carotid vessel wall imaging. The sequences were evaluated and optimised in a phantom and 17 volunteers. T_2 measurement accuracy, repeatability, and image sharpness were compared. This chapter investigates the following hypotheses:

> *[Hypothesis 3]* the in-vivo accuracy and repeatability of the black-blood carotid vessel wall T_2 measurement are dependent on the choice of the sequence.
>
> *[Hypothesis 4]* 3D sequences achieve higher $SNR_{efficiency}$ in the magnitude images than the 2D sequences.

Aspects of this work have been presented at ISMRM 25th Annual meeting, 2017. No.2786.

4.1 Introduction

Quantitative MRI allows direct measurement of the MR properties of human tissue. Among the quantitative values, T_2 has been reported to be statistically different in major plaque components [102]. Quantitative T_2 mapping has the potential to assist plaque component segmentation and plaque type classification [156].

Several pulse sequences could be used to quantify the T_2 values within the plaque, including the 2D multi-echo spin echo (MESE) [157, 158], 2D multi-echo fast-spin-echo (MEFSE), 3D fast-spin-echo (FSE) [159], and 3D fast spoiled gradient echo (FSPGR) [160]. Different black-blood techniques could be used in combination with the acquisition: double inversion-recovery (DIR) [156], motion-sensitized driven-equilibrium (MSDE) [113, 159], and delay alternating with nutation for tailored excitation (DANTE) [89].

The in-vivo quantitative T_2 measurement could be influenced by many factors, including B_0 and B_1 field inhomogeneity, stimulated echoes, T_1 effects, choice of fitting methods [161], and the black-blood preparation regime. Some of these factors have been discussed in previous studies [156, 161-163]. With the emergence of T_2 mapping sequences for vessel wall imaging, the choice of the sequence is another factor that could influence T_2 measurement accuracy. However, there is a sparsity of comparative studies comparing in-vivo T_2 mapping sequences.

The purpose of this work is to compare four different black-blood prepared quantitative T_2 mapping sequences. Initial investigations were performed by consideration of the signal intensity evolution using Bloch simulations. Phantom experiments were then performed comparing each respective method to the gold standard sequence. In-vivo volunteer experiments were then performed to enable comparison of vessel wall relaxivity values, repeatability, and image quality.

4.2 Materials and Methods

4.2.1 Sequences

Four black-blood T_2 mapping sequences were developed and tested, including 1) DIR prepared 2D MESE; 2) DIR prepared 2D MEFSE; 3) iMSDE prepared 3D FSE with variable flip angle; and 4) iMSDE prepared 3D FSPGR. The third and fourth sequences were developed by the author.

In the 3D FSE/FSPGR sequences, different echo times were achieved by varying the RF and gradient pulse intervals in the iMSDE preparation, while keeping the readout the same for different echoes. To achieve adequate blood suppression, the first moment of iMSDE preparation of the first echo in 3D FSE and FSPGR was 838.0 and 6666.7 $mTms^2/m$, respectively. The applied first moments were a result of empirical observations to achieve appropriate blood suppression for each sequence. The 3D FSE flip angle train was designed accordingly using mean vessel wall MR properties, from the literature (T_1 = 1000 ms, T_2 = 50 ms) [102]. A segmented multi-shot radial fan-beam trajectory was used for 3D acquisitions. The FSE based 2D and 3D sequences acquired the different echoes using an interleaved acquisition order, while the 3D FSPGR sequence acquired the echoes sequentially. Examples of these two acquisition methods are shown in Figure 4.1.

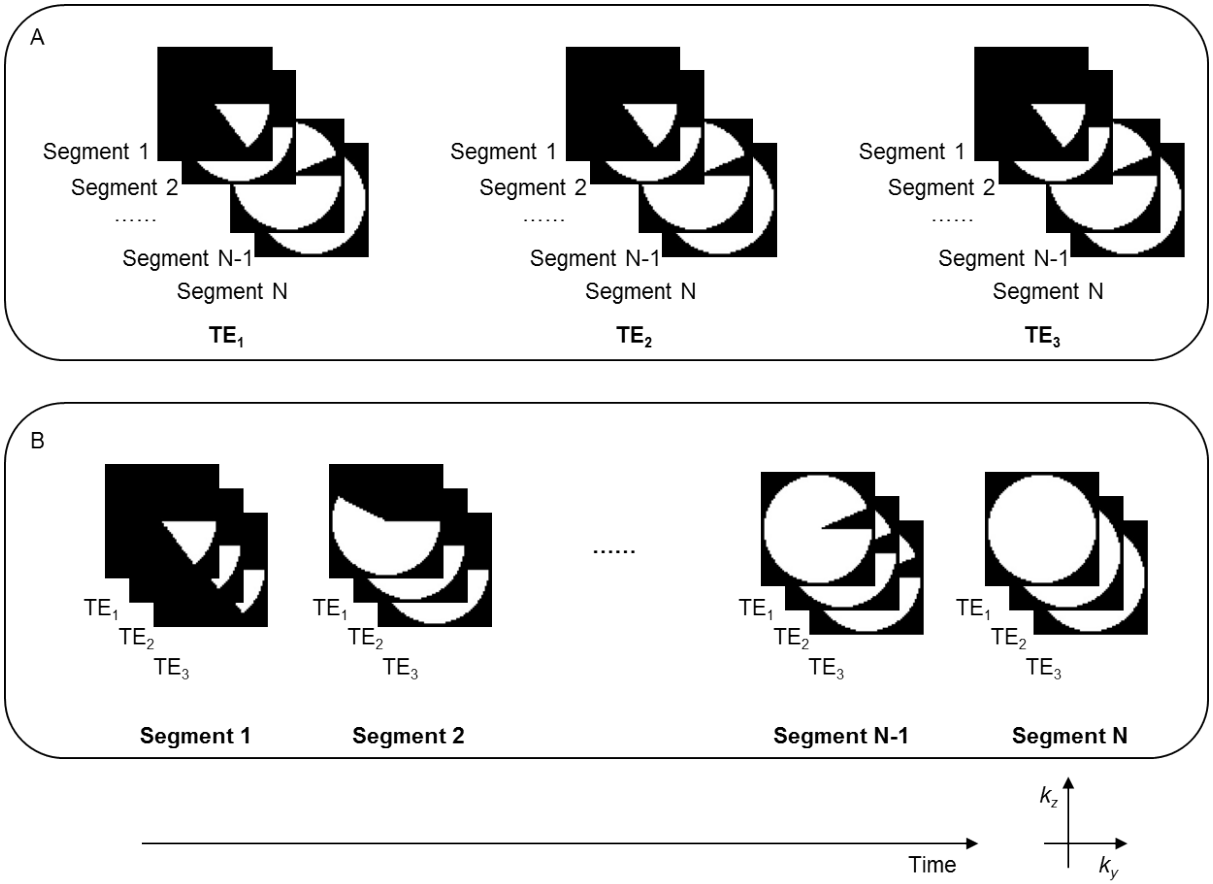

Figure 4.1 Sequential (A) and interleaved (B) multi-echo 3D acquisitions using a segmented multi-shot radial fan-beam trajectory.

In the FSPGR sequence, 200 dummy pulses were used at the beginning of the sequence to allow the magnetisation to achieve a steady state and 50 dummy pulses were used after the acquisition to allow the magnetisation recovery to reach an equilibrium state [160]. A delay time of 400 ms was used at the end of each segment for higher SNR [144, 164]. The time duration for each segment was about 1200 ms. Fat saturation in the 3D FSE sequence was achieved by using an Adiabatic SPectral Inversion Recovery (ASPIR) pulse, the other three sequences used a standard chemical shift selective saturation pulse. Other imaging parameters are listed in Table 4.1.

Bloch simulations were performed to evaluate the vessel wall signal evolutions for the four sequences, using T_1 = 1000 ms and T_2 = 50 ms [102]. The Bloch simulation code was available online mentioned in Chapter 2. The author performed the DIR or iMSDE prepared FSE and FSPGR simulation based on the spin-echo and gradient-echo demonstration available from the mentioned webpage. Initial tests were carried out to compare the simulation result with theoretical calculation to ensure the simulation results were correct.

Sequence	2D MESE (reference)	2D MESE	2D MEFSE	3D FSE	3D FSPGR
Blood suppression	-	DIR	DIR	iMSDE	iMSDE
Num. of echoes	8	8	8	3	3
Acquisition order	interleaved	interleaved	interleaved	interleaved	sequential
Echo time (ms)	12.4 to 99.1 with 12.4 interval	12.9 to 103.2 with 12.9 interval	6.7 to 193.7 with 26.7 interval	25.8/55.8/85.8 (include prep)	23.2/43.2/63.2 (include prep)
Num. of Averages	0.5	0.5	1	1	1
Repetition time (ms)	2000	Two R-R intervals	Two R-R intervals	2000	7.1
ETL/VPS	8	8	32	40	50
Bandwidth (kHz)	31.3	31.3	31.3	31.3	31.3
In-plane FOV (mm×mm)	140×140	140×140	140×140	140×140	140×140
Slice thickness (mm)	1.4	1.4	1.4	1.4	1.4
Matrix	224×224	224×224	224×224	224×224×30	224×224×30
Acquisition time	4:10	~ 3:03	~ 1:27	8:55	7:54

Table 4.1 Scanning parameters of the sequences. VPS: views per segment;

4.2.2 Phantom and subjects

The four sequences were tested using the Eurospin Test Object gel phantoms (TO5, Diagnostic Sonar, Livingston, Scotland) with known T_2 values ranging from 52 to 136 ms at 19 ºC. A 2D MESE sequence without blood suppression was used as the gold standard.

Seventeen healthy volunteers (eleven men, mean age 33, range: 23-44 years) were recruited into this study. The volunteer experiments were conducted under a research ethics agreement and all volunteers gave informed written consent (R&D number: A091374). For the 2D sequences, a single axial slice 3 mm below the carotid bifurcation was chosen. For the 3D sequences, an axial slab was centred at the bifurcation. The slice thickness for all four sequences was set to 1.4 mm. To assess the repeatability, eight volunteers were scanned for the second time. The average interval between the two scans was 43 days (range 28 to 69 days). All the phantom and volunteer scans were performed on a 3 T system (MR750, GE Healthcare, Waukesha, WI), using a four-channel phased-array neck coil (PACC, MachNet, Roden, The Netherlands).

4.2.3 Image analysis and T_2 quantification

Contours of the carotid vessel wall and lumen at matched slice locations across all four sequences were manually drawn by a single observer, who had three years of carotid imaging experience, using a DICOM viewer (OsiriX 5.5.2, Pixmeo, Geneva, Switzerland).

T_2 fitting was performed by considering the noise floor in the power images using the algorithm described by Miller et al [112], which has previously been demonstrated to yield accurate T_2 values [159]:

$$I_c(TE)^2 = I_s(TE)^2 - I_n(TE)^2 \tag{4.1}$$

where $I_s(TE)$ and $I_n(TE)$ are the signal and background noise intensity, and $I_c(TE)$ is the corrected signal intensity at each echo. The T_2 map was then generated on a voxelwise basis by fitting the following equation to the images with different TEs using the Levenberg-Marquardt nonlinear least-squares algorithm:

$$I_c(TE)^2 = {I_0}^2 e^{-2TE/T_2} \tag{4.2}$$

where ${I_0}^2$ is the estimated power signal at TE = 0.

In the 2D MESE/MEFSE sequences, the imperfect 180° refocusing pulses cause stimulated echoes in the second and later echo images. Therefore the first echo image without stimulated echo contamination were discarded for the T_2 fitting [156]. In the 3D FSPGR sequence sequentially acquired images were first co-registered to the first echo before performing the fitting, using a standard intensity-based registration function (*imregister* from Matlab's Image Processing Toolbox, MathWorks, Natick, MA, USA).

The mean and standard deviation of the measured T_2 values, SNR, $SNR_{efficiency}$ from the first analysed echo, and the coefficient of variance (CoV) in the carotid vessel wall from all four sequences were compared. The SNR was defined as the mean wall signal divided by the standard deviation of the background noise, and considered the four-channel coil correction [165, 166]

$$SNR = 0.659 \times \frac{mean\ wall\ signal}{standard\ deviation\ of\ noise} \tag{4.3}$$

The $SNR_{efficiency}$ was defined as:

$$SNR_{efficiency} = \frac{SNR}{\sqrt{acquisition\ time\ per\ echo}} \tag{4.4}$$

The CoV was defined as follows within each of the vessels:

$$CoV = \frac{standard\ deviation\ of\ wall\ signal}{mean\ wall\ signal} \tag{4.5}$$

4.2.4 Statistical analysis

For the phantom scans, the concordance correlation coefficient (CCC) and Bland-Altman summary statistics were used to compare the four sequences against the gold standard method. For the volunteer scans, paired two-tailed Student's t-tests were used to compare the results for parametric distributions and the Wilcoxon signed-rank test were used for non-parametric distributions. The intraclass correlation coefficient (ICC) was used to evaluate the agreement between the two repeated scans. Statistical significance was defined as a p-value < 0.05. The statistical analysis was performed using R version 3.2.2 (R Core Team 2015, Vienna, Austria) [167].

4.3 Results

The Bloch simulation results are shown in Figure 4.2. In the phantom scans, the correlations for 2D MESE, 2D MEFSE, 3D FSE and FSPGR were all very high: r = 0.999, 0.999, 0.995 and 0.985, respectively, compared with the gold standard sequence (MESE without blood suppression). The results of the Bland-Altman analysis for the four sequences comparing to the reference sequence was shown in Table 4.2.

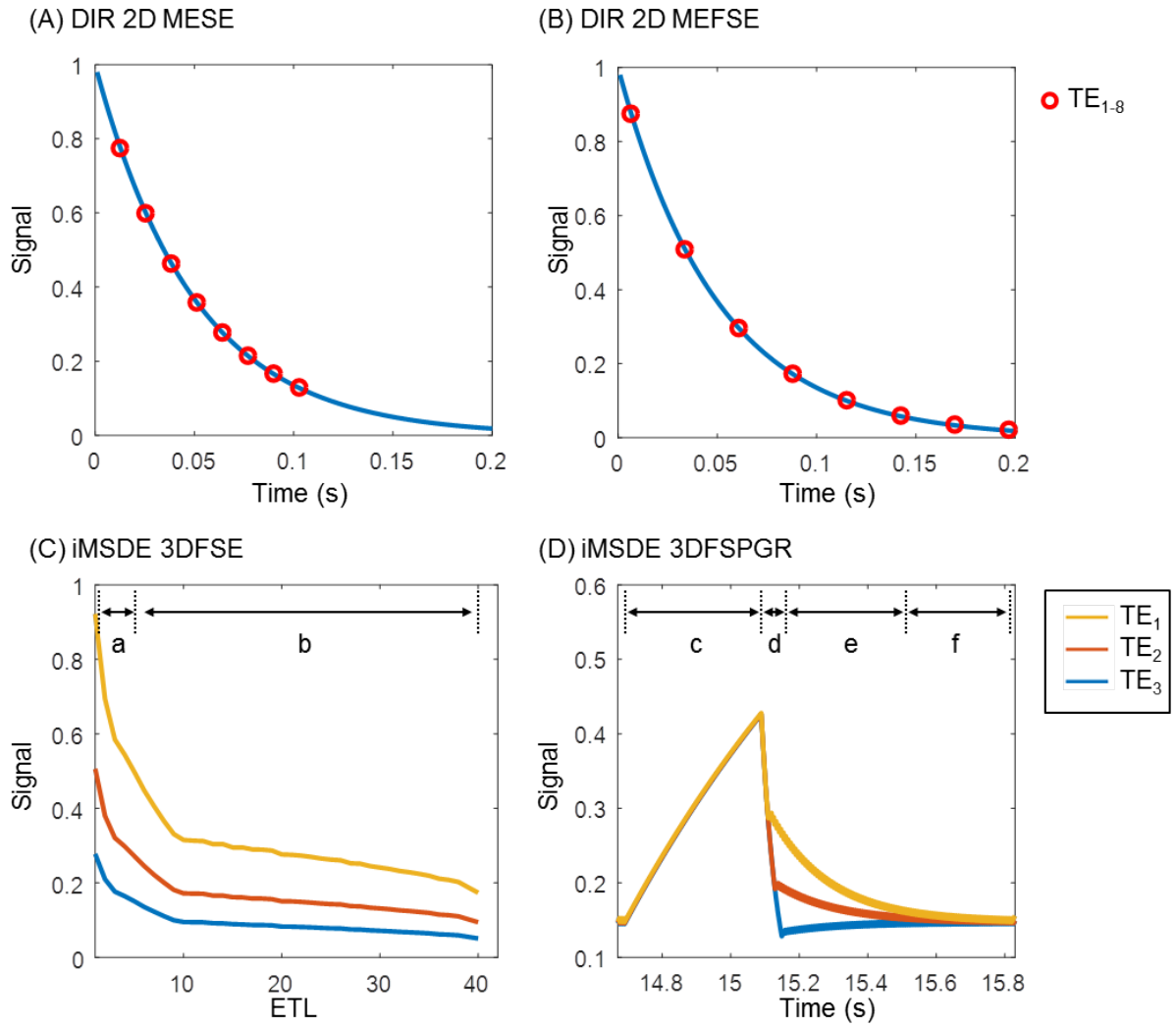

Figure 4.2 Bloch simulations of signal evolution within one segment in four sequences. (A) DIR 2D MESE, (B) DIR 2D MEFSE, (C) iMSDE 3D FSE, the FSE readouts are plotted out. The first four echoes (a) are discarded to allow the magnetisation to reach the equilibrium state before the acquisition (b). (D) iMSDE 3D FSPGR. Subsections: c: delay time; d: iMSDE and fat sat pulse; e: data acquisition; f: dummy pulses. T_1 = 1000 ms and T_2 = 50 ms are used for the simulations. Detailed descriptions are provided in the method section. Other parameters are listed in Table 4.1.

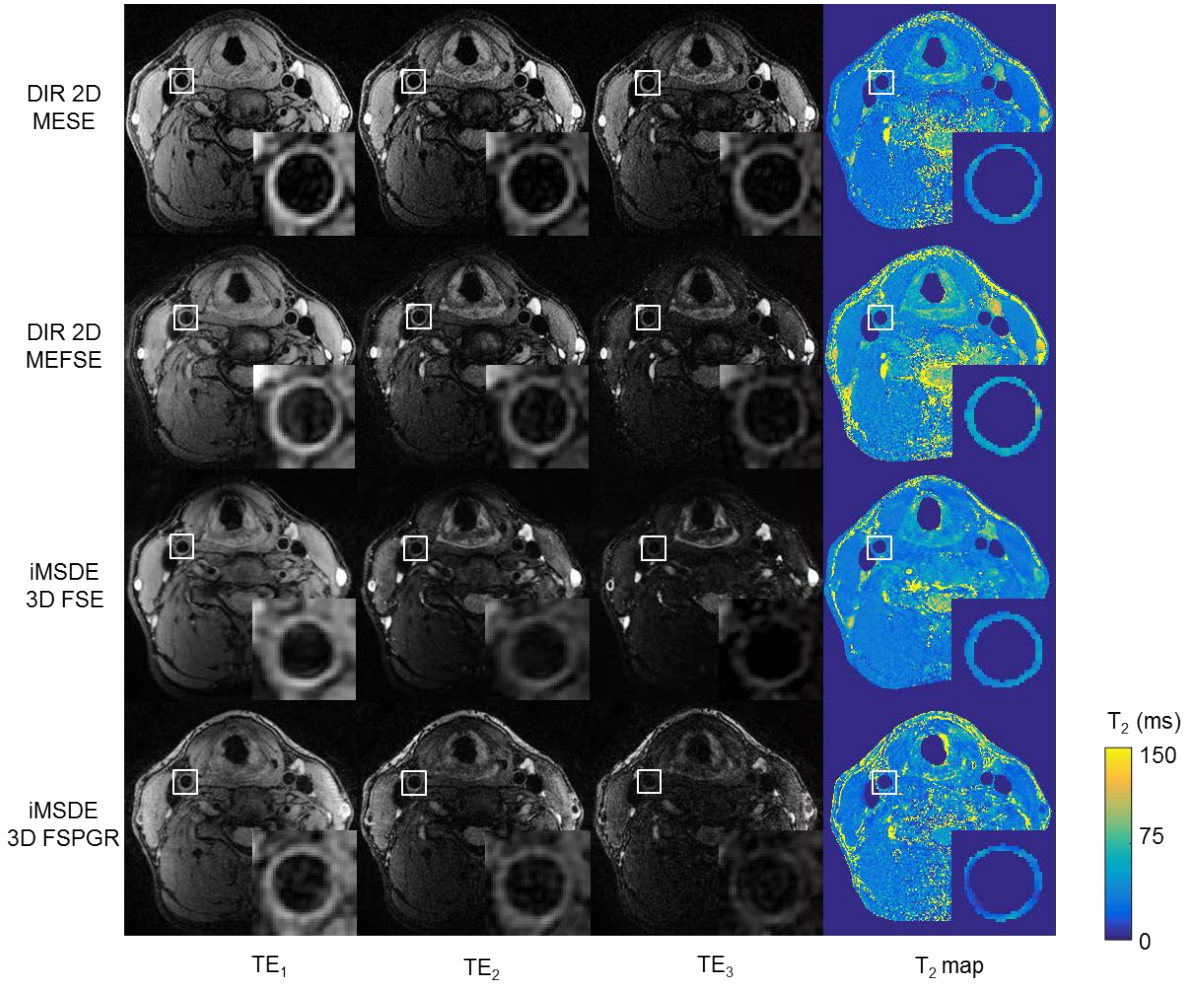

Figure 4.3 An example of volunteer images and T_2 maps using the four different sequences. $TE_{1,2,3}$ are the first, second and third echoes used within the analysis.

Sequence	Bias (ms)	95% CI
DIR 2D MESE	-5.9	-11.0 to -1.0
DIR 2D MEFSE	7.7	4.7 to 11
iMSDE 3D FSE	4.3	-1.5 to 10.0
iMSDE 3D FSPGR	2.9	-13.0 to 19.0

Table 4.2 Bland-Altman analysis of the four sequences compared to the reference sequence (2D MESE without black-blood preparation).

	DIR 2D MESE	DIR 2D MEFSE	iMSDE 3D FSE	iMSDE 3D FSPGR
T_2 ± SD (ms)	43.5 ± 8.2	52.9 ± 8.6	36.0 ± 6.5	41.1 ± 9.3
SNR ± SD	11.1 ± 2.6	10.8 ± 3.9	25.0 ± 8.8	13.8 ± 7.4
$SNR_{efficiency}$ ± SD ($min^{-1/2}$)	6.3 ± 1.5	9.0 ± 3.3	14.6 ± 5.1	8.6 ± 4.6
CoV (Median with IQR, %)	40 (32-45)	29 (24-44)	35 (32-42)	66 (54-75)

Table 4.3 Mean and SD of T_2 measurement, SNR and $SNR_{efficiency}$ and CoV derived from four sequences in the volunteer scans. IQR: Interquartile range;

All the volunteers completed the MRI studies. In total 34 carotid arteries were analysed. Example images from a volunteer and the resultant T_2 maps derived using the four black-blood sequences are shown in Figure 4.3. The mean T_2, SNR, $SNR_{efficiency}$, and CoV of the volunteer vessel walls are summarised in Table 4.3. The T_2 measurements from 2D MESE and 3D FSE/FSPGR showed no significant difference (43.5 ± 8.2, 36.0 ± 6.5 and 41.1 ± 9.3 ms, respectively, $p > 0.05$). While the 2D MEFSE yielded significantly higher T_2 values than the other three sequences (52.9 ± 8.6 ms, $p < 0.05$). The highest SNR was found in the 3D FSE sequence (25.0 ± 8.8, $p < 0.05$), while the 2D MEFSE had the lowest SNR (10.8 ± 3.9).

The 3D FSE also had the highest $SNR_{efficiency}$ (14.6 ± 5.1 $min^{-1/2}$, $p < 0.05$), while the other three sequences had similar $SNR_{efficiency}$ ($p > 0.05$). The CoV for the 2D MESE, 2D MEFSE and 3D FSE was similar [median and interquartile range: 40% (32–45%), 29% (24–44%) and 35% (32–42%), respectively, $p > 0.05$], but they were significantly lower compared to 3D FSPGR sequence [66% (54–75%), $p < 0.01$]. The ICCs with 95% CI for the repeated scans of the four sequences were: 2D MESE: 0.96 (0.88-0.99); 2D MEFSE: 0.82 (0.54-0.93); 3D FSE: 0.86 (0.63-0.95); 3D FSPGR: 0.65 (0.20-0.88).

4.4 Discussion

This study, for the first time, compared the accuracy of different black-blood T_2 mapping sequences in the carotid vessel wall. All four sequences demonstrated accurate T_2 quantifications in the phantom scans; however, it is noted that there are significant differences in the in-vivo results as well as differences in image quality. Though all the in-vivo T_2 measurements are comparable with previous studies [156, 159, 160].

The choice of black-blood technique is an important factor for accurate T_2 measurement in-vivo. As the irregular plaque surface and carotid bifurcation could form complex flow patterns, poor suppression of the blood flow could result in errors in vessel wall T_2 quantification, due to partial volume. In these cases, the 3D techniques showed better blood suppression compared to the 2D methods such as DIR [144, 165]. Another consideration for the black-blood preparation pulse is whether it is sensitive to B_1^+ field non-uniformity, especially on 3 T. It has been shown that the conventional MSDE method, compared to DIR or DANTE, is more sensitive to B_1^+ field non-uniformity [144]. This could result in signal variation in the images leading to inaccurate T_2 measurement. Our results from the iMSDE prepared 3D FSPGR sequence which utilised a higher first order moment of 6666.7 $mTms^2/m$ support this finding (Figure 4.3 and CoV in Table 4.3). Careful shimming during the scan and further optimisation of the MSDE sequence, such as i^2MSDE [168] or the use of sinusoidal gradients [165], could help to reduce these effects. The changing preparation time used in the iMSDE could potentially result in a magnetisation transfer (MT) effect [87, 169]. However, the iMSDE prepared 3D sequences demonstrated accurate T_2 measurements in the phantom, and comparable T_2 measurements in the volunteers with the 2D DIR MESE sequence, indicating that MT is not influencing the T_2 quantification.

The acquisition method is another consideration for vessel wall imaging. In the current study, both FSE and GRE based acquisitions were evaluated. The results showed that the 3D FSE sequence achieves a higher SNR, $SNR_{efficiency}$ and lower T_2 CoV compared to the 3D FSPGR sequence. This could be explained by the following reasons. First, FSE based readouts utilise refocusing pulses which are less sensitive to B_1^+ field non-uniformity and resonant frequency errors than GRE based readouts. Second, during the FSE readout, the movement of blood spins could induce intra-voxel dephasing which results in intrinsically black-blood effects, as previously reported in other studies [170, 171]. Consequently, the FSE based sequences can use less or no black-blood preparation [172] compared to the strong blood suppression used in GRE readout, and are therefore less influenced by black-blood preparation as shown in our study.

Both 2D and 3D methods were included in this study. The use of 3D acquisitions has several advantages over 2D methods. Firstly, it allows greater longitudinal coverage. This could help with plaques located in the proximal common carotid artery or distal internal carotid artery [173] which might be missed by the more limited coverage using 2D acquisitions. Secondly, it could allow thinner slice thickness which results in less partial volume effects and potentially more accurate plaque morphological measurements [174]. Thirdly, the 3D

sequences have higher SNR as our results showed. However, this also leads to one of the disadvantages of the 3D methods. Since the signals are from the entire imaging volume, any movement during the acquisition could influence the entire dataset, so the 3D methods are potentially more prone to motion artefact. However, the volunteer images in this study showed no obvious motion artefact.

For the 2D sequences, the MEFSE demonstrated significantly higher T_2 values than MESE in volunteers. Similar results were reported in previous studies [162, 163]. Imperfections in the 180º refocusing pulses cause stimulated echoes which lead to higher signal intensities in later echoes [161, 175]. This phenomenon is more obvious in 2D FSE sequences with longer echo train lengths [163].

The T_2 calculation based on Miller's method [112] was used in this study. There are other curve fitting methods used in the literature, such as two-parameter fitting without noise correction [156, 158] or three-parameter fitting method [176]. Miller's power correction was applied in this study as the 3D sequences only acquired three echoes. This approach prevented the noise floor contributing to errors in T_2 calculations [177].

There are two main limitations in this study. Firstly, the three FSE based sequences acquired multiple echoes in an interleaved manner, while the FSPGR sequence acquired the echoes sequentially, which was the same method used in a previous study [160]. Hence image registration was needed for the 3D FSPGR sequence which may potentially introduce further errors into the T_2 analysis. However, in this study, no obvious motion was observed in the volunteer data, but it may be difficult for patients to keep still given such a long acquisition time. Thus, an interleaved acquisition may be preferable, further time reduction strategies such as parallel imaging [178] and compressed sensing [159, 164, 179], should be investigated. Secondly, these methods were only evaluated in normal volunteers.

4.5 Conclusion

Four different black-blood T_2 mapping sequences were developed and validated through Bloch simulation and phantom experiments as well as in a cohort of healthy volunteers. Although the phantom scans showed accurate T_2 measurement, the in-vivo measurements of the four sequences were significantly different. Therefore, a careful choice of T_2 mapping sequence is warranted for carotid vessel wall imaging.

The results prove the specific hypotheses investigated in this chapter that *[Hypothesis 3]* the in-vivo accuracy and repeatability of the black-blood carotid vessel wall T_2 measurement is different when using different sequences and *[Hypothesis 4]* 3D sequences achieves higher $SNR_{efficiency}$ in the magnitude images than the 2D sequences.

Chapter 5 Three-dimensional black-blood T_2 mapping with compressed sensing and data-driven parallel imaging in the carotid artery

In Chapter 4, it was shown that the iMSDE prepared 3D FSE sequence achieved the highest SNR, $SNR_{efficiency}$ and relative high repeatability. In this chapter, this sequence was combined with compressed sensing (CS) and parallel imaging (PI) to reduce the acquisition time. The accelerated sequence was optimised in a phantom and 12 volunteers, and then applied to a cohort of eight patients. The main hypotheses for this chapter are that

> *[Hypothesis 5]* the CS and PI accelerated 3D T_2 mapping sequence can achieve accurate T_2 measurement with good reproducibility.
>
> *[Hypothesis 6]* the CS and PI accelerated 3D T_2 mapping sequence is clinically feasible and can measure different T_2 values between plaque components.

Aspects of this work have been published in Magnetic Resonance Imaging 2017, 37:62-69 [180].

5.1 Background

5.1.1 Compressed sensing MRI

Compressed sensing (CS) has been introduced to MRI to improve the efficiency of the image acquisition. The technique of MRI obeys three key requirements for successful CS application [181]: (1) MRI is compressible (has a sparse representation) in a known transform domain. (2) The artefact due to undersampling is incoherence. (3) A nonlinear reconstruction can be used to enforce both sparsity of image representation and consistency of the acquired data. To understand the CS in the MRI images, several backgrounds needs to be introduced.

Sparsity

A sparsity of a vector or image means that most of the coefficients are exact zeros. For example, in Nyquist sampling, the acquired number of *k*-space samples equals to the number of image pixels. However the compressibility of sparseness means the number of

essential *k*-space points can be fewer than the number of image voxels. The essential *k*-space points must contain enough information to reconstruct the image with adequate diagnostic quality.

Incoherent Sampling

Uniform undersampling and zero-filled reconstruction are completely coherent as the artefact is simply the replication of original image. Non-uniform undersampling on the other hand, could spread the artefact throughout the image, resulting in the incoherent artefact, as shown in Figure 5.1.

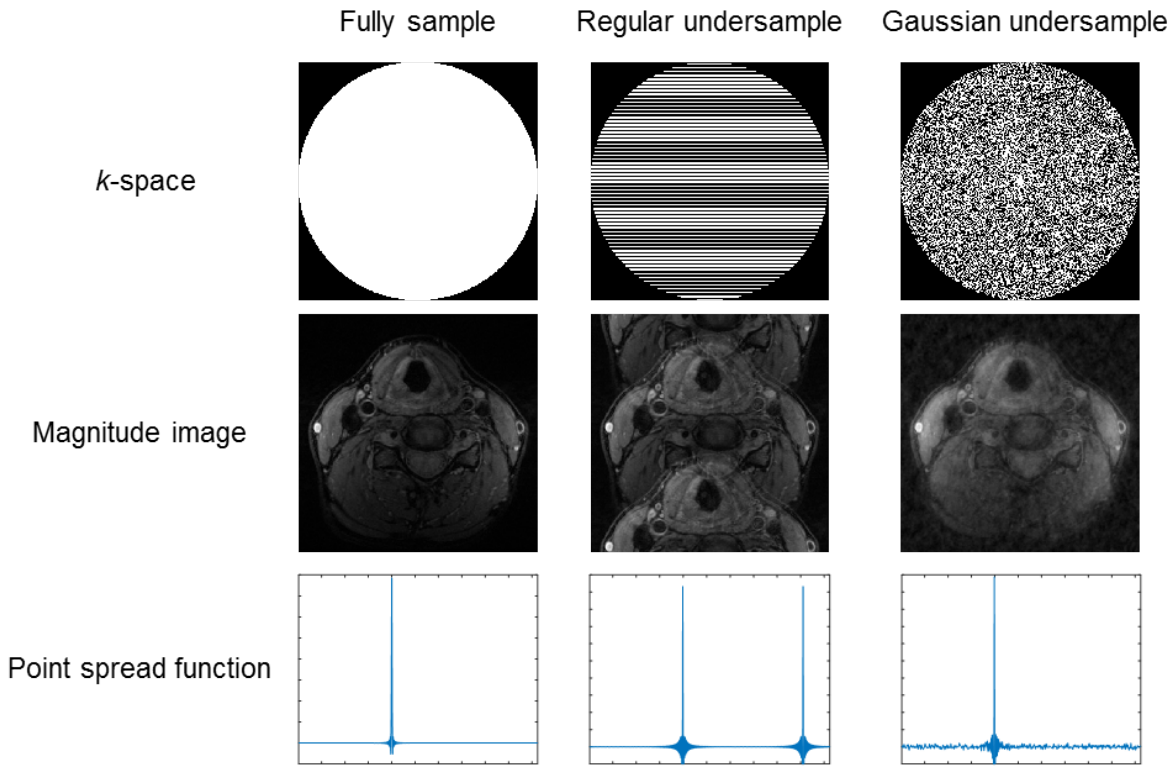

Figure 5.1 An example showing the difference between fully sampled, Nyquist and Gaussian undersample. The corresponding *k*-space, magnitude image and point spread function are shown. Nyquist undersample results in coherent artefact and repeated point spread function. The Gaussian random undersample results in incoherent artefact and similar point spread function with fully sampled example.

Figure 5.2 shows the diagram of how the incoherent artefact can be removed by the CS reconstruction.

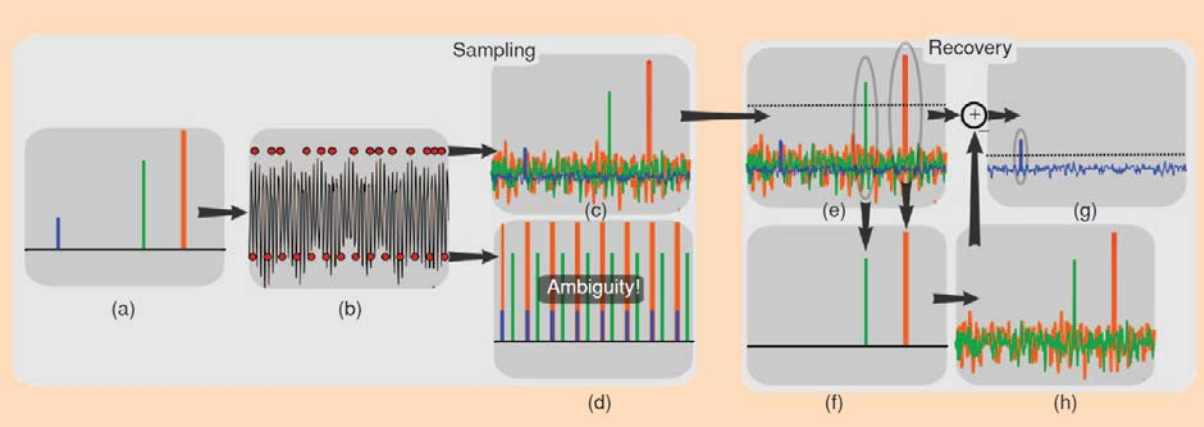

Figure 5.2 An example of CS reconstruction from undersampled data. (a) A sparse signal is under sampled in its 1-D *k*-space domain by a factor of eight (b). (c) Pseudo-random undersampling causes the energy leaks away from each nonzero signal, and results in an incoherent interference and other reconstructed signal (not noise). (d) Equispaced under sampling with reconstruction by zero-filling results in coherent aliasing, the original signal and artefact cannot be distinguished. (e-f) A threshold based method firstly recovers the strong component, to calculate their interference (h). The calculated interference was subtracted by the original signal to reduce the total interference level, allowing the threshold for weaker, previously submerged components. By iteratively repeating (e)–(g), the rest of the component can be recovered. With permission [181].

Reconstruction

The CS reconstruction used in this work includes an L1-norm constraint to recovery the missing information from the undersampled data:

$$\hat{m} = minimize\{\|\Psi m\|_1\}\ such\ that\ F\hat{m} = y \tag{5.1}$$

where m is the complex image, Ψ is a sparsifing transform (such as a nearest neighbor finite difference used in this work), the notion $\|\ \ \|_1$ means the L1 norm, F is the Fourier transform operator and y is the acquired *k*-space data. The general p norm is defined as:

$$\|x\|_p = (\sum_k |x_k|^p)^{1/p} \tag{5.2}$$

In the presence of noise, Equation 5.1 can be written as

$$\hat{m} = minimize\{\|\Psi m\|_1\}\ such\ that\ \|F\hat{m} - y\|_2^2 \leq \epsilon \tag{5.3}$$

Where ϵ is used normally under the level of noise.

Furthermore, Equation 5.3 can be written using a Lagrange multiplier by incorporating the constraint $\|F\hat{m} - y\|_2^2 \leq \epsilon$ to

$$\hat{m} = minimize\{\|Fm - y\|_2^2 + \lambda\|\Psi m\|_1\} \quad (5.4)$$

The CS algorithm runs the following loop to reconstruct the final image:

(a) Start with the zero-filled Fourier transform image
(b) Perform the non-linear conjugate gradient to find the image that reduces the $\|\Psi m\|_1$
(c) Calculate the new k-space data using y = Fm
(d) Replace the measured location in the *k*-space with measured data to form a new y
(e) Find the new image m = F^{-1}y, and repeat step (b) to (e).

Normally, the number of iterations is fixed in the reconstruction pipeline based on prior empirical observations assessing reconstruction time and accuracy. Fifteen iteration loops were used in this work.

5.1.2 Autocalibrating Reconstruction for Cartesian imaging (ARC)

The parallel imaging method used in this work is ARC (Autocalibrating Reconstruction for Cartesian imaging). The *k*-space is undersampled by a certain factor to reduce the acquisition time, except the central region, known as the autocalibration signal (ACS), which is fully sampled. During the reconstruction, the known data from the ACS region is used to calculate the weighting factors for each coil (eg, the carotid coil has four individual channels). Missing *k*-space points are then estimated by considering these global weighting factors as well as the surrounding acquired data (kernel) for the coil. After filling the empty *k*-space points, the magnitude image from the different coil elements is combined using the sum-of-squares reconstruction algorithm.

5.1.3 CS and ARC combination

In this work, CS and ARC are combined in a sequential way with CS as the first step, and ARC as the second step [182], as shown in Figure 5.3. There are several reasons for this:

(a) The CS feature can be implemented more easily with our previous acquisition with parallel imaging reconstruction
(b) This allows easy combinations of different CS and ARC factors in both setup and reconstruction

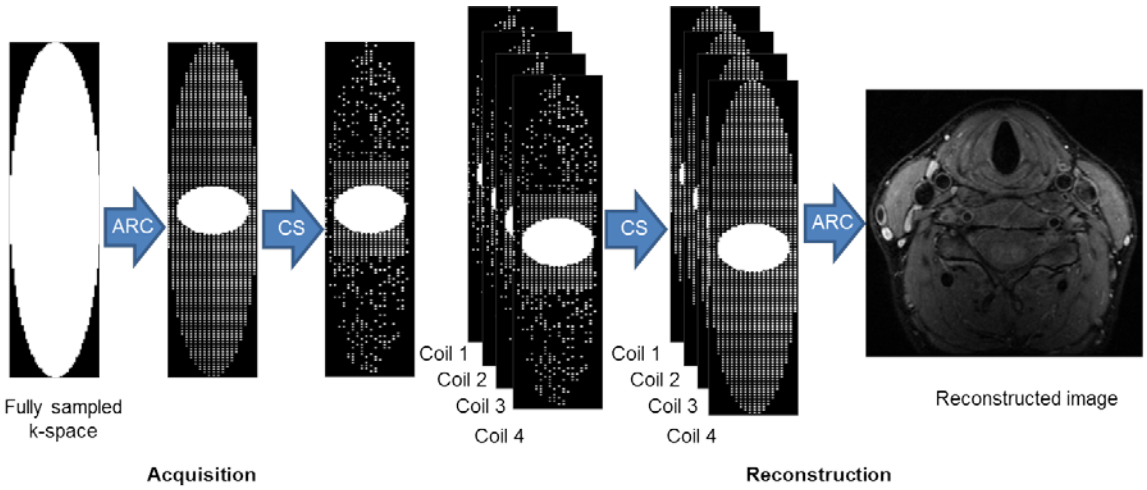

Figure 5.3 CS and ARC are combined in sequential steps to produce the reconstructed image.

5.2 Introduction

This study applies improved motion-sensitized driven-equilibrium (iMSDE) as a preparation pulse to suppress blood flow. Furthermore, the intra-pulse durations within the iMSDE preparation are varied to change the effective echo time (TE) and enable subsequent T_2 quantification. Unlike 2D T_2 mapping sequences, which acquire multiple TEs in one repetition time (TR), 3D T_2 mapping sequences normally repeat the same sequence multiple times with different effective TEs, resulting in long overall scan times. In addition, patient movement during long scanning times cannot be eliminated especially when the images at the different echo times are acquired sequentially. This requires additional image coregistration which may reduce the accuracy of T_2 measurements. The sequence in this study used an interleaved acquisition so that the images at different echo times are intrinsically coregistered.

This study evaluates an iMSDE prepared, black-blood, 3D T_2 mapping sequence with the combination of compressed sensing and data-driven parallel imaging [182]. Phantom studies and healthy volunteer scans were carried out to evaluate the accuracy and repeatability of this sequence. Patients with carotid stenosis >50% were also scanned using this sequence and the T_2 maps were compared with conventional multi-contrast images.

5.3 Materials and Methods

Sequence

An iMSDE preparation scheme, with variable TE, was combined with a 3D fast spin echo (FSE) readout to achieve black-blood T_2 mapping, as shown in Figure 5.4. A variable flip

angle refocusing train was used in the readout [183]. The iMSDE preparation is comprised of two non-selective 90° pulses with two composite 180° pulses between them, together with motion sensitive gradients along the X, Y and Z axes between the pulses [88]. The first-order moment was empirically set to 412 $mTms^2/m$. Fat saturation was achieved by using an Adiabatic SPectral Inversion Recovery (ASPIR) pulse before the FSE readout. A radial view ordering scheme was used to achieve the shortest possible readout TE [183]. The total TE for the sequence is the sum of the iMSDE preparation TE_{iMSDE} and the FSE readout TE_{FSE}. By changing the time interval within the iMSDE preparation (TE_{iMSDE} = 4τ), images with different TEs were achieved. Three different values of TE_{iMSDE} were interleaved in a single acquisition.

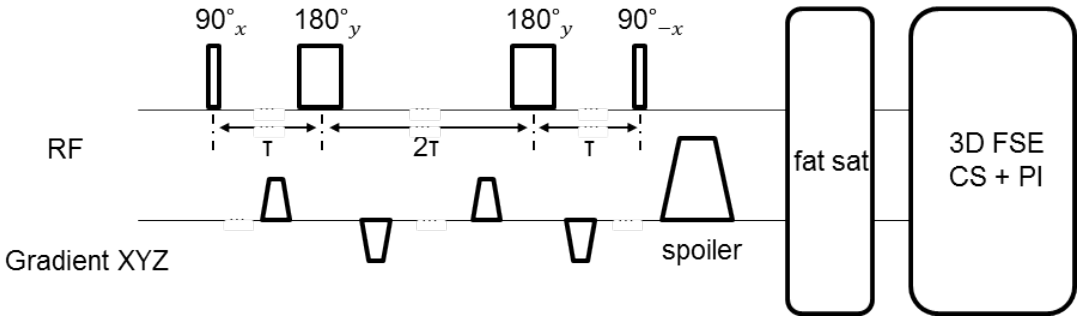

Figure 5.4 3D iMSDE prepared compressed sensing FSE. The overall echo times (TE_1, TE_2, …, TE_n) are achieved by varying the echo time (TE_{iMSDE} = 4τ) in the iMSDE preparation.

The FSE readout was further modified to incorporate the combined parallel imaging and compressed sensing approach discussed above. An example of 3D *k*-space acquired by ARC is shown in Figure 5.5(a) and (b). Figure 5.5(a) shows the *k*-space sampling pattern for a 224 × 40 (k_y × k_z) matrix size with an ARC acceleration factor of 2 (2 × 1 in k_y × k_z direction). Figure 5.5(b) shows the acceleration factor of 4 (2 × 2). In ARC, the outer region of *k*-space is uniformly undersampled whilst the auto-calibration centre is fully sampled [182]. The auto-calibration centre was set to 32 × 32 in this study. For compressed sensing, the non-calibrated ARC *k*-space was further undersampled using a Gaussian pseudo-random distribution. Figure 5.5(c) and (d) shows the *k*-space using a CS factor 1.5 together with ARC accelerations of 2 × 1 and 2 × 2 respectively. Figure 5.5(e) and (f) show a higher CS factor of 2.0. Details of the image reconstruction are mentioned in the introduction section of this chapter.

The iMSDE with interleaved 3D FSE was developed by the author, the ARC option is embeded in the original readout. The CS acquisition and online-reconcontration algorithem were provided by Dr Scott Reid and Dr Kevin King from GE Healthcare.

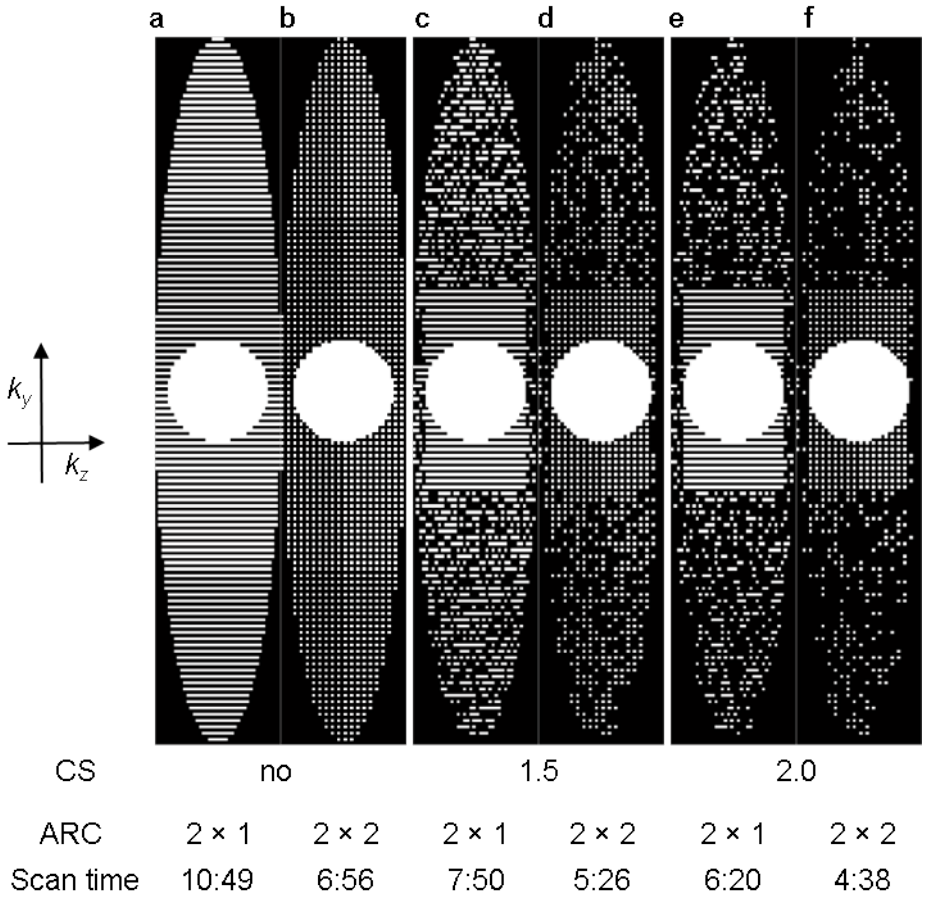

Figure 5.5 Under-sampled *k*-space patterns which are representative of the applied combinations of ARC ($k_y \times k_z$) and CS factors.

MRI Experiments

All the imaging experiments were performed using a 3 T system (MR750, GE Healthcare, Waukesha, WI), using a four channel phased-array neck coil (PACC, MachNet, Roden, The Netherlands).

Phantom study

The sequence was initially tested using the Eurospin Test Object (TO5) phantom (Diagnostic Sonar, Livingston, UK) which contains calibrated gels with known relaxivity values at 19º C. Nine gels were selected with a range of T_2 values which represent the T_2 values of plaque components previously reported in the literature (ranging from 52 to 143 ms). A three echo FSE sequence (TR = 2000 ms, TE = 21.6, 51.6, 81.6 ms) with the combination of two ARC values (2 × 1 and 2 × 2), without CS and with CS factors of 1.5 and 2.0 were used to acquire a total of six T_2 maps. The imaging matrix was 224×224×40, with field-of-view of 140×140×56 mm^3. A 2D multi-echo fast spin echo (MEFSE) sequence was acquired for comparison, with TR = 2000 ms and eight TEs from 8.6 to 68.8 ms with 8.6 ms intervals.

The imaging matrix for 2D MEFSE was 224×224, the field-of-view was 140×140 mm^2 and the slice thickness was 2 mm.

Volunteer study

Twelve healthy volunteers (eight men, mean age 34, range: 24-55 years) were recruited in this study, these volunteer experiments were conducted under an existing research ethics agreement and all volunteers gave informed written consent (R&D number: A091374). The volunteers were scanned with ARC 2 × 1 and without CS once, and with a CS factor of 1.5 twice. The repeated scan was used to determine the repeatability of the T_2 measurements, the average interval between the two scans was 14 days (range 7 to 28 days). Other scanning parameters of this sequence are listed in the last column of Table 5.1.

Sequence	TOF	Pre/Post-contrast DANTE T_1w FSE	MR-DTI	iMSDE T_2 mapping
Flip angle (°)	20	Variable flip angle	30	Variable flip angle
Echo train length	-	24	-	40
TE/TR (ms)	2.2/5.9	16.9/540	4.2/8.6	21.6, 51.6 and 81.6/2000
Acquired Matrix size	256×256×32	224×224×48	160×160×66	224×224×40
Acquired pixel size (mm^3)	0.5×0.5×2	0.6×0.6×1.4	0.5×0.5×1.4	0.6×0.6×1.4
Acquisition Time	1 min 35 s	2×6 min 26 s	4 min 42 s	7 min 48 s

Table 5.1 Imaging protocol for 3D multi-contrast MRI.

Patient study

Six patients (four men, mean age 80, range: 74-87 years) who had a carotid stenosis of at least 50% on Duplex ultrasound underwent this examination. A vacuum pillow was placed around the head and neck to minimise the movement. The standard protocol included multi-contrast 3D sequences in the coronal plane: a 3D time-of-flight (TOF) sequence, pre- and post-contrast DANTE prepared [89] 3D FSE sequence and pre-contrast MR-Direct Thrombus Imaging sequence (MR-DTI) [184]. The centre of the imaging volume was positioned at the middle of carotid bifurcation at both sides. Details of the scanning parameters are summarised in Table 5.1. The T_2 mapping sequence with a combination of CS factor of 1.5 and ARC 2 × 1 was used for the patient scanning. This separate study protocol was reviewed and approved by a local ethics committee and written informed consent was obtained from each patient.

Image analysis

The acquired images were first interpolated to 512×512×80, and then reformatted into the axial plane with a pixel size of 0.2×0.2×0.3 mm^3. For the phantom scans, regions of interest were defined within each gel and the mean and standard deviation (sd) of the T_2 values were recorded for each ARC and CS combination. For the volunteer scans, the analysis was performed on 10 contiguous slices of the common carotid artery (CCA) below the bifurcation on both sides. Vessel wall and lumen were manually segmented using a DICOM viewer (OsiriX 5.5.2, Pixmeo, Geneva, Switzerland). The ARC 2 × 1 without CS accelerated *k*-space data of the volunteers was saved and used off-line for simulating higher ARC and CS acceleration factors. Simulation experiments were performed using in-house software developed in MATLAB R2015b (MathWorks, Natick, Massachusetts, USA). Wall-lumen sharpness was quantified to measure the blurring for each of the ARC and CS accelerations [185]. A single axial slice of the common carotid artery (CCA) 5 mm below the bifurcation was chosen for the sharpness calculation. The image was first bilinearly interpolated at a factor of six to increase the image matrix, resulting in an interpolated pixel size of 0.03×0.03 mm^2. An intensity profile perpendicular to the vessel wall was drawn from the wall to the lumen. To determine image sharpness a synthetic image was created with the relative signal intensity of the lumen set to zero and the highest signal intensity in the vessel wall set to one. The wall-lumen sharpness was calculated by

$$\text{Sharpness} = 1/d \ (mm^{-1}) \tag{5.4}$$

Where *d* is the distance between pixels at an intensity between 0.8 and 0.2.

Data analysis

The statistical analysis was performed using the R programming language (version 3.2.2) [186]. The Shapiro–Wilk's test was used to test normality assumptions. Normally distributed data was presented as mean ± sd. A one-way ANOVA was used to compare T_2 measurements with different ARC and CS combinations. The concordance correlation coefficient (CCC) and Bland-Altman plots were used to evaluate the correlation and agreement between the 2D and 3D methods [187]. For the volunteer scans, the coefficient of variation (CoV: the ratio of the SD divided by the mean value) of T_2 values within each of the vessel wall with different CS and ARC combination were calculated. The intraclass correlation coefficient (ICC) was used to evaluate the agreement between two repeated scans. Statistical significance was defined as a p-value < 0.05.

5.4 Results

Phantom study

Figure 5.6(a) shows the measured T_2 values with different combinations of ARC and CS factors, the quantitative comparison found no significant difference between the different combinations (p = 0.999). Figure 5.6(b) shows the phantom T_2 values measured by 3D iMSDE FSE with ARC 2 × 1 and CS factors of 1.5 compared to the standard 2D MESE. A high correlation was noted between the two sequences for T_2 values ranging from 52 to 143 ms (r = 0.991). The CCCs between 2D and other 3D ARC and CS combinations were all above 0.9. Figure 5.6(c) shows the Bland-Altman plot comparing the two scans, with the bias of 3.0 ms and 95% limits of agreement -3.1 and 9.0 ms.

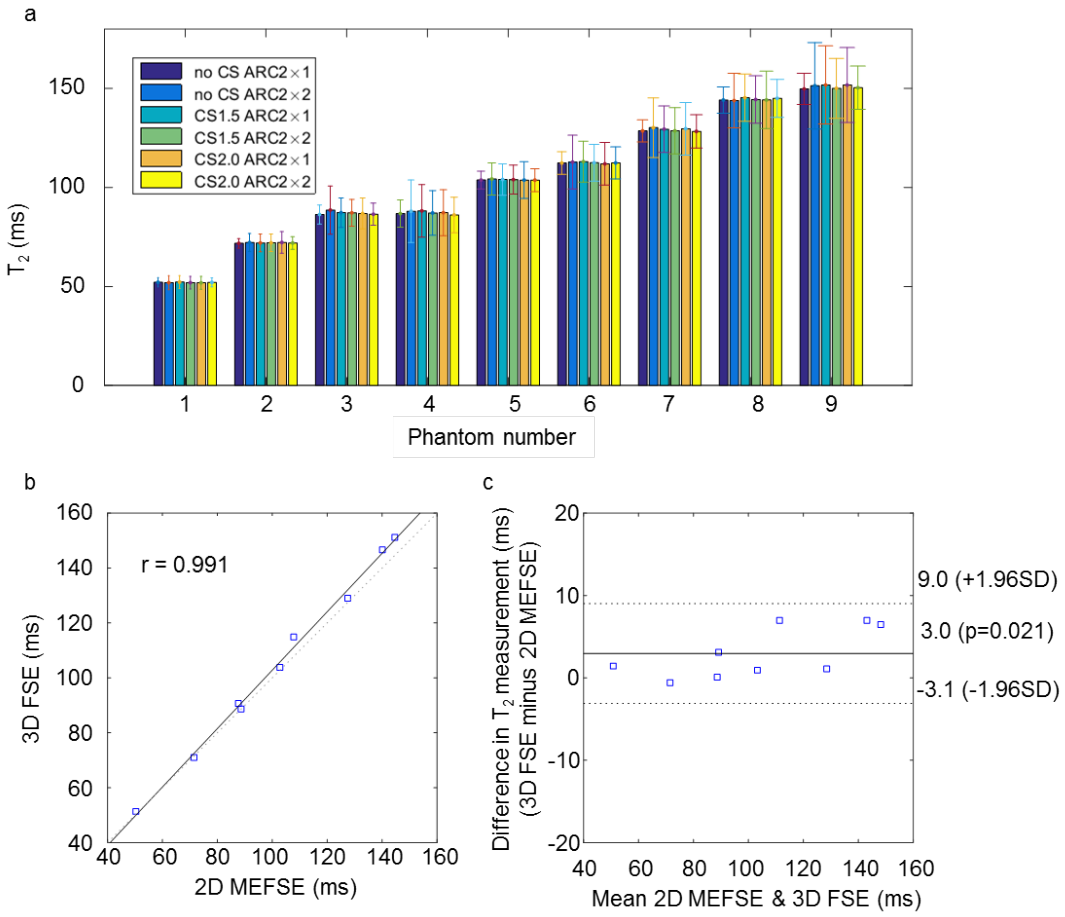

Figure 5.6 (a) Measured T_2 values of Eurospin phantom gels using a different combination of ARC and CS acceleration factors. (b) Concordance correlation of T_2 measurements obtained using 3D iMSDE FSE (ARC2 × 1 and CS1.5) and 2D MEFSE. (c) Bland-Altman plot of the difference versus the mean of the T_2 values using 3D iMSDE FSE (ARC2 × 1 and CS1.5) and 2D MEFSE.

Volunteer study

All twelve volunteers (100%) completed the MR studies; good blood suppression being achieved on all the images. Figure 5.7(a) shows a volunteer image without compressed sensing (ARC 2 × 1), (b-f) shows the reconstruction image from retrospectively subsampled *k*-space from (a). The vessel wall boundaries become blurred with increasing CS factors, and the noise level increases with increasing ARC parallel acceleration factors. The wall-lumen sharpness values comparing each combination obtained from 24 arteries across 12 volunteers is shown in Figure 5.8. Figure 5.8(a) shows how the image sharpness was defined. In Figure 5.8(b), the non-CS accelerated image has the highest wall-lumen sharpness (1.9 mm^{-1}). With ARC 2 × 1 and CS 1.5, the image has a higher wall-lumen sharpness compared with CS 2.0 (1.7 vs. 1.4 mm^{-1}).

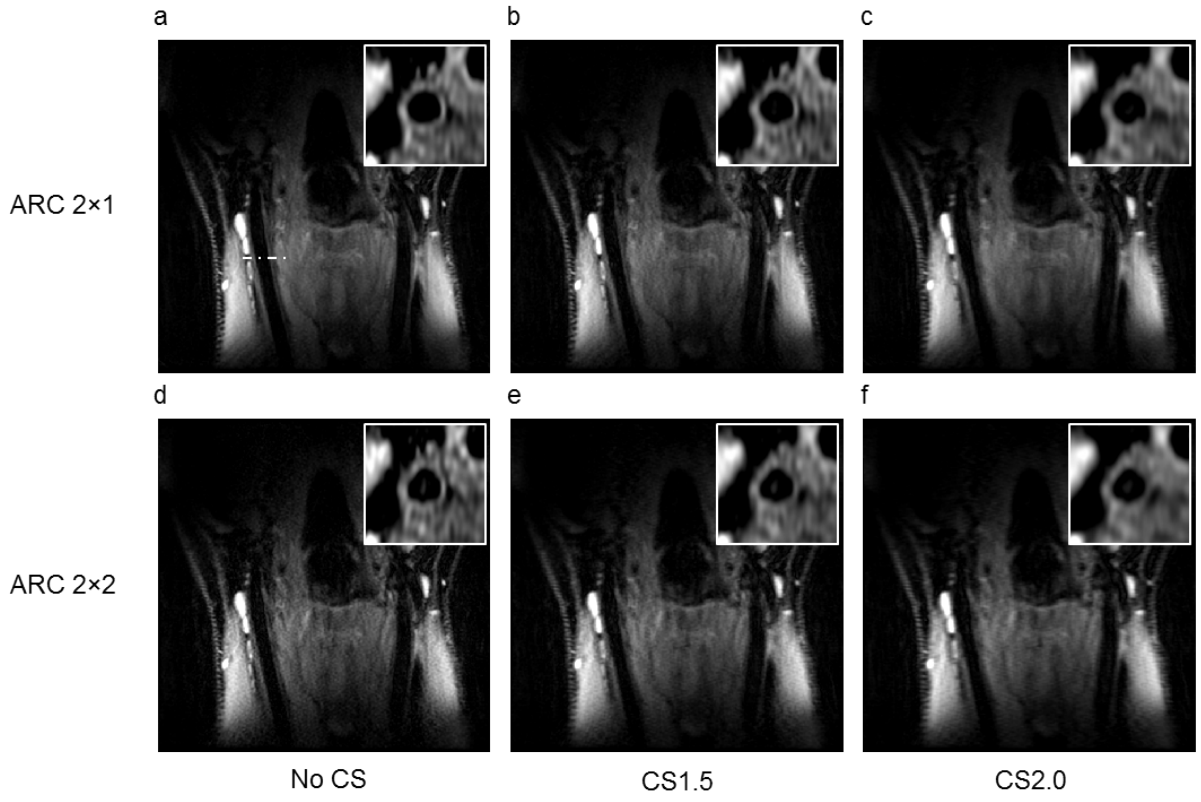

Figure 5.7 Simulation experiment comparing ARC and increasing CS accelerations in a healthy volunteer. The scaled top-right corner images are the reformatted axial projections.

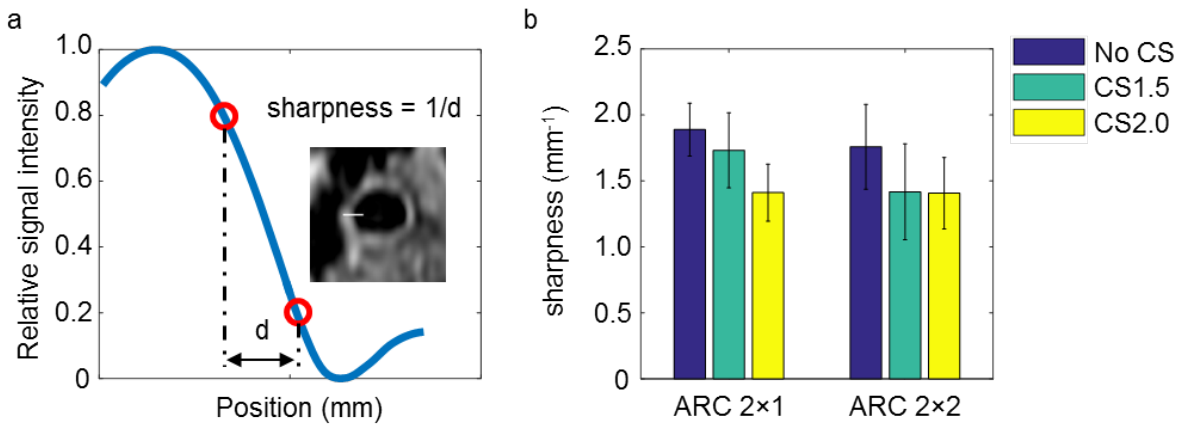

Figure 5.8 (a) With blood suppression the signal intensity drops from wall to lumen. The line profile was drawn from wall to lumen to determine the wall-lumen sharpness. (b) Compares wall-lumen sharpness for the volunteer cohort using ARC and CS combinations measured in both carotid arteries (n = 24 arteries).

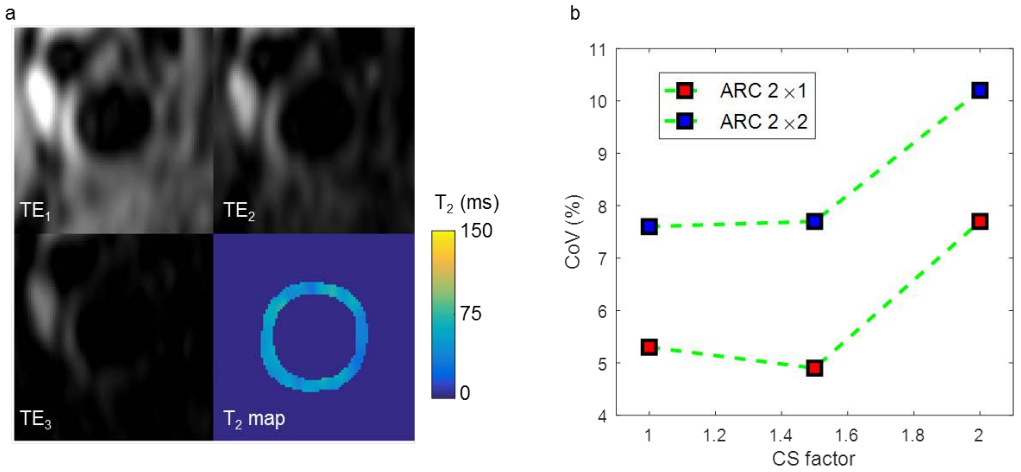

Figure 5.9 Images of a volunteer with different echo times and the resultant T_2 map (with ARC2 × 1 and CS1.5). (b): Plots the Coefficient of Variation (CoV) compare the ARC and CS combinations from the volunteers' arteries (n = 24).

Figure 5.9(a) shows the T_2 map from one volunteer with a CS factor 1.5 and ARC 2 × 1. Figure 5.9(b) shows the CoV of T_2 values of measured slices in each combination. CoV remains similar when CS factor is below 1.5 and increases when CS factor increased to 2.0. ARC 2 × 2 has a higher CoV compared to ARC 2 × 1. The mean T_2 value for the volunteer carotid wall was 48.0 ± 9.5 ms. Good repeatability was found between the two scans (ICC: 0.93, 95% CI 0.84-0.97). According to the noise level from Figure 5.9 and wall-lumen sharpness evaluation in Figure 5.8, a combination of ARC 2 × 1 and CS factor of 1.5 was chosen for the patient study.

Patient study

Five of the six patients (83%) completed the scans. Eight carotid plaques were found in the five patients. Recent IPH was found in four plaques, and fibrous tissue was found in two of the plaques. The overall T_2 values of the plaques were 54.9 ± 12.2 ms. The mean wall-lumen sharpness of the 10 CCAs from these five patients was 1.5 ± 0.3 mm^{-1}, which is similar to volunteer scans.

Figure 5.10 shows an example of a right carotid plaque from a patient. The white arrow shows the region of hyperintensity in T_1w, hypointensity in post-contrast T_1w, and hyperintensity signal in MR-DTI. This region was indicative of recent IPH. T_2 mapping shows higher T_2 values in the recent IPH (88.1 ± 6.8 ms) compared to other plaque regions. Figure 5.11 shows a plaque with fibrous tissue inside. The fibrous shows hyperintense signal in post-contrast T_1w and the third echo of T_2 mapping sequence (T_2w). The T_2 values for the fibrous tissue were 62.7 ± 9.3 ms.

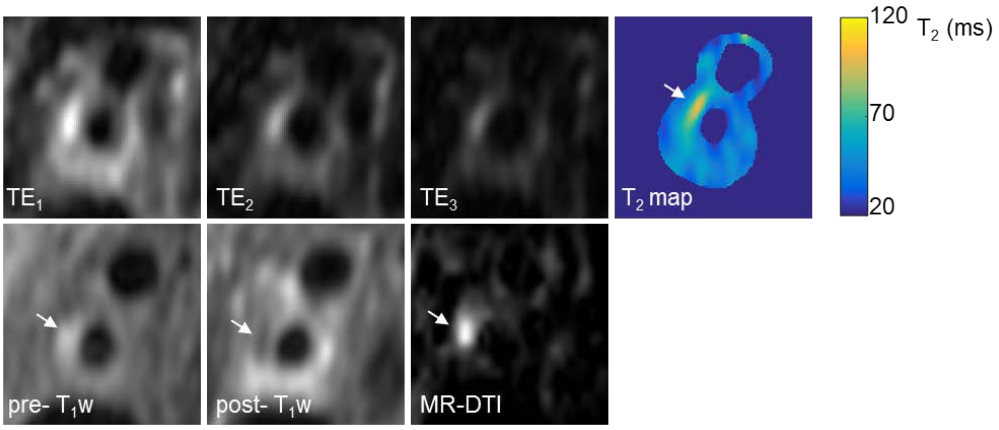

Figure 5.10 An example of recent IPH (while arrow) identified using a multi-contrast MRI protocol. Recent IPH shows higher T_2 values than the surrounding plaque region.

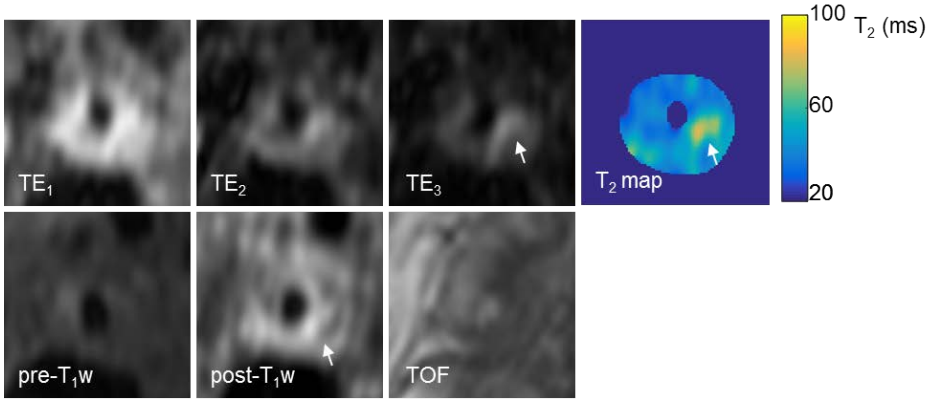

Figure 5.11 Multi-contrast MRI shows fibrotic tissue in the plaque. The fibrous tissue has higher T_2 values than the surrounding plaque components.

5.5 Discussion

This study, for the first time, shows the combination of compressed sensing and parallel imaging to reduce the time of 3D T_2 mapping to a clinically acceptable acquisition time (7 min 48 s) compared with the non-accelerated scans (over 10 mins). T_2 mapping sequences in carotid plaque have shown the ability to differentiate plaque components [102], which could be used for plaque segmentation and identification of high-risk components [104, 105]. Whilst compressed sensing [179, 188-190] and parallel imaging [178, 188, 191, 192] have been introduced for multi-contrast carotid vessel wall imaging, these acceleration techniques have not yet been reported for 3D T_2 mapping. In this study, the measured T_2 values from the volunteers' healthy carotid vessel walls and plaque components from patients are similar to previous studies [104, 106]. Furthermore, this T_2 mapping sequence could also be used to simultaneously obtain PD and T_2 weighted images, with the first echo of TE/TR = 21.6/2000 ms, and the third echo of TE/TR = 81.6/2000 ms.

Rapid 2D T_2 mapping can be achieved by using multi-echo fast spin echo sequences [102, 104, 106], which can acquire images with different TEs in one TR. However, it becomes challenging when extending into 3D, since most 3D sequences do not allow interleaved multi-echo acquisitions and the *k*-space view-ordering is more complicated. To achieve T_2 mapping, one method is to change the TE in the preparation pulse, either in a T_2 preparation [193] or preferably combined in a black-blood iMSDE preparation [160]. Studies have demonstrated that both FSE [193] and GRE [160] based readouts could achieve good T_2 mapping results. The long TR in FSE based T_2 mapping sequences allows the magnetisation to fully recover after each readout segment, which enables images with different TEs to be acquired in an interleaved fashion. Therefore the "echoes" are intrinsically registered. In comparison to acquiring images with different TEs sequentially, this method does not need additional image registration in the post-processing which could induce extra variability [160].

The main limitation of this study is the absence of histological validation of the plaques. Since the participating patients were asymptomatic, they were not scheduled for surgery. However, the phantom validation in this study showed good accuracy and the measurements of carotid wall T_2 values in both volunteers and patients are in good agreement with other studies [102, 104, 106]. The second limitation is that the study only has a small number of patients. A third limitation is that cardiac gating was not used in these sequences. However, Zhu et al showed that ungated sequences could achieve comparable vessel SNR and CNR than gated sequence in black blood FSE based carotid imaging [194]. The accuracy of gated and ungated T_2 mapping sequences needs further exploration. The

fourth limitation is that the CS reconstruction algorithm used in this study was developed for general application, and not specifically optimised for imaging the carotid wall. Further optimisation of the reconstruction parameters could potentially improve image quality, however this is outside the scope of this study. The last limitation would be that in this study, a specific CS reconstruction and the sequential combination of CS and ARC were used, which may not be the optimum process. There are also other CS algorithms [195-197] and different combination of CS with PI [198, 199] or other acceleration methods [200, 201] existing in the literature that might worth exploring. However this is outside of the scope of current work. A recent paper described a combination of CS and principal component analysis could derive T_2 information from a single scan [202]. However the feasibility of this method in carotid plaque imaging needs to be explored as blood suppression is necessary for vessel wall imaging. The method used in the current study is a straightforward implementation of a black-blood sequence with a combined PI + CS reconstruction method.

5.6 Conclusion

This study demonstrates the combination of CS and ARC for accelerating 3D blood-suppressed T_2 mapping in the carotid artery, using an interleaved variable TE iMSDE based black-blood preparation scheme. These acceleration techniques reduce the 3D T_2 mapping sequence to a clinically acceptable acquisition time of 7 min 48 s for three echoes with a high acquired spatial resolution of 0.6×0.6×1.4 mm^3.

The specific hypotheses investigated in this chapter, that *[Hypothesis 5]* the CS and PI accelerated 3D T_2 mapping sequence can achieve accurate T_2 measurement with good reproducibility and *[Hypothesis 6]* the CS and PI accelerated 3D T_2 mapping sequence is clinically feasible and can measure different T_2 values between plaque components, were proved.

Chapter 6 Three-dimensional black-blood multi-contrast protocol for carotid imaging using compressed sensing: a repeatability study

Following Chapter 5, this chapter extends the use of CS to a 3D FSE based multi-contrast protocol, which comprises DANTE prepared T_1w, iMSDE prepared T_2w and PDw sequences. The proposed protocol was tested in a cohort of 12 volunteers and eight patients. Vessel wall morphological features, including wall/lumen area and wall thickness were measured. The scan-rescan repeatability, inter/intra-observer agreement were tested. This chapter investigates the following hypotheses:

> *[Hypothesis 7]* the repeatability of carotid vessel wall measurements is high in sequences with and without CS acceleration.
>
> *[Hypothesis 8]* the inter/intra-observer agreement of carotid plaque measurements is high in patients.

Aspects of this work have been presented at ISMRM 25th Annual meeting, 2017. No.3118.

6.1 Introduction

A multi-contrast MR protocol comprising PDw, T_1w and T_2w sequences could identify high-risk intraplaque components with high sensitivity and specificity [203]. Multi-contrast MRI has been used in the previous studies for plaque classification [203], component segmentation [204, 205] and also to determine the age of intraplaque hemorrhage [39].

Black-blood techniques have been used to suppress the blood signal in the lumen to improve vessel wall visualisation. This is usually achieved in 2D imaging with the use of magnetisation preparation schemes such as DIR [86, 178, 206], or QIR [87]. For 3D imaging, non-selective preparation schemes such as MSDE [88, 113] or DANTE [89, 144] have been used. Volumetric (3D) readout based on either FSE [204, 207-209] or GRE [144] allows the acquisition of near isotropic voxels which could potentially improve the plaque component quantifications. However, one of the disadvantages of 3D protocols in previous carotid studies is the long overall acquisition time (approximately 20-45 min), which could lead to poor patient compliance [117].

Several techniques have been introduced to reduce the 3D acquisition time. Parallel imaging (PI) methods have been introduced, with the use of multi-channel coils [178, 192, 210]. Dedicated pulse sequences have also been developed to acquire multiple contrast weightings in a single acquisition, such as the Multi-contrast Atherosclerosis Characterization (MATCH) sequence, which can acquire hyper T_1w, grey blood, and T_2w images in a single 5-min sequence [211]. More recently, the method of compressed sensing (CS) has been introduced into MRI as an alternative method to accelerate image acquisition [212], and has been applied to carotid imaging [179, 190, 213]. Whilst the first two techniques (PI and MATCH) have been used for multi-contrast purposes, the use of CS has not previously been validated in a multi-contrast protocol.

The purpose of this work, therefore, is to evaluate the use of CS within a current standard carotid multi-contrast protocol. Volunteer scans were carried out to evaluate the interscan reproducibility and patients with carotid atherosclerotic diseases were recruited to validate inter/intra-observer reproducibility of the morphology measurements based on the CS accelerated sequences.

6.2 Materials and methods

Study subjects

This study had ethical approval and informed consent was obtained from each volunteer and patient. Twelve volunteers (eight men, mean age 34, range: 24-55 years) and eight patients (four men, mean age 75, range: 72-87 years) with a carotid artery stenosis greater than 50% on duplex ultrasound were scanned on a 3 T MRI system (MR 750, GE Healthcare, Waukesha, WI), using a four channel phased-array neck coil (PACC, MachNet, Roden, The Netherlands). To evaluate the interscan reproducibility of the sequences, the twelve volunteers were scanned for a second time using the same protocol. The time interval between the two scans was 14 days (range 7 to 28 days).

Imaging protocol

All the subjects were imaged using a multi-contrast protocol listed in Table 6.1. Coronal imaging slabs of the 3D sequences were centred at the carotid bifurcation. The compressed sensing was achieved in the similar method describe in Chapter 5.

Contrast	Time-of-flight	T_1w	PDw	T_2w
Sequence	3D SPGR	3D FSE	3D FSE	3D FSE
Blood suppression	-	DANTE	iMSDE	iMSDE
Echo time (ms)	2.2	16.9	21.6	51.6
Repetition time (ms)	5.9	540	2000	2000
Flip angle (°)	20	Variable flip angle	Variable flip angle	Variable flip angle
FOV (mm^3)	140×140×64	140×140×67	140×140×56	140×140×56
Acquisition matrix	256×256×32	224×224×48	224×224×40	224×224×40
ARC Parallel Imaging (phase×slice)	-	-	2×1	2×1
CS acceleration	Non-CS	Non-CS/1.5/2.0	1.5	1.5
Acquisition time	1:35	3:16/2:13/1:41	2:36	2:36

Table 6.1 Scanning parameters for the multi-contrast protocol.

T_1w images were acquired by a DANTE [89] prepared 3D FSE sequence. Images were acquired without CS acceleration, and with CS acceleration factors of 1.5 and 2.0. The scanning times were 3 min 16 s, 2 min 13 s and 1 min 41 s, respectively. The parameters for DANTE preparation were: the number of pulses: 150; gradient amplitude: 3 G/cm; gradient axes: X, Y and Z; flip angle: 13°; DANTE pulse repetition time: 1ms. No parallel imaging was used for the T_1w images. T_2w and PDw images were acquired using an iMSDE [88] prepared 3D FSE sequence. The first-order moment (m_1) was set to 412 $mTms^2/m$ following empirical observations to attain sufficient blood suppression [180]. A CS acceleration factor of 1.5 was used. The scanning time was 2 min 36 s for both of the sequences. The CS and ARC were combined in a sequential way [214]. Fat suppression was performed using an Adiabatic SPectral Inversion Recovery (ASPIR) pulse. The acquired resolution for T_1w, T_2w and PDw was 0.6×0.6×1.4 mm^3. Cardiac gating was not used in the protocol.

Image analysis

The acquired multi-contrast images were first reformatted into the axial plane, and then interpolated into a voxel size of 0.2×0.2×0.3 mm^3, using MATLAB (The MathWorks, Inc., Natick, MA). Carotid artery lumen and outer wall boundaries were manually drawn by an experienced observer who has more than two years' experience in carotid imaging, using a DICOM viewer (OsiriX 5.5.2, Pixmeo, Geneva, Switzerland).

For the volunteer images, five contiguous slices in the common, internal and external carotid artery (CCA, ICC and ECA), 5 mm below and 5 mm above the bifurcation were used for morphological measurements. The lumen area was defined as the area inside the lumen contour, and the wall area was defined as the area between the outer wall boundary and inner lumen contour. The mean radius of the lumen and outer wall was calculated by simplifying the geometry as a circle with the same area. The mean wall thickness was determined as the difference between lumen radius and outer wall radius. The wall-lumen sharpness was also calculated for each CS factor in the T_1w sequences [185]. For the patient images, the vessel wall and lumen boundaries were manually drawn on each of the slices containing atherosclerotic plaque. The plaque was defined as a focal wall thickness ≥1.5 mm [141]. To test the intra-observer reproducibility, the T_1w images with a CS factor of 1.5 were analysed twice by the same observer. To test the inter-observer reproducibility, the T_1w images were analysed by a second observer who also has 2 years of carotid imaging experience, and the results were compared with the first observer. Both of the observers made their measurements independently and were blinded to the subjects' clinical information.

Statistical analysis

Interclass correlations (ICCs) were calculated to evaluate the agreement of wall/lumen area and wall thickness measurements between two volunteer scans. The measurement differences from T_1w images between two scans were analysed using the Bland-Altman method [187]. The inter/intra-observer variabilities from the patients scans were also evaluated using the ICC. An ICC value above 0.75 was considered as excellent agreement. 0.40-075 was good agreement and below 0.40 was poor agreement [215]. A two-tailed paired student's t-test was used to compare the wall thickness measurements between non-CS and CS accelerated T_1w sequences in patients. Statistical significance was defined if $p<0.05$. Continuous data were presented as mean ± standard deviation. The statistical analysis was performed using R (version 3.2.2) [167].

6.3 Results

All the twelve volunteers completed the scans. Seven out of eight patients completed the scan. One patient did not finish the scan due to discomfort.

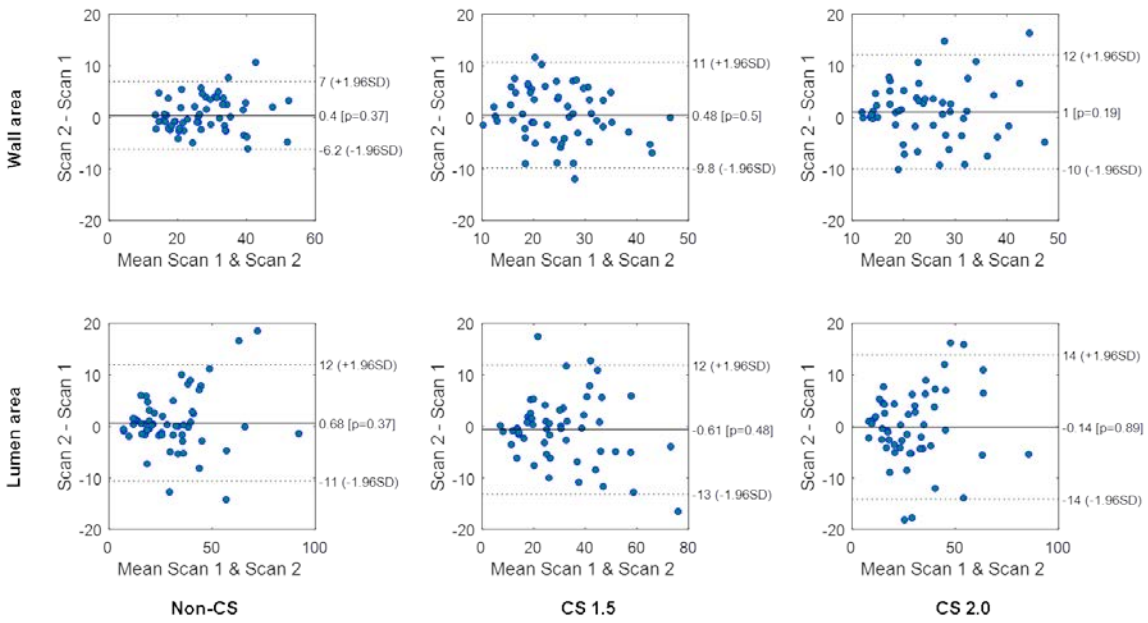

Figure 6.1 Bland-Altman plots of volunteer lumen and wall area measurements from T_1w sequences between two repeated scans (all units: mm^2).

Figure 6.1 shows the Bland-Altman plots of lumen and wall area measurement of volunteer T_1w images between two scans with non-CS, CS factor of 1.5 and 2.0. The ICC (95% CI) for lumen and wall area measured from the repeated volunteer scans using the three multi-contrast sequences with CS factor of 1.5 are shown in Table 6.2. Excellent correlation of wall/lumen area measurement were found between two scans (all ICCs > 0.80). Figure 6.2 shows the wall-lumen sharpness calculated from the T_1w volunteer images. The sharpness decreases with increasing CS factor.

	PDw	T_1w	T_2w
Wall area	0.95 (0.92-0.97)	0.81 (0.69-0.88)	0.97 (0.94-0.98)
Lumen area	0.96 (0.92-0.97)	0.92 (0.87-0.95)	0.96 (0.94-0.98)

Table 6.2 The ICC (95% CI) for lumen and wall area measured from repeated volunteer scans at three contrast weighted sequences with CS factor of 1.5.

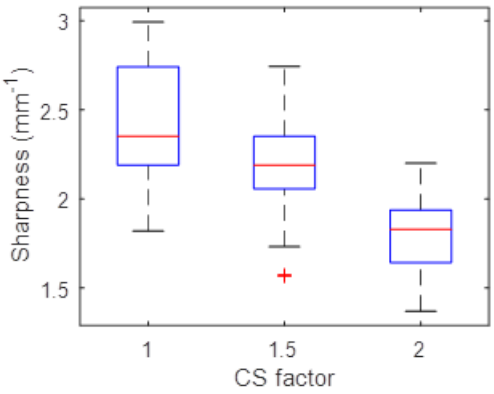

Figure 6.2 The wall-lumen sharpness measured from volunteer T_1w images with different CS factors.

Figure 6.3 shows an example of a patient image with intra-plaque haemorrhage. From the T_1w images, the wall-lumen and outer wall boundaries become blurred with increasing CS factor. However, for the wall thickness measurement, there are no significant differences comparing the CS accelerated sequence with the non-CS sequence (Non-CS vs. CS1.5: 2.43 ± 0.57 vs. 2.58 ± 0.87 mm, p = 0.58; Non-CS vs. CS2.0: 2.43 ± 0.57 mm vs. 2.39 ± 0.85 mm, p = 0.59). When compared to the volunteers, the patients have a thicker wall thickness ($p<0.01$), as shown in Figure 6.4.

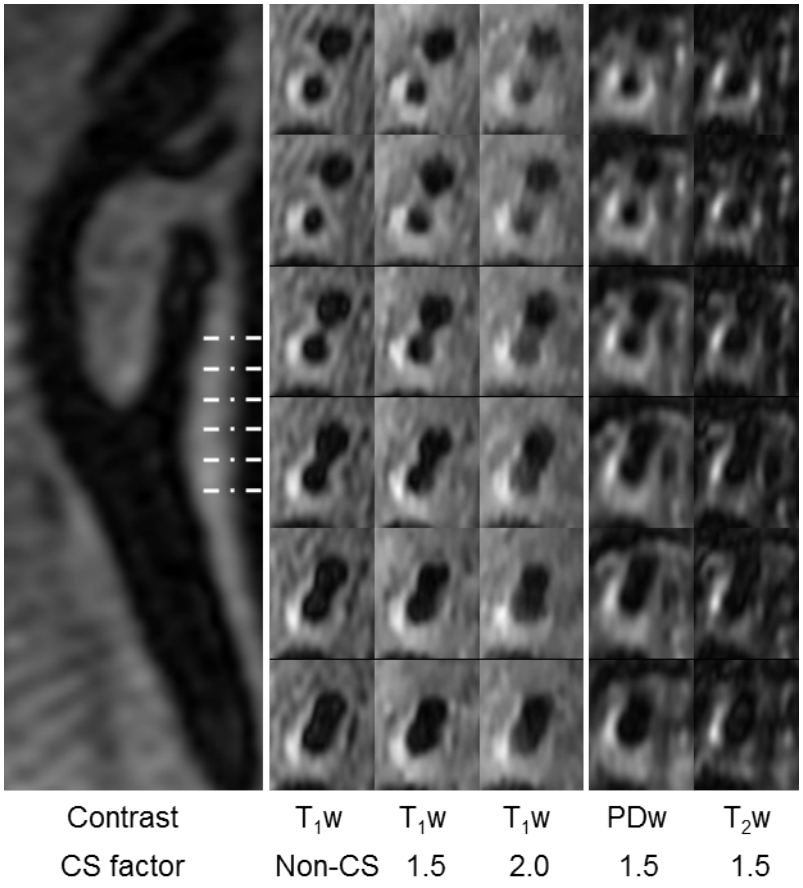

Figure 6.3 Multi-contrast carotid images of an 80-year-old male. The plaque contains an intra-plaque haemorrhage.

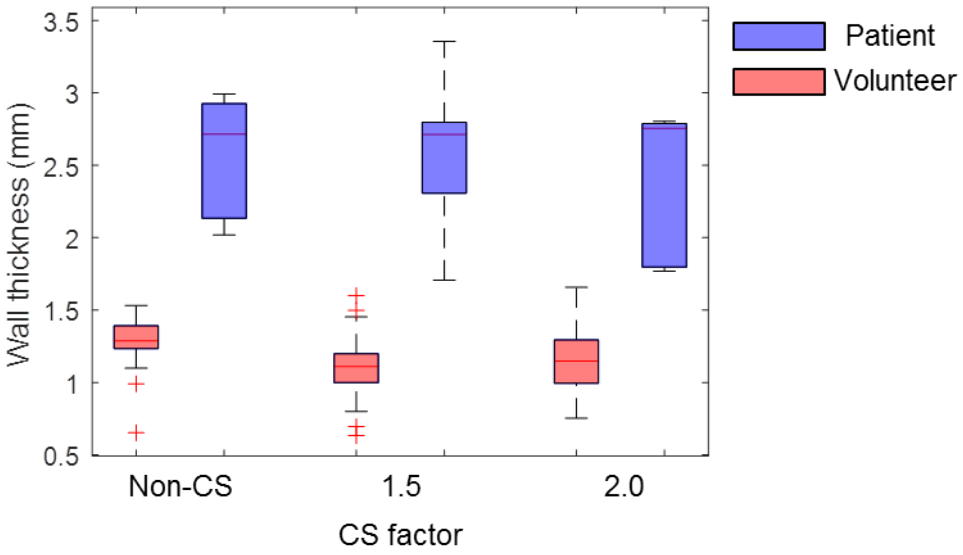

Figure 6.4 Volunteer and patient's wall thickness at different CS factors of T_1w images.

Table 6.3 shows the ICC with 95% CI of the intra-observer reproducibility in measuring the lumen/wall area and wall thickness in multi-contrast sequences from the patients. All the

ICCs were above 0.81. Table 6.4 shows the inter-observer reproducibility of lumen/wall area and wall thickness of the patients using PDw, T_1w and T_2w images. The ICCs were all higher than 0.83.

	PDw	T_1w	T_2w
Wall area	0.86 (0.51-0.98)	0.84 (0.50-0.96)	0.82 (0.43-0.97)
Lumen area	0.98 (0.95-0.99)	0.98 (0.92-1.00)	0.98 (0.96-0.99)
Wall thickness	0.98 (0.96-0.99)	0.86 (0.57-0.96)	0.97 (0.95-0.99)

Table 6.3 ICC (95% CI) for the intra-observer measurements of the multi-contrast protocol using CS factor of 1.5 from patients' scans.

	PDw	T_1w	T_2w
Wall area	0.84 (0.50-0.96)	0.87 (0.40-0.98)	0.86 (0.51-0.97)
Lumen area	0.98 (0.95-0.99)	0.95 (0.77-0.99)	0.98 (0.93-0.99)
Wall thickness	0.98 (0.94-0.99)	0.92 (0.63-0.97)	0.95 (0.89-0.99)

Table 6.4 ICC (95% CI) for the inter-observer measurements of the multi-contrast protocol using CS factor of 1.5 from patients' scans.

6.4 Discussion

This study demonstrates, for the first time, the usefulness of CS acceleration in a multi-contrast black-blood carotid protocol to reduce the overall acquisition time at 3 T. The results show that CS accelerated sequences have a good scan-rescan reproducibility in carotid morphological measurement in volunteers, and good inter/intra-observer reproducibility of morphological measurement in patients.

Multi-contrast MRI has been used widely in assessing plaque components and vulnerability [144, 203, 204, 216-224]. Originally this was performed at 1.5 T [203, 216-220], however the studies are now more commonly performed at 3 T due to the superior signal-to-noise ratio (SNR) and contrast-to-noise ratio (CNR) [221-223, 225-227]. In addition, the development of 3D sequences allows for larger coverage, better through-plane resolution, higher scanning efficiency, less motion artefact and more precise plaque segmentation [144, 204, 211]. Whilst acceleration techniques such as PI have been introduced and validated [178], the use of CS has not previously been validated for the multi-contrast protocol. The CS techniques has been used in carotid studies to reduce the acquisition time of the sequences, such as MERGE [164, 179, 190, 228] and black-blood dynamic contrast enhance MRI [229]. The

studies showed the CS can be used to accelerate the carotid MRI scanning time without impacting the diagnostic quality, reduce the motion artefact and achieve higher temporal resolution in the dynamic images. Previous study also has demonstrated that CS produces better image quality than PI [230], and that the combination of CS and PI can achieve even better image quality than either of the techniques used alone [231]. This study for the first time, tested the scan-rescan reproducibility and intra-inter observer repeatability of carotid morphological measurement in a multi-contrast protocol. The results showed that wall area, lumen area and wall thickness is reproducible in a CS accelerated multi-contrast protocol. The CS algorithm used in this study is a productised reconstruction with accepted reconstruction time.

The results in this study showed that the wall-lumen sharpness decreases as the CS factor increases (Figure 6.2), and the CoV of scan-rescan on volunteer T_1w images has increased. This indicates that the CS could bring extra uncertainty in the morphological measurement.

There are several limitations in this study. Firstly, the number of patients is quite small. Only eight patients were scanned using the current multi-contrast protocol. Therefore only limited plaque components and examples were investigated. However, good reproducibility of the quantitative analysis from the volunteer scan demonstrates the feasibility of applying the CS-accelerated protocol for future large scale patients scanning. The second limitation is that a coronal acquisition with anisotropic resolution was used in this study to as a trade-off between blood suppression, image SNR, scanning time and coverage. This may lead to limitations in the wall thickness measurements and potentially effect the plaque characterization in the reconstructed axial image. Nevertheless, the result from the current scanning settings showed good repeatability of the wall thickness measurements. Future optimisation should consider the use of isotropic resolution acquisitions for better plaque characterization, especially benefit for axial images. The third limitation is that the CS reconstruction method used in this study was a vendor provided on-line algorithm which was optimised for clinically acceptable reconstruction times. Further optimisation of the acquisition and reconstruction parameters, or to even use the multi-contrast sequences for joint reconstruction [232], could potentially improve the image quality, albeit probably at the expense of increased reconstruction time. Fourthly, considering the limited scanning time in practice, ARC acceleration of 2×1 and only a single CS factor of 1.5 was used for PDw and T_2w sequences. The results from the T_1w may not necessarily be extrapolated to these two contrast weighted images. The last limitation is that a fixed echo train length was used in this study, as we primarily considered the CS as an additional feature to the existing optimised

protocol setup. Longer echo train length with optimised flip angle schemes could further reduce the acquisition time but this is outside the scope of this study.

6.5 Conclusion

In conclusion, this study shows that the current 3D carotid black-blood multi-contrast protocol could be accelerated by CS, in additional to PI, with robust and reproducible morphology measurements. With current protocol setup, CS of 1.5 with the combination of paraller imaging acceleration factor of two can be used for the multi-contrast protocol. Multi-contrast vessel wall imaging protocol could use CS to further reduce the acquisition time.

The results prove the specific hypotheses investigated in this chapter that *[Hypothesis 7]* the repeatability of carotid vessel wall measurements is high in sequences with and without CS acceleration and *[Hypothesis 8]* the inter/intra-observer agreement of carotid plaque measurements is high in patients.

Chapter 7 The development and optimisation of 3D black-blood R_2* mapping of the carotid artery wall

This chapter describes the development and optimisation of a 3D black-blood R_2* mapping sequence for carotid vessel wall. Different blood suppression techniques are compared by Bloch simulation and volunteer image SNR and CNR analysis. Three different *k*-space view orderings are compared. Blood-suppression efficiency, vessel wall and adjacent sternocleidomastoid muscle R_2* values are compared with different methods. This chapter tests the following hypotheses:

> *[Hypothesis 9]* the blood suppression techniques do not influence the measurement of R_2* values in the carotid vessel wall.
>
> *[Hypothesis 10]* optimal blood suppression, *k*-space view ordering and acquisitions-per-short could achieve good black-blood vessel wall R_2* mapping.

Aspects of this work have been presented at ISMRM 25th Annual meeting, 2017. No.2787.

7.1 Introduction

The measurement of the T_2*/R_2* relaxation time has been used to assess iron concentration in the myocardium [233, 234], and liver [235] as well as being used to monitor the uptake of Ultra-small Superparamagnetic Particles of Iron Oxide (USPIO) in the vessel wall [236-239]. Good reproducibility has been found when using conventional multi-echo gradient-echo based T_2*/R_2* sequences [240]. Recently, black-blood preparation based on DIR has been introduced for cardiac T_2* imaging with improved myocardial-to-blood contrast, clearer myocardial borders, and less blood signal contamination [241-243]. Black-blood T_2* sequences have reportedly achieved comparable T_2* measurement, and superior reproducibility compared to bright-blood sequences [241-243].

In vessel wall imaging, the 2D black-blood T_2* sequences using DIR or QIR have been used to distinguish symptomatic from asymptomatic plaque [244]. Significant differences in T_2* values have also been found in different plaque components [102]. Changes in T_2*-weighted imaging following the administration of USPIO have been used as a surrogate biomarker for changes in plaque inflammation [245-249].

However, currently there are limited studies exploring the application of the advanced blood suppression techniques, such as iMSDE and DANTE for 3D T_2* mapping [250, 251]. The aim of this study was to develop an optimised a 3D black-blood T_2* sequence for carotid vessel wall imaging. Two different 3D black-blood preparations were compared for the image quality. Three different *k*-space view orders were designed to allow the minimal number of black-blood pulses to be used in the acquisition. The *k*-space view orders were optimised through Bloch simulation and evaluated in a volunteer study,. The inversion of T_2* relaxivity, R_2* = 1/T_2^*, is used in this study, since it has a positive linear relationship with tissue iron concentration [235].

7.2 Materials and Methods

Sequence

The basic sequence consists of a blood suppression module, followed by a fat-suppressed 3D multi-echo fast spoiled gradient echo sequence (ME-FSPGR), with a delay time (Td) at the end. Figure 7.1(A) shows the sequence diagram for one shot. Two black-blood techniques, iMSDE (Figure 7.1B) [252] and DANTE (Figure 7.1C) [253], were compared. The iMSDE module consists of a non-selective 90˚ tip-down pulse, two composite 180˚ refocusing pulses and a -90˚ tip-up pulse. Motion sensitive gradients were used between the RF pulses for blood suppression. The DANTE preparation comprises a train of low amplitude hard RF pulses interspersed with gradients applied along all three directions.

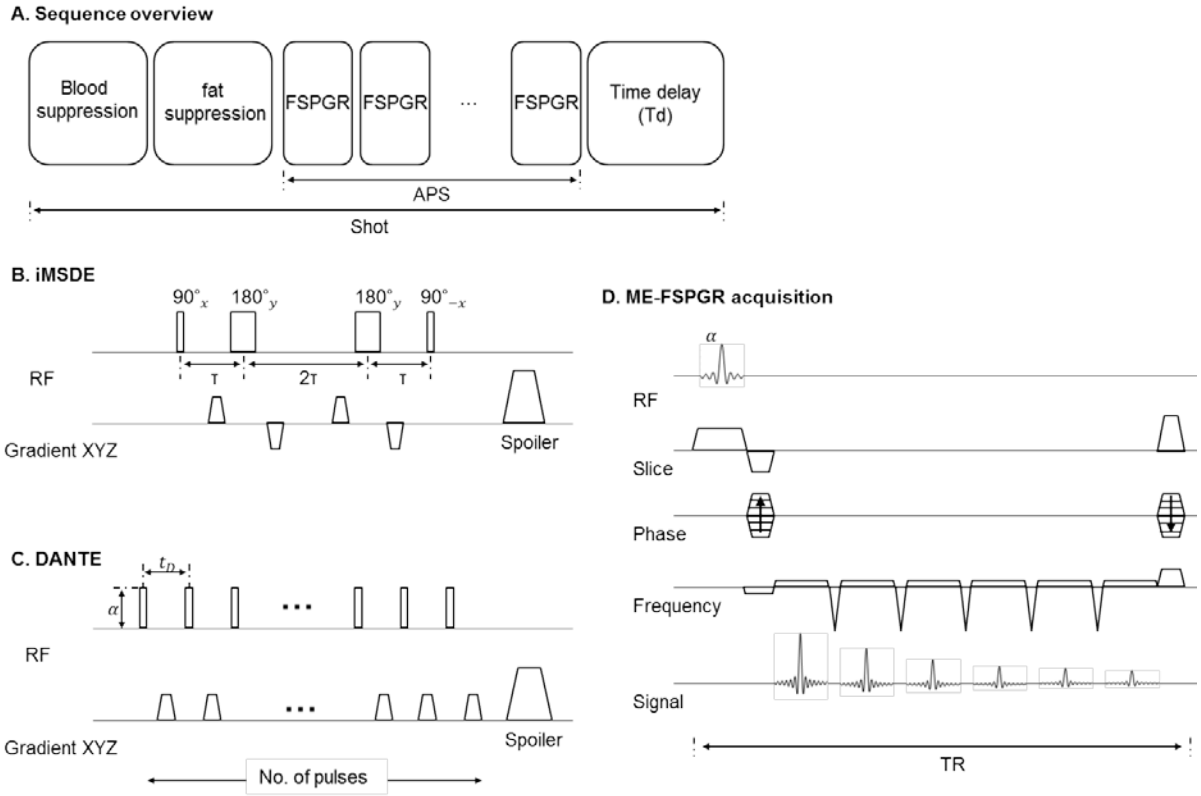

Figure 7.1 Overview of the black-blood ME-FSPGR sequence in one shot. (A) A shot consists of blood suppression preparation pulse, a standard chemical saturation pulse, and multiple acquisitions. The number of acquisition is defined as acquisitions-per-shot (APS). A delay time (Td) is used at the end of each shot. Two different blood suppressions, iMSDE (B) and DANTE (C) were used. T is the time interval between the 90˚ and 180˚ pulse in iMSDE. α is the flip angle in DANTE. t_D is the repetition time of DANTE pulse. (D) The ME-FSPGR acquisition contains six echoes.

Fat saturation was achieved using a standard chemical shift saturation pulse. Each shot comprises the blood suppression preparation, fat suppression, multiple ME-FSPGR acquisitions and Td (Figure 7.1D). The number of ME-FSPGR acquisitions-per-shot (APS) is user selectable. Each ME-FSPGR acquisition comprises six echoes. The delay time (Td) is applied at the end of the FSPGR acquisitions to allow the magnetisation to recover and improve the overall SNR. During the readout, the *k*-space points in the k_y-k_z plane were acquired per their distance from the *k*-space centre to achieve optimal blood suppression.

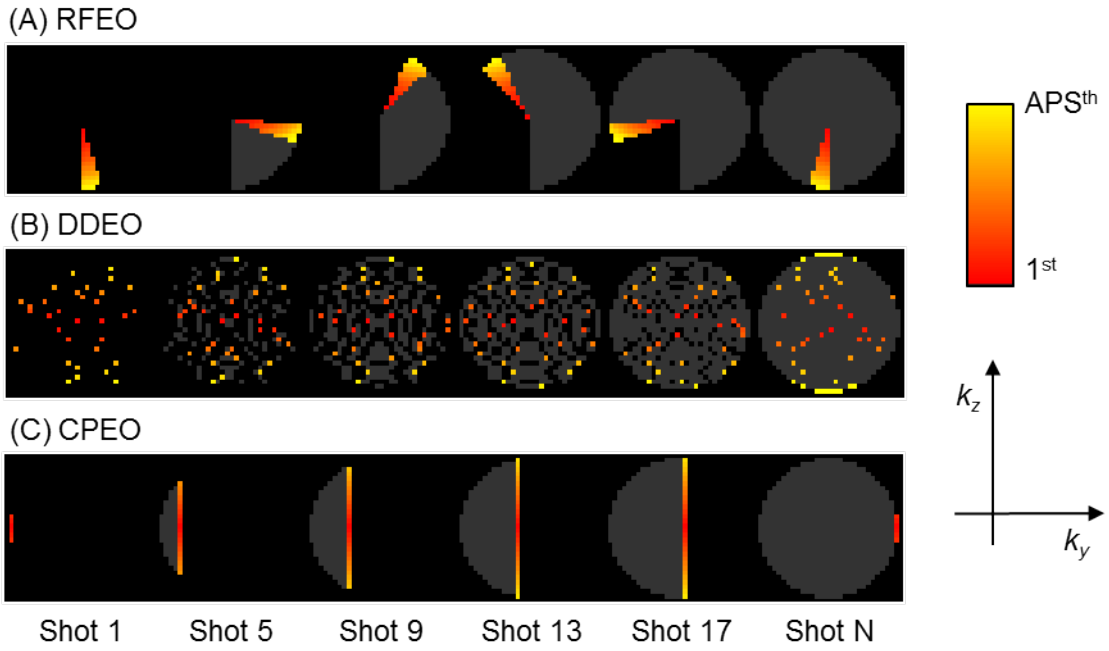

Figure 7.2 Example of three different *k*-space orderings using a matrix of 32×32. The colour bar shows the acquisition order within each of the shot: from the 1st point to the APSth point; APS = 32 is used in this example.

Three different *k*-space view orders were implemented and compared. The first method was Radial Fan-beam Encoding Ordering (RFEO) [254] (Figure 7.2A). In this method, the *k*-space points in the k_y-k_z plane were first sorted into different shots by their polar angle, and then within each shot, the points were sorted by their distance from the *k*-space centre. The second method was the Distance-Determined Encoding Ordering [255] (DDEO, Figure 7.2B). In this method, all the *k*-space points in the k_y-k_z plane were first sorted by their distance from the *k*-space centre, and then the ith × N points were allocated to the ith place in each shot (i is from 1 to the APS, N is the total number of shots). The third method was Centric Phase Encoding Order (CPEO, Figure 7.2C), in which each shot consists of a single line along k_z.

The other fixed parameters for the acquisition were: Td = 200 ms; TE = 4.9, 10.4, 15.7, 21.1, 26.4 and 31.8 ms; TR = 36.8 ms; flip angle = 15°; receiver bandwidth = ±31.25 kHz; acquisition plane: axial; field-of-view (FOV): 140×140×80 mm^3; acquisition matrix: 224×224×40. The images were interpolated to a 512×512×80 reconstructed matrix size using zero-filling. A unipolar echo acquisition was used to minimise off-resonance effects. The author implemented both iMSDE and DANTE preparation into the ME-FSPGR sequence used in this study.

Bloch simulation

Bloch equation simulations were performed to study the signal evolution of the vessel wall with the different black-blood methods and *k*-space view orderings, using the Bloch simulation algorithm mentioned in Chapter 2 from Brian Hargreaves at Stanford University, in Matlab (MathWorks, Natick, MA, USA). The relaxation times used in the simulation were: T_1_blood = 1500 ms, T_2_blood = 128 ms, T_1_wall = 1000 ms and T_2_wall = 50 ms [102, 144]. Other parameters were the same as for the volunteer protocol.

Volunteer studies

Fourteen volunteers (seven male, mean age 30.9, range: 24-41 years) were recruited for this study. The study protocol was reviewed and approved by a local ethics committee and written informed consent was obtained from each volunteer (R&D number: A091374). All scans were performed using a 1.5 T system (MR450w, GE Healthcare, Waukesha, WI), using a 4-channel phased-array neck coil (PACC, MachNet, Roden, The Netherlands).

The volunteers were initially scanned with the ME-FSPGR sequence combined with i) DANTE, ii) iMSDE, and iii) without black-blood preparation. The readouts used the RFEO method with a fixed APS of 40. The three different view orders were evaluated using the DANTE preparation with an APS of 40 for all of the volunteers. The scanning time for the RFEO and DDEO acquisitions was 6 min 15 s, and 7 minutes for CPEO. To further optimise the blood suppression, seven volunteers were scanned with the DANTE preparation and RFEO order using different APS (APS = 10, 40, 70 and 100).

In the R_2* calculation, Miller's method [112] described in Chapter 2 is used.

Image analysis

In all the volunteer images, the lumen and wall contours of three contiguous slices 5 mm below the bifurcation were manually drawn by an experienced reviewer in OsiriX (OsiriX 5.5.2, Pixmeo, Geneva, Switzerland). Vessel wall SNR and wall-lumen CNR were calculated. The SNR of a single region drawn in the sternocleidomastoid muscle was also calculated for each scan. The data are presented as mean ± sd (standard deviation). A paired student's t-test was used to compare the difference. The statistical analysis was performed using R [256] (version 3.2.2, R Development Core Team, Vienna, Austria).

7.3 Results

To achieve adequate blood suppression, the iMSDE preparation was empirically optimised with a gradient amplitude of 20 mT/m, duration of 1500 ms and slew rate of 120 mT/m/ms. The DANTE parameters were set at: number of pulses 100, gradient amplitude 20 mT/m, flip angle 13˚, repetition time ~1 ms.

Figure 7.3 shows the Bloch simulation of the vessel wall longitudinal magnetisation change over time and one corresponding volunteer image using RFEO with an APS of 40. The DANTE prepared sequence achieves a higher signal compared to the iMSDE prepared version. In the volunteer scans, the vessel wall SNR and CNR are significantly higher in DANTE than iMSDE (SNR: 12.7 ± 3.2 vs. 8.7 ± 1.4, $p < 0.01$; CNR: 7.0 ± 1.8 vs. 5.1 ± 1.1, $p < 0.01$). The R_2* values of the vessel wall were similar (DANTE vs. iMSDE: 35.8 ± 13.3 vs. 35.0 ± 7.0 s^{-1}, $p = 0.84$). The muscle R_2* values were unaffected by the blood suppression schemes (no blood suppression: 34.9 ± 5.0 s^{-1}, DANTE: 35.8 ± 4.6 s^{-1}, iMSDE: 37.3 ± 7.7 s^{-1}, $p > 0.05$).

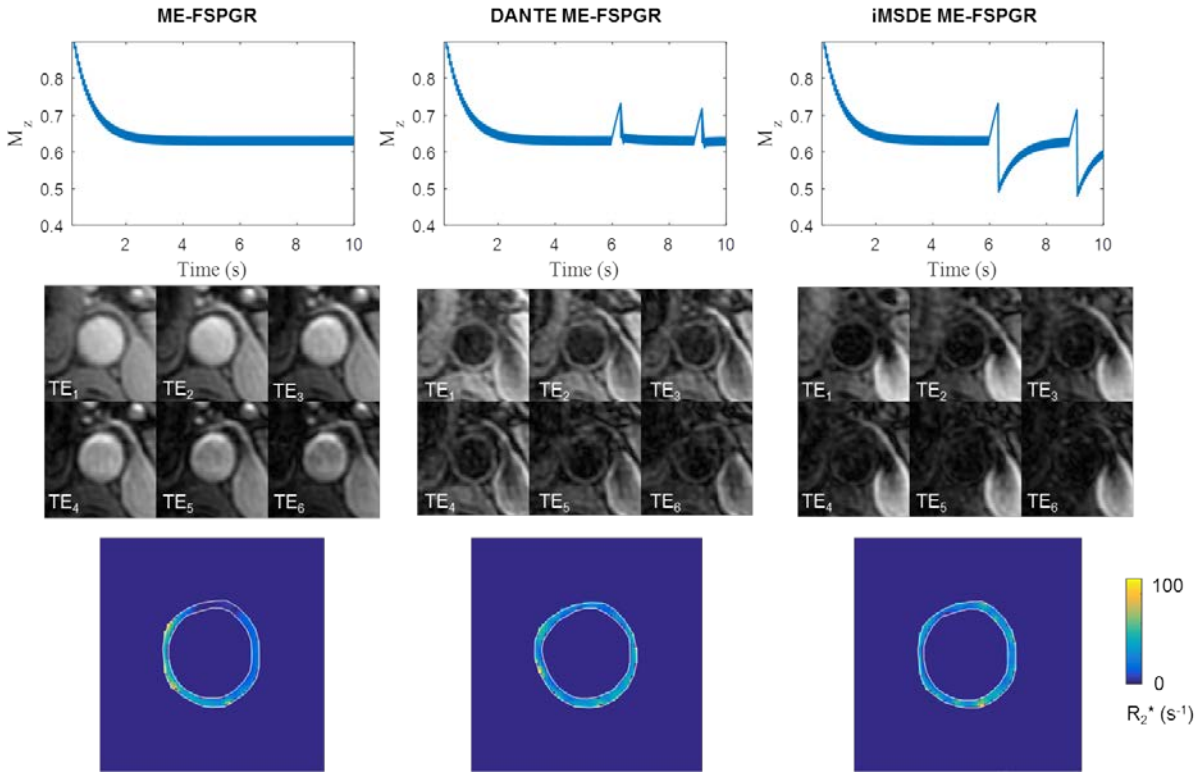

Figure 7.3 Upper row: Bloch simulation of the ME-FSPGR sequence, and with DANTE or iMSDE preparation. Vessel wall material properties of T_1 = 1000 ms and T_2 = 50 ms are used in the simulation. Centre row: corresponding volunteer images with six echoes acquired. Bottom row: corresponding R_2* maps of the vessel wall.

Figure 7.4 shows the Bloch simulation of the longitudinal magnetisation recovery of blood using the different *k*-space view orders. After each black-blood pulse, the blood longitudinal magnetisation recovers from zero due to T_1 relaxation. Since the image contrast is mainly determined by the *k*-space centre, a method that allocates the low blood signal points to the *k*-space centre can achieve optimal blood suppression. Under this assumption, the DDEO method (centre column) should achieve the best blood suppression.

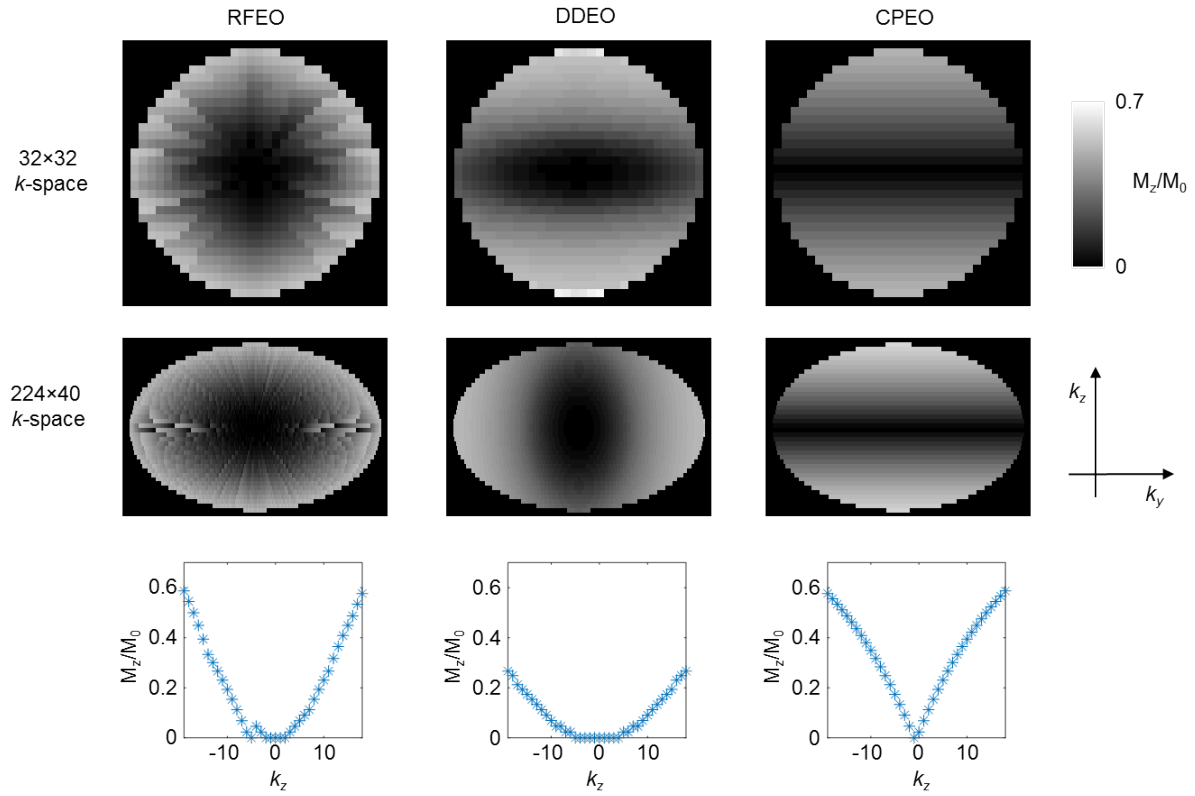

Figure 7.4 Blood T_1 recovery in *k*-space using three different *k*-space view orderings. The upper row shows an example of 32×32 *k*-space using APS equals to 32. Centre row shows the example of 224×40 *k*-space using APS equals to 40. The bottom row shows the one line of *k*-space (k_y = 0) in 224×40 matrix example.

Figure 7.5 shows a volunteer study acquired using the DANTE prepared sequence with the three different *k*-space orders. These T_2*w images are obtained using a sum-of-squares combination of the different echoes. The RFEO and DDEO orders achieved better blood suppression than the CPEO order. The results show that volunteer wall-lumen CNR of RFEO (7.0 ± 1.8) and DDEO (6.7 ± 2.0) are comparable, and higher than the CPEO method (6.1 ± 2.2). However, none of the differences was significant ($p > 0.05$).

Figure 7.5 An example of volunteer image using three different *k*-space view ordering. The sum-of-squares of echoes is presented.

Some of the volunteer images showed insufficient blood suppression with the use of APS = 40. Thus, the effectiveness of changing the APS on blood suppression was further investigated in seven volunteers. One example of a volunteer study with different APS is shown in Figure 7.6. The results show that the SNR and R_2* value measured from the vessel wall and the sternocleidomastoid muscle were similar with different APS, while the CNR of the vessel wall decreases with increasing APS, indicating the blood suppression efficiency decreases with increasing APS.

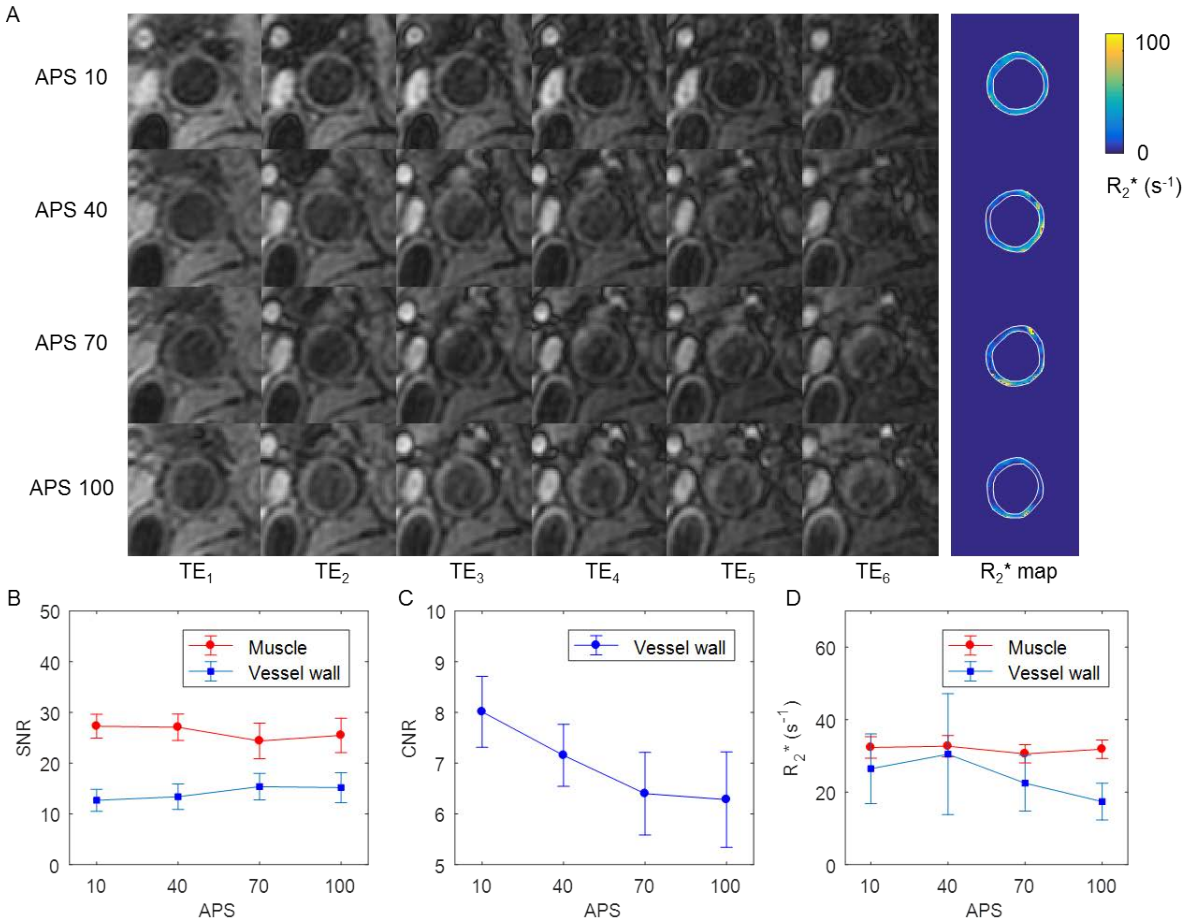

Figure 7.6 Comparison of different APS using DANTE prepared acquisition. (A): A volunteer image showing different APS. The six different echoes and R_2* map is presented. Large APS results in insufficient blood suppression. (B-D): Measurement of SNR, CNR and R_2* of the vessel wall and sternocleidomastoid muscle.

7.4 Discussion

Vessel wall multi-echo T_2* imaging could be used for plaque component classification [102, 257], USPIO uptake quantification [238, 245, 246, 248, 258-260] and potentially also for susceptibility weighted imaging (SWI) [261, 262] and quantitative susceptibility mapping (QSM) [263]. Unlike 3D FSE based T_2 mapping sequences [158, 159, 264, 265], in which the readout has an intrinsic blood suppression effect, the blood suppression for GRE-based T_2* mapping is challenging. So far only limited studies have explored black-blood T_2* mapping. This study, for the first time, shows the feasibility of implementing black-blood techniques into a 3D T_2*/R_2* mapping sequence.

The iMSDE preparation demonstrated a lower SNR compared to DANTE in this study, which is in agreement with a previous study [144]. The T_2 decay during the iMSDE preparation

leads to lower image SNR, which may limit the application in some low-signal regions [251]. When applied to high field MRI (e.g., 7T), DANTE may also be more suitable due to the specific absorption rate (SAR) restrictions [144, 266].

Three different *k*-space filling orders were implemented and compared. There was no difference between the RFEO and DDEO orders, in that they both showed better blood suppression than CPEO. Both RFEO and DDEO fill the *k*-space centre immediately after the blood suppression pulse. Therefore, the reconstructed images have the most effective blood suppression. The results showed non-significant differences between these three methods, indicating that the choice of view-ordering does not a major influence on image quality. The choice of the APS, on the other hand, is more important for blood suppression. Larger APS values allow longer blood T_1 recovery between the blood suppression pulses, which will result in insufficient blood suppression. The RFEO and DDEO provide flexible APS during the scan while the CPEO has limited options for APS (APS must be fractions of slice number, e.g., 1, 1/2, 1/3 et al of slice number). The DDEO method may be more suitable when the APS is very short; in this case the RFEO method may not be optimal as the outer *k*-space regions cannot be reached even with a small polar angle. The large jumps in the *k*-space ordering utilised in the DDEO method may increase eddy current effects, as, has been previously reported albeit using balanced steady-state free precession (SSFP) sequence [267, 268]. However, no such eddy current artefact was observed in this study.

It should be noted that cardiac gating was not used in this study. The addition of ECG gating would result in variable Td values and hence variable magnetisation recovery between different the shots. Furthermore, a previous study showed that comparable vessel wall morphological measurement can be achieved with a ungated 3D sequence [269].

7.5 Conclusion

This study has developed and optimised a 3D black-blood R_2^* mapping sequence through Bloch simulation and volunteer imaging. The results show that the DANTE preparation is better than iMSDE in terms of image SNR. In addition the RFEO and DDEO *k*-space ordering methods have similar blood suppression efficiency, and are both better than the CPEO method. Smaller APS could achieve better blood suppression effect.

The results prove the specific hypotheses investigated in this chapter that *[Hypothesis 9]* the blood suppression techniques do not influence the measurement of R_2* values in the carotid

vessel wall and *[Hypothesis 10]* optimal blood suppression, *k*-space view ordering and short acquisitions-per-short could achieve good black-blood vessel wall R_2* mapping.

Chapter 8 Summary and further developments

The general aim of this dissertation is to evaluate several quantitative MRI methods for quantifying different biomarkers in carotid vessel wall imaging. The main hypothesis investigated in this thesis is: Can quantitative MRI methods be used to acquire objective biomarkers of carotid vessel wall and atherosclerotic plaque with high accuracy and good repeatability?

Traditional multi-contrast carotid protocol demonstrates high accuracy in differentiating plaque component, with histology as the gold standard. However the sequences and parameters used in these studies are not identical. These make it difficult to harmonise the results from multi-centre trials. Quantitative MRI on the other hand, could overcome these limitations and provide standardised analysis for the carotid plaques independent of scanners and locations. The use of quantitative MRI would be more suitable for longitudinal studies such as monitoring the disease progression or studying a certain drug therapy.

The 4D high temporal and spatial resolution sequence used in Chapter 3 demonstrates the ability to obtain carotid plaque perfusion and surface morphological information simultaneously. This allows fast and reproducible vessel wall functional and morphological analysis. Current limitations of this method include an anisotropic resolution and limited temporal resolution. Future improvement could improve both these aspects of the acquisition through the use of compressd sensing mentioned in Chapter 4 and 5. The full imaging protocol applied in the 21 patients normally exceeds 45 mins which is relatively long. Techniques such as DIfferential Subsampling with Cartesian Ordering (DISCO) [270] or recently introduced compressed sensing in dynamic imaging [271] could be investigated to improve the images quality, or reduce the acquisition time while maintaining the similar image quality.

Currently there are several groups worldwide performing carotid imaging, however the sequences they are using are different. Some groups use FSE/TSE (Turbo Spin Echo) based sequences [272], and others are using GRE based sequences [204, 273]. This makes it difficult to compare the images from different groups. The quantitative sequences, such as T_2 mapping, are also different between the groups. For this reason, Chapter 4 was designed to compare different T_2 mapping sequences in the application of carotid wall. The results

showed that the vessel wall T_2 values are significantly different in the volunteers' scans using different sequences, though the phantom scans showed accurate measurement. The scan efficiency and SNR are much higher when using 3D sequences compared to 2D sequences. The FSE readout has higher image SNR and lower CoV in T_2 maps than GRE readout. This indicates careful analysis of the signal evolution and choice of sequences are important factors for accurate T_2 measurement in the carotid vessel wall. A similar methodology could be applied to other vessel wall areas such as middle cerebral artery (MCA) and abdominal aorta. When applied to abdominal imaging, the current 3D sequences need to be combined with respiratory gating, this will increase scanning time and potentially reduce the image quality. The long scanning time used in this work (above 8 mins) is still too long for the patient scan [180]. Therefore Chapter 5 was designed to combine a recent technique, compressed sensing, to reduce the scanning time.

Chapter 5 demonstrated the compressed sensing (CS) and parallel imaging (PI) can be used together to reduce the acquisition time of the 3D FSE sequence. The joint acceleration showed better image quality than when a single technique was used [274]. In under 8 minutes simultaneous PDw, T_2w and T_2 mapping were acquired. Therefore, this sequence can be used for both quantitative and multi-contrast imaging. There is further work that needs to be done to optimise this sequence. For instance, the small slice number (40 slices) and a fixed fully sampled *k*-space centre (32×32 in k_y×k_z) limits the use of a higher CS factor. When compared to other carotid CS studies [164, 190], the CS factor in this study is relatively low (up to 2). Future work could explore increasing slice number and optimise both fully sampled *k*-space centre size and CS factor to further improve the scan efficiency of the 3D T_2 mapping sequence. Also, this sequence could be combined with reduced-field of view to increase the resolution and reduce the scanning time as well [275], although at the expenses of a reduction in SNR.

Chapter 6 applied the CS and PI techniques to the current multi-contrast protocol and demonstrated good scan-rescan and inter/intra-observer repeatability in volunteer and patient scan. As CS has only been introduced into MRI in recent years, this is the first work that validates the use of CS in a multi-contrast protocol in a clinical study. Similar to Chapter 5, one of the limitations of this work is the fixed fully sampled *k*-space centre and the small number of slices used, which prevent the use of high CS factor (up to 2 in this study). Thus, a more comprehensive analysis is necessary to investigate these factors jointly, including the reconstruction time, to find an optimal protocol.

The optimised black-blood 3D R_2* sequence described in Chapter 7 showed comparable R_2* measurement with non-blood suppressed sequence in the healthy volunteers. The sequence could be used to differentiate plaque components [102] and can also applied to studies using USPIOs. The use of USPIOs could help identify plaques inflammation [102, 276]. Currently the majority of these kind of studies are performed in 2D [249, 277]. The proposed 3D sequence could allow whole plaque coverage and allow the images to be reformatted into any plane. The obtained data from this sequence could also have other application as well. For example, the phase information could be used for susceptibility weighted imaging (SWI) [278] or quantitative susceptibility mapping (QSM) [279].

The sequences, post-processing algorithm, and methodology described in this thesis could be applied to other vessel wall imaging area as well, such as middle cerebral artery, abdominal aorta, and peripheral arteries. Figure 8.1 shows an example of 3D iMSDE FSE based T_2 mapping sequence applied in the MCA of a healthy volunteer.

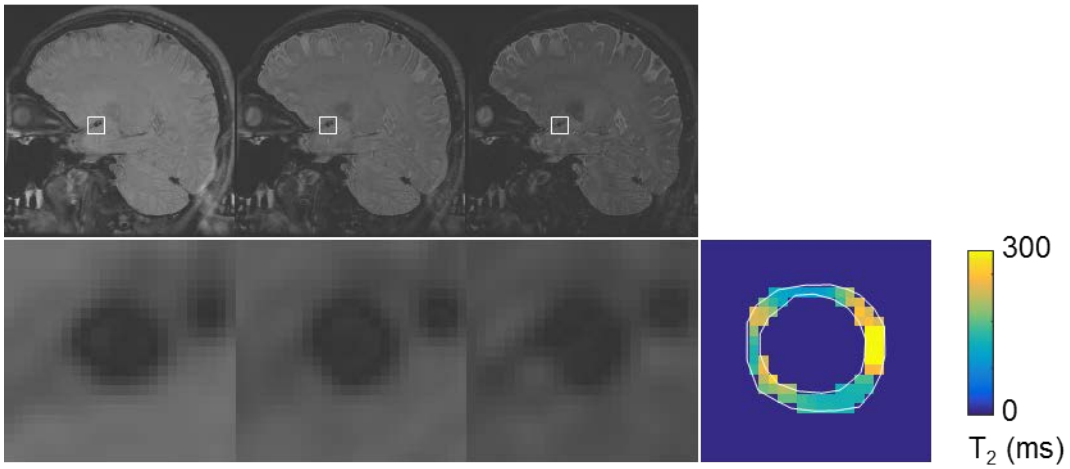

Figure 8.1 3D iMSDE FSE based T_2 mapping sequence applied to middle cerebral artery. The images were acquired by the author using the sequence developed in Chapter 4.

As the traditional quantitative imaging methods used in this thesis usually take much longer than contrast weighted images, the sequences need to be repeated several times with one specific parameter varied while others are kept constant. To overcome the drawbacks of traditional quantitative imaging methods, there are also other quantitative mapping techniques that have been developed in recent years, such as synthetic MRI [280] and magnetic resonance fingerprinting (MRF) [281].

Synthetic MRI uses a single sequence with a multi-slice, multi-echo and multi-delay acquisition to simultaneously obtain PD, T_1 and T_2 relaxation time data, which could be used

to synthesis conventional image weightings such as T_1w, T_2w, PDw T_1/T_2 FLAIR (FLuid AttenuatedInversion REcovery) and STIR (Short TI Inversion Recovery).

MRF was introduced in 2013 to provide simultaneous measurement of multiple parameters such as relative spin density, T_1, T_2, B_0 map and et al., using a single time-efficient acquisition [281]. The MRF technique uses a varying flip angle and TR throughout the acquisition. Each type of tissue with a typical T_1, T_2 and PD property shows a unique signal evaluation in the sequence (fingerprints) which can be used to recognize in the post-processing. Figure 8.2 shows an example of T_1, T_2 and PD maps from MRF compared with the T_2 mapping result from Chapter 4 in a healthy volunteer scan at 3 T. This sequence was an early version of MRF developed in GE environment with spiral readout. The FOV was fixed to 180×180 mm^2 with the in-plane resolution of 0.7×0.7 mm^2. Future work could compare these techniques with the 'traditional quantitative methods' demonstrate in the thesis.

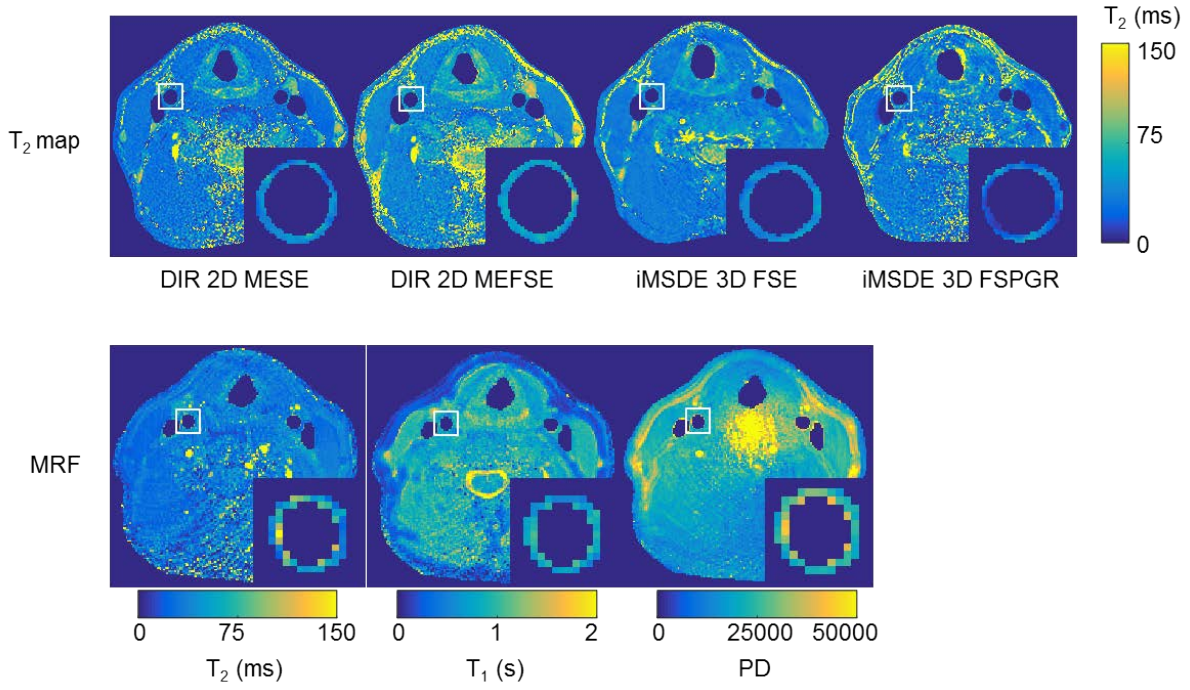

Figure 8.2 First row: T_2 mapping from the four sequences discussed in Chapter 4. Second row: MR fingerprinting and the T_2, T_1 and PD maps. The MRF images were acquired by the author with the help of Dr Joshua Kaggie.

In conclusion, the quantitative MRI methods used in the thesis have been proven to be accurate and repeatable techniques to quantify carotid vessel wall biomarkers. Future work needs to explore the association of these quantitative biomarkers with the development, procession and severity of the carotid atherosclerotic disease.

Bibliography

1. Yuan, J., A. Usman, T. Das, A. Patterson, J. Gillard, and M. Graves, *Imaging Carotid Atherosclerosis Plaque Ulceration: Comparison of Advanced Imaging Modalities and Recent Developments.* American Journal of Neuroradiology, 2017. **38**(4): p. 664-671.
2. Hankey, G.J., *Stroke: how large a public health problem, and how can the neurologist help?* Archives of neurology, 1999. **56**(6): p. 748-754.
3. Saka, Ö., A. McGuire, and C. Wolfe, *Cost of stroke in the United Kingdom.* Age and ageing, 2009. **38**(1): p. 27-32.
4. Shi, F., R.G. Hart, D.G. Sherman, and C.H. Tegeler, *Stroke in the People's Republic of China.* Stroke, 1989. **20**(11): p. 1581-1585.
5. Thrift, A.G., H.M. Dewey, R.A. Macdonell, J.J. McNeil, and G.A. Donnan, *Incidence of the major stroke subtypes initial findings from the North East Melbourne Stroke Incidence Study (NEMESIS).* Stroke, 2001. **32**(8): p. 1732-1738.
6. Web. Available from: http://vpdiagnostics.com. 11/05/2017.
7. Carr, S., A. Farb, W.H. Pearce, R. Virmani, and J.S. Yao, *Atherosclerotic plaque rupture in symptomatic carotid artery stenosis.* Journal of vascular surgery, 1996. **23**(5): p. 755-766.
8. Shattock, S., *A report upon the pathological condition of the aorta of King Menephtah, traditionally regarded as the Pharaoh of the Exodus.* Proceedings of the Royal Society of Medicine, 1909. **2**(Pathol Sect): p. 122.
9. Insull Jr, W., *The pathology of atherosclerosis: plaque development and plaque responses to medical treatment.* The American journal of medicine, 2009. **122**(1): p. S3-S14.
10. Gillard, J., M. Graves, and T. Hatsukami, *Carotid disease: the role of imaging in diagnosis and management*. 2006: Cambridge University Press.
11. Libby, P., P.M. Ridker, and G.K. Hansson, *Progress and challenges in translating the biology of atherosclerosis.* Nature, 2011. **473**(7347): p. 317-325.
12. Moore, W.S., H. Barnett, H.G. Beebe, E.F. Bernstein, B.J. Brener, T. Brott, et al., *Guidelines for carotid endarterectomy a multidisciplinary consensus statement from the Ad Hoc Committee, American Heart Association.* Stroke, 1995. **26**(1): p. 188-201.
13. Njemanze, P., O. Beck, C. Gomez, S. Horenstein, B. Cujec, P. Polasek, et al., *North American Symptomatic Carotid Endarterectomy Trial. Methods, patient characteristics, and progress.* Stroke, 1991. **22**: p. 711-20.
14. Barnett, H.J., D.W. Taylor, M. Eliasziw, A.J. Fox, G.G. Ferguson, R.B. Haynes, et al., *Benefit of carotid endarterectomy in patients with symptomatic moderate or severe stenosis.* New England Journal of Medicine, 1998. **339**(20): p. 1415-1425.

15. Barnett, H.J., H.E. Meldrum, and M. Eliasziw, *The appropriate use of carotid endarterectomy.* Canadian Medical Association Journal, 2002. **166**(9): p. 1169-1179.

16. Rothwell, P., S. Gutnikov, and C. Warlow, *Reanalysis of the final results of the European Carotid Surgery Trial.* Stroke, 2003. **34**(2): p. 514-523.

17. Farrell, B., A. Fraser, P. Sandercock, J. Slattery, and C. Warlow, *Randomised trial of endarterectomy for recently symptomatic carotid stenosis: final results of the MRC European Carotid Surgery Trial (ECST).* Lancet, 1998. **351**(9113): p. 1379-1387.

18. Staikov, I.N., K. Nedeltchev, M. Arnold, L. Remonda, G. Schroth, M. Sturzenegger, et al., *Duplex sonographic criteria for measuring carotid stenoses.* Journal of clinical ultrasound, 2002. **30**(5): p. 275-281.

19. Grant, E.G., A.J. Duerinckx, S.M. El Saden, M.L. Melany, G.M. Hathout, P.T. Zimmerman, et al., *Ability to Use Duplex US to Quantify Internal Carotid Arterial Stenoses: Fact or Fiction? 1.* Radiology, 2000. **214**(1): p. 247-252.

20. Wasserman, B.A., R.J. Wityk, H.H. Trout, and R. Virmani, *Low-grade carotid stenosis looking beyond the lumen with MRI.* Stroke, 2005. **36**(11): p. 2504-2513.

21. Glagov, S., E. Weisenberg, C.K. Zarins, R. Stankunavicius, and G.J. Kolettis, *Compensatory enlargement of human atherosclerotic coronary arteries.* New England Journal of Medicine, 1987. **316**(22): p. 1371-1375.

22. Fishbein, M.C. and R.J. Siegel, *How big are coronary atherosclerotic plaques that rupture?* Circulation, 1996. **94**(10): p. 2662-2666.

23. Redgrave, J.N., P. Gallagher, J.K. Lovett, and P.M. Rothwell, *Critical Cap Thickness and Rupture in Symptomatic Carotid Plaques The Oxford Plaque Study.* Stroke, 2008. **39**(6): p. 1722-1729.

24. Bassiouny, H.S., Y. Sakaguchi, S.A. Mikucki, J.F. McKinsey, G. Piano, B.L. Gewertz, et al., *Juxtalumenal location of plaque necrosis and neoformation in symptomatic carotid stenosis.* Journal of vascular surgery, 1997. **26**(4): p. 585-594.

25. Teng, Z., U. Sadat, A.J. Brown, and J.H. Gillard, *Plaque hemorrhage in carotid artery disease: Pathogenesis, clinical and biomechanical considerations.* Journal of biomechanics, 2014. **47**(4): p. 847-858.

26. Moreno, P.R., R.A. Lodder, K.R. Purushothaman, W.E. Charash, W.N. O'Connor, and J.E. Muller, *Detection of lipid pool, thin fibrous cap, and inflammatory cells in human aortic atherosclerotic plaques by near-infrared spectroscopy.* Circulation, 2002. **105**(8): p. 923-927.

27. Miskolczi, L., L.R. Guterman, J.D. Flaherty, and L.N. Hopkins, *Depiction of carotid plaque ulceration and other plaque-related disorders by intravascular sonography: a flow chamber study.* AJNR Am J Neuroradiol, 1996. **17**(10): p. 1881-90.

28. Stary, H.C., A.B. Chandler, R.E. Dinsmore, V. Fuster, S. Glagov, W. Insull, et al., *A definition of advanced types of atherosclerotic lesions and a histological classification of atherosclerosis A report from the Committee on Vascular Lesions of the Council on Arteriosclerosis, American Heart Association.* Circulation, 1995. **92**(5): p. 1355-1374.

29. Sitzer, M., W. Müller, M. Siebler, W. Hort, H.-W. Kniemeyer, L. Jäncke, et al., *Plaque ulceration and lumen thrombus are the main sources of cerebral microemboli in high-grade internal carotid artery stenosis.* Stroke, 1995. **26**(7): p. 1231-1233.

30. Eliasziw, M., J.Y. Streifler, A.J. Fox, V.C. Hachinski, G.G. Ferguson, and H. Barnett, *Significance of plaque ulceration in symptomatic patients with high-grade carotid stenosis. North American Symptomatic Carotid Endarterectomy Trial.* Stroke, 1994. **25**(2): p. 304-308.

31. Handa, N., M. Matsumoto, H. Maeda, H. Hougaku, and T. Kamada, *Ischemic stroke events and carotid atherosclerosis results of the Osaka follow-up study for ultrasonographic assessment of carotid atherosclerosis (the OSACA Study).* Stroke, 1995. **26**(10): p. 1781-1786.

32. Rothwell, P.M., R. Gibson, and C. Warlow, *Interrelation between plaque surface morphology and degree of stenosis on carotid angiograms and the risk of ischemic stroke in patients with symptomatic carotid stenosis.* Stroke, 2000. **31**(3): p. 615-621.

33. Rothwell, P., R. Villagra, R. Gibson, R. Donders, and C. Warlow, *Evidence of a chronic systemic cause of instability of atherosclerotic plaques.* The Lancet, 2000. **355**(9197): p. 19-24.

34. Rothwell, P.M., Z. Mehta, S.C. Howard, S.A. Gutnikov, and C.P. Warlow, *From subgroups to individuals: general principles and the example of carotid endarterectomy.* The Lancet, 2005. **365**(9455): p. 256-265.

35. Prabhakaran, S., T. Rundek, R. Ramas, M.S. Elkind, M.C. Paik, B. Boden-Albala, et al., *Carotid plaque surface irregularity predicts ischemic stroke the northern manhattan study.* Stroke, 2006. **37**(11): p. 2696-2701.

36. Sadat, U., Z. Teng, V. Young, S. Walsh, Z. Li, M. Graves, et al., *Association between biomechanical structural stresses of atherosclerotic carotid plaques and subsequent ischaemic cerebrovascular events–a longitudinal in vivo magnetic resonance imaging-based finite element study.* European Journal of Vascular and Endovascular Surgery, 2010. **40**(4): p. 485-491.

37. Yuan, C., K.W. Beach, L.H. Smith, and T.S. Hatsukami, *Measurement of atherosclerotic carotid plaque size in vivo using high resolution magnetic resonance imaging.* Circulation, 1998. **98**(24): p. 2666-2671.

38. den Hartog, A., S. Bovens, W. Koning, J. Hendrikse, P. Luijten, F. Moll, et al., *Current status of clinical magnetic resonance imaging for plaque characterisation in patients with*

carotid artery stenosis. European Journal of Vascular and Endovascular Surgery, 2013. **45**(1): p. 7-21.

39. Chu, B., A. Kampschulte, M.S. Ferguson, W.S. Kerwin, V.L. Yarnykh, K.D. O'Brien, et al., *Hemorrhage in the atherosclerotic carotid plaque: a high-resolution MRI study.* Stroke, 2004. **35**(5): p. 1079-1084.

40. Yuan, C., W.S. Kerwin, M.S. Ferguson, N. Polissar, S. Zhang, J. Cai, et al., *Contrast‐enhanced high resolution MRI for atherosclerotic carotid artery tissue characterization.* Journal of Magnetic Resonance Imaging, 2002. **15**(1): p. 62-67.

41. Lovett, J., P. Gallagher, L. Hands, J. Walton, and P. Rothwell, *Histological correlates of carotid plaque surface morphology on lumen contrast imaging.* Circulation, 2004. **110**(15): p. 2190-2197.

42. Hessel, S.J., D.F. Adams, and H.L. Abrams, *Complications of angiography.* Radiology, 1981. **138**(2): p. 273-281.

43. Walker, M.D., J.R. Marler, M. Goldstein, P.A. Grady, J.F. Toole, W.H. Baker, et al., *Endarterectomy for asymptomatic carotid artery stenosis.* JAMA, 1995. **273**(18): p. 1421-1428.

44. Edwards, J.H., I.I. Kricheff, T. Rites, and A. Imparato, *Angiographically Undetected Ulceration of the Carotid Bifurcation as a Cause of Embolic Stroke 1.* Radiology, 1979. **132**(2): p. 369-373.

45. Streifler, J.Y., M. Eliasziw, A.J. Fox, O.R. Benavente, V.C. Hachinski, G.G. Ferguson, et al., *Angiographic detection of carotid plaque ulceration. Comparison with surgical observations in a multicenter study. North American Symptomatic Carotid Endarterectomy Trial.* Stroke, 1994. **25**(6): p. 1130-1132.

46. Gandhi, D., *Computed tomography and magnetic resonance angiography in cervicocranial vascular disease.* Journal of Neuro-Ophthalmology, 2004. **24**(4): p. 306-314.

47. Ho, V.B. and T.K. Foo, *Optimization of Gadolinium-Enhanced Magnetic Resonance Angiography Using an Automated Bolus-Detection Algorithm (MR SmartPrep) y.* Investigative radiology, 1998. **33**(9): p. 515-523.

48. Barnes, R., G. Bone, J. Reinertson, E. Slaymaker, D. Hokanson, and D. Strandness Jr, *Noninvasive ultrasonic carotid angiography: prospective validation by contrast arteriography.* Surgery, 1976. **80**(3): p. 328-335.

49. Reilly, L.M., R.J. Lusby, L. Hughes, L.D. Ferrell, R.J. Stoney, and W.K. Ehrenfeld, *Carotid plaque histology using real-time ultrasonography: clinical and therapeutic implications.* The American journal of surgery, 1983. **146**(2): p. 188-193.

50. Park, T.H., *Evaluation of Carotid Plaque Using Ultrasound Imaging.* Journal of Cardiovascular Ultrasound, 2016. **24**(2): p. 91-95.

51. Dósa, E., K. Hirschberg, A. Apor, Z. Járányi, L. Entz, G. Acsády, et al., *Echolucent or predominantly echolucent femoral plaques predict early restenosis after eversion carotid endarterectomy.* Journal of vascular surgery, 2010. **51**(2): p. 345-350.

52. Mitchell, D.G., *Color Doppler imaging: principles, limitations, and artifacts.* Radiology, 1990. **177**(1): p. 1-10.

53. O'Donnell, T.F., L. Erdoes, W.C. Mackey, J. McCullough, A. Shepard, P. Heggerick, et al., *Correlation of B-mode ultrasound imaging and arteriography with pathologic findings at carotid endarterectomy.* Archives of surgery, 1985. **120**(4): p. 443-449.

54. O'Leary, D., J. Holen, J. Ricotta, S. Roe, and E. Schenk, *Carotid bifurcation disease: prediction of ulceration with B-mode US.* Radiology, 1987. **162**(2): p. 523-525.

55. Comerota, A.J., M.L. Katz, J.V. White, and J.D. Grosh, *The preoperative diagnosis of the ulcerated carotid atheroma.* Journal of vascular surgery, 1990. **11**(4): p. 505-510.

56. Sitzer, M., W. Müller, J. Rademacher, M. Siebler, W. Hort, H.-W. Kniemeyer, et al., *Color-flow Doppler-assisted duplex imaging fails to detect ulceration in high-grade internal carotid artery stenosis.* Journal of vascular surgery, 1996. **23**(3): p. 461-465.

57. De Bray, J., J. Baud, and M. Dauzat, *Consensus concerning the morphology and the risk of carotid plaques.* Cerebrovascular Diseases, 1997. **7**(5): p. 289-296.

58. Hennerici, M., H. Baezner, and M. Daffertshofer, *Ultrasound and arterial wall disease.* Cerebrovascular Diseases, 2004. **17**(Suppl. 1): p. 19-33.

59. Anderson, D.C., R. Loewenson, D. Yock, R. Farber, D. Larson, and M. Bromer, *B-mode, real-time carotid ultrasonic imaging: correlation with angiography.* Archives of neurology, 1983. **40**(8): p. 484-488.

60. O'Leary, D., F. Bryan, M. Goodison, M. Rifkin, R. Gramiak, M. Ball, et al., *Measurement variability of carotid atherosclerosis: real-time (B-mode) ultrasonography and angiography.* Stroke, 1987. **18**(6): p. 1011-1017.

61. Heliopoulos, J., K. Vadikolias, C. Piperidou, and P. Mitsias, *Detection of Carotid Artery Plaque Ulceration Using 3‐Dimensional Ultrasound.* Journal of Neuroimaging, 2011. **21**(2): p. 126-131.

62. Saba, L., G. Caddeo, R. Sanfilippo, R. Montisci, and G. Mallarini, *CT and ultrasound in the study of ulcerated carotid plaque compared with surgical results: potentialities and advantages of multidetector row CT angiography.* American journal of neuroradiology, 2007. **28**(6): p. 1061-1066.

63. Schminke, U., L. Motsch, L. Hilker, and C. Kessler, *Three-dimensional ultrasound observation of carotid artery plaque ulceration.* Stroke, 2000. **31**(7): p. 1651-1655.

64. Yao, J., M.R. van Sambeek, A. Dall'Agata, L.C. van Dijk, M. Kozakova, P.J. Koudstaal, et al., *Three-dimensional ultrasound study of carotid arteries before and after endarterectomy.* Stroke, 1998. **29**(10): p. 2026-2031.

65. Griewing, B., U. Schminke, C. Morgenstern, M.L. Walker, and C. Kessler, *Three‐dimensional Ultrasound Angiography (Power Mode) for the Quantification of Carotid Artery Atherosclerosis.* Journal of Neuroimaging, 1997. **7**(1): p. 40-45.

66. Walker, L.J., A. Ismail, W. McMeekin, D. Lambert, A.D. Mendelow, and D. Birchall, *Computed tomography angiography for the evaluation of carotid atherosclerotic plaque.* Stroke, 2002. **33**(4): p. 977-981.

67. Wintermark, M., S.S. Jawadi, J.H. Rapp, T. Tihan, E. Tong, D. Glidden, et al., *High-resolution CT imaging of carotid artery atherosclerotic plaques.* American Journal of Neuroradiology, 2008. **29**(5): p. 875-882.

68. Saba, L., G. Caddeo, R. Sanfilippo, R. Montisci, and G. Mallarini, *Efficacy and sensitivity of axial scans and different reconstruction methods in the study of the ulcerated carotid plaque using multidetector-row CT angiography: comparison with surgical results.* American journal of neuroradiology, 2007. **28**(4): p. 716-723.

69. Link, J., J. Brossmann, M. Grabener, S. Mueller-Huelsbeck, J.C. Steffens, G. Brinkmann, et al., *Spiral CT angiography and selective digital subtraction angiography of internal carotid artery stenosis.* American journal of neuroradiology, 1996. **17**(1): p. 89-94.

70. Korn, A., B. Bender, C. Thomas, S. Danz, M. Fenchel, T. Nägele, et al., *Dual energy CTA of the carotid bifurcation: advantage of plaque subtraction for assessment of grade of the stenosis and morphology.* European journal of radiology, 2011. **80**(2): p. e120-e125.

71. Vlahos, I., R. Chung, A. Nair, and R. Morgan, *Dual-energy CT: vascular applications.* American Journal of Roentgenology, 2012. **199**(5_supplement): p. S87-S97.

72. Klingebiel, R., M. Kentenich, H.-C. Bauknecht, F. Masuhr, E. Siebert, M. Busch, et al., *Comparative evaluation of 64-slice CT angiography and digital subtraction angiography in assessing the cervicocranial vasculature.* Vascular health and risk management, 2008. **4**(4): p. 901.

73. Manninen, A.-L., J.-M. Isokangas, A. Karttunen, T. Siniluoto, and M. Nieminen, *A comparison of radiation exposure between diagnostic CTA and DSA examinations of cerebral and cervicocerebral vessels.* American Journal of Neuroradiology, 2012. **33**(11): p. 2038-2042.

74. Hasebroock, K.M. and N.J. Serkova, *Toxicity of MRI and CT contrast agents.* Expert opinion on drug metabolism & toxicology, 2009. **5**(4): p. 403-416.

75. Laub, G. and W. Kaiser, *MR angiography with gradient motion refocusing.* Journal of computer assisted tomography, 1988. **12**(3): p. 377-382.

76. Gullberg, G.T., F.W. Wehrli, A. Shimakawa, and M. Simons, *MR vascular imaging with a fast gradient refocusing pulse sequence and reformatted images from transaxial sections.* Radiology, 1987. **165**(1): p. 241-246.

77. Anderson, C., D. Saloner, R. Lee, V. Griswold, L. Shapeero, J. Rapp, et al., *Assessment of carotid artery stenosis by MR angiography: comparison with x-ray angiography and color-coded Doppler ultrasound.* American journal of neuroradiology, 1992. **13**(3): p. 989-1003.

78. Yucel, E.K., C.M. Anderson, R.R. Edelman, T.M. Grist, R.A. Baum, W.J. Manning, et al., *Magnetic resonance angiography update on applications for extracranial arteries.* Circulation, 1999. **100**(22): p. 2284-2301.

79. Etesami, M., Y. Hoi, D. Steinman, S. Gujar, A. Nidecker, B. Astor, et al., *Comparison of carotid plaque ulcer detection using contrast-enhanced and time-of-flight MRA techniques.* American Journal of Neuroradiology, 2013. **34**(1): p. 177-184.

80. Raoult, H., J.-Y. Gauvrit, P. Schmitt, V. Le Couls, and E. Bannier, *Non-ECG-gated unenhanced MRA of the carotids: Optimization and clinical feasibility.* European radiology, 2013. **23**(11): p. 3020-3028.

81. Koktzoglou, I., M.T. Walker, J.R. Meyer, I.G. Murphy, and R.R. Edelman, *Nonenhanced hybridized arterial spin labeled magnetic resonance angiography of the extracranial carotid arteries using a fast low angle shot readout at 3 Tesla.* Journal of Cardiovascular Magnetic Resonance, 2016. **18**(1): p. 1.

82. Takei, N., M. Miyoshi, and H. Kabasawa, *Noncontrast MR angiography for supraaortic arteries using inflow enhanced inversion recovery fast spin echo imaging.* Journal of Magnetic Resonance Imaging, 2012. **35**(4): p. 957-962.

83. Koktzoglou, I., I.G. Murphy, S. Giri, and R.R. Edelman, *Quiescent interval low angle shot magnetic resonance angiography of the extracranial carotid arteries.* Magnetic resonance in medicine, 2015.

84. Priest, A.N., M.J. Graves, and D.J. Lomas, *Non‐contrast‐enhanced vascular magnetic resonance imaging using flow‐dependent preparation with subtraction.* Magnetic resonance in medicine, 2012. **67**(3): p. 628-637.

85. Demarco, J., H. Ota, H. Underhill, D. Zhu, M. Reeves, M. Potchen, et al., *MR carotid plaque imaging and contrast-enhanced MR angiography identifies lesions associated with recent ipsilateral thromboembolic symptoms: an in vivo study at 3T.* American Journal of Neuroradiology, 2010. **31**(8): p. 1395-1402.

86. Edelman, R.R., D. Chien, and D. Kim, *Fast selective black blood MR imaging.* Radiology, 1991. **181**(3): p. 655-660.

87. Yarnykh, V.L. and C. Yuan, *T1 ‐insensitive flow suppression using quadruple inversion ‐recovery.* Magnetic resonance in medicine, 2002. **48**(5): p. 899-905.

88. Wang, J., V.L. Yarnykh, T. Hatsukami, B. Chu, N. Balu, and C. Yuan, *Improved suppression of plaque ‐mimicking artifacts in black ‐blood carotid atherosclerosis imaging using a multislice motion ‐sensitized driven ‐equilibrium (MSDE) turbo spin ‐echo (TSE) sequence.* Magnetic resonance in medicine, 2007. **58**(5): p. 973-981.

89. Li, L., K.L. Miller, and P. Jezzard, *DANTE ‐prepared pulse trains: A novel approach to motion ‐sensitized and motion ‐suppressed quantitative magnetic resonance imaging.* Magnetic resonance in medicine, 2012. **68**(5): p. 1423-1438.

90. Chu, B., C. Yuan, N. Takaya, J.R. Shewchuk, A.W. Clowes, and T.S. Hatsukami, *Serial high-spatial-resolution, multisequence magnetic resonance imaging studies identify fibrous cap rupture and penetrating ulcer into carotid atherosclerotic plaque.* Circulation, 2006. **113**(12): p. e660-e661.

91. Chu, B., M.S. Ferguson, H. Underhill, N. Takaya, J. Cai, M. Kliot, et al., *Detection of carotid atherosclerotic plaque ulceration, calcification, and thrombosis by multicontrast weighted magnetic resonance imaging.* Circulation, 2005. **112**(1): p. e3-e4.

92. Bloch, F., *Nuclear induction.* Physical review, 1946. **70**(7-8): p. 460.

93. Purcell, E.M., H. Torrey, and R.V. Pound, *Resonance absorption by nuclear magnetic moments in a solid.* Physical review, 1946. **69**(1-2): p. 37.

94. Lauterbur, P.C., *Image formation by induced local interactions: examples employing nuclear magnetic resonance.* 1973.

95. Garroway, A.N., P.K. Grannell, and P. Mansfield, *Image formation in NMR by a selective irradiative process.* Journal of Physics C: Solid State Physics, 1974. **7**(24): p. L457.

96. Edelstein, W., J. Hutchison, G. Johnson, and T. Redpath, *Spin warp NMR imaging and applications to human whole-body imaging.* Physics in medicine and biology, 1980. **25**(4): p. 751.

97. Listerud, J., S. Einstein, E. Outwater, and H. Kressel, *First principles of fast spin echo.* Magnetic resonance quarterly, 1992. **8**(4): p. 199-244.

98. Roux, P.L. and R.S. Hinks, *Stabilization of echo amplitudes in FSE sequences.* Magnetic resonance in medicine, 1993. **30**(2): p. 183-190.

99. Alsop, D.C., *The sensitivity of low flip angle RARE imaging.* Magnetic resonance in medicine, 1997. **37**(2): p. 176-184.

100. Damadian, R., *Tumor detection by nuclear magnetic resonance.* 1971.

101. Stanisz, G.J., E.E. Odrobina, J. Pun, M. Escaravage, S.J. Graham, M.J. Bronskill, et al., *T1, T2 relaxation and magnetization transfer in tissue at 3T.* Magnetic resonance in medicine, 2005. **54**(3): p. 507-512.

102. Degnan, A.J., V.E. Young, T.Y. Tang, A.B. Gill, M.J. Graves, J.H. Gillard, et al., *Ex vivo study of carotid endarterectomy specimens: quantitative relaxation times within atherosclerotic plaque tissues.* Magnetic resonance imaging, 2012. **30**(7): p. 1017-1021.

103. Biasiolli, L., A.C. Lindsay, J.T. Chai, R.P. Choudhury, and M.D. Robson, *In-vivo quantitative T 2 mapping of carotid arteries in atherosclerotic patients: segmentation and T 2 measurement of plaque components.* Journal of Cardiovascular Magnetic Resonance, 2013. **15**(1): p. 69.

104. Biasiolli, L., A.C. Lindsay, J.T. Chai, R.P. Choudhury, and M.D. Robson, *In-vivo quantitative T2 mapping of carotid arteries in atherosclerotic patients: segmentation and T2 measurement of plaque components.* Journal of Cardiovascular Magnetic Resonance, 2013. **15**(1): p. 1-9.

105. Chai, J.T., L. Biasiolli, L. Li, M. Alkhalil, F. Galassi, C. Darby, et al., *Lipid-rich Core Quantification in Carotid Atherosclerosis Using MRI T2 Mapping-Relation to Clinical Presentation and Plaque Macrophage Activation.* Circulation, 2015. **132**(Suppl 3): p. A11833-A11833.

106. Proniewski, B., T. Miszalski-Jamka, and P. Jazwiec. *In vivo T2-mapping and segmentation of carotid artery plaque components using magnetic resonance imaging at 1.5 T*. in *Computing in Cardiology Conference (CinC), 2014*. 2014. IEEE.

107. LaMuraglia, G.M., J.F. Southern, V. Fuster, and H.L. Kantor, *Magnetic resonance images lipid, fibrous, calcified, hemorrhagic, and thrombotic components of human atherosclerosis in vivo.* Circulation, 1996. **94**(5): p. 932-938.

108. Dalager-Pedersen, S., E. Falk, S. Ringgaard, I.B. Kristensen, and E.M. Pedersen, *Effects of temperature and histopathologic preparation on the size and morphology of atherosclerotic carotid arteries as imaged by MRI.* Journal of magnetic resonance imaging, 1999. **10**(5): p. 876-885.

109. Morrisett, J., W. Vick, R. Sharma, G. Lawrie, M. Reardon, E. Ezell, et al., *Discrimination of components in atherosclerotic plaques from human carotid endarterectomy specimens by magnetic resonance imaging ex vivo.* Magnetic resonance imaging, 2003. **21**(5): p. 465-474.

110. Biasiolli, L., A.C. Lindsay, R.P. Choudhury, and M.D. Robson, *Loss of fine structure and edge sharpness in fast‐spin‐echo carotid wall imaging: measurements and comparison with multiple‐spin‐echo in normal and atherosclerotic subjects.* Journal of Magnetic Resonance Imaging, 2011. **33**(5): p. 1136-1143.

111. Gudbjartsson, H. and S. Patz, *The Rician distribution of noisy MRI data.* Magnetic resonance in medicine, 1995. **34**(6): p. 910-914.

112. Miller, A.J. and P.M. Joseph, *The use of power images to perform quantitative analysis on low SNR MR images.* Magnetic resonance imaging, 1993. **11**(7): p. 1051-1056.

113. Wang, J., V.L. Yarnykh, and C. Yuan, *Enhanced image quality in black‐blood MRI using the improved motion‐sensitized driven‐equilibrium (iMSDE) sequence.* Journal of Magnetic Resonance Imaging, 2010. **31**(5): p. 1256-1263.

114. Bernstein, M.A., K.F. King, and X.J. Zhou, *Handbook of MRI pulse sequences*. 2004: Elsevier.

115. Pipe, J.G., *A simple measure of flow disorder and wall shear stress in phase contrast MRI.* Magnetic resonance in medicine, 2003. **49**(3): p. 543-550.

116. Zur, Y., M. Wood, and L. Neuringer, *Spoiling of transverse magnetization in steady‐state sequences.* Magnetic resonance in medicine, 1991. **21**(2): p. 251-263.

117. Yuan, J., G. Makris, A. Patterson, A. Usman, T. Das, A. Priest, et al., *Relationship between carotid plaque surface morphology and perfusion: a 3D DCE-MRI study.* Magnetic Resonance Materials in Physics, Biology and Medicine, 2017: p. 1-9.

118. Padhani, A.R., *Dynamic contrast‐enhanced MRI in clinical oncology: Current status and future directions.* Journal of Magnetic Resonance Imaging, 2002. **16**(4): p. 407-422.

119. Kerwin, W.S., M. Oikawa, C. Yuan, G.P. Jarvik, and T. Hatsukami, *MR imaging of adventitial vasa vasorum in carotid atherosclerosis.* Magnetic Resonance in Medicine, 2008. **59**(3): p. 507-514.

120. Gaens, M.E., W.H. Backes, S. Rozel, M. Lipperts, S.N. Sanders, K. Jaspers, et al., *Dynamic contrast-enhanced MR imaging of carotid atherosclerotic plaque: model selection, reproducibility, and validation.* Radiology, 2013. **266**(1): p. 271-279.

121. Graves, M.J., *Pulse sequences for contrast-enhanced magnetic resonance imaging.* Radiography, 2007. **13**: p. e20-e30.

122. Larsson, H., M. Stubgaard, J. Frederiksen, M. Jensen, O. Henriksen, and O. Paulson, *Quantitation of blood‐brain barrier defect by magnetic resonance imaging and gadolinium‐DTPA in patients with multiple sclerosis and brain tumors.* Magnetic Resonance in Medicine, 1990. **16**(1): p. 117-131.

123. Weinmann, H., M. Laniado, and W. Mützel, *Pharmacokinetics of GdDTPA/dimeglumine after intravenous injection into healthy volunteers.* Physiological chemistry and physics and medical NMR, 1984. **16**(2): p. 167.

124. Fritz‐Hansen, T., E. Rostrup, H.B. Larsson, L. Søndergaard, P. Ring, and O. Henriksen, *Measurement of the arterial concentration of Gd‐DTPA using MRI: A step toward quantitative perfusion imaging.* Magnetic Resonance in Medicine, 1996. **36**(2): p. 225-231.

125. Port, R.E., M.V. Knopp, U. Hoffmann, S. Milker-Zabel, and G. Brix, *Multicompartment analysis of gadolinium chelate kinetics: blood-tissue exchange in mammary tumors as monitored by dynamic MR imaging.* Journal of Magnetic Resonance Imaging, 1999. **10**(3): p. 233-241.

126. Kovar, D.A., M. Lewis, and G.S. Karczmar, *A new method for imaging perfusion and contrast extraction fraction: input functions derived from reference tissues.* Journal of Magnetic Resonance Imaging, 1998. **8**(5): p. 1126-1134.

127. Yang, C., G.S. Karczmar, M. Medved, A. Oto, M. Zamora, and W.M. Stadler, *Reproducibility assessment of a multiple reference tissue method for quantitative dynamic contrast enhanced–MRI analysis.* Magnetic resonance in medicine, 2009. **61**(4): p. 851-859.

128. Tofts, P.S. and A.G. Kermode, *Measurement of the blood‐brain barrier permeability and leakage space using dynamic MR imaging. 1. Fundamental concepts.* Magnetic resonance in medicine, 1991. **17**(2): p. 357-367.

129. Tofts, P.S., *Modeling tracer kinetics in dynamic Gd‐DTPA MR imaging.* Journal of Magnetic Resonance Imaging, 1997. **7**(1): p. 91-101.

130. Patlak, C.S., R.G. Blasberg, and J.D. Fenstermacher, *Graphical evaluation of blood-to-brain transfer constants from multiple-time uptake data.* Journal of Cerebral Blood Flow & Metabolism, 1983. **3**(1): p. 1-7.

131. Randoux, B., B.a. Marro, F. Koskas, M. Duyme, M. Sahel, A. Zouaoui, et al., *Carotid Artery Stenosis: Prospective Comparison of CT, Three-dimensional Gadolinium-enhanced MR, and Conventional Angiography 1.* Radiology, 2001. **220**(1): p. 179-185.

132. Nederkoorn, P.J., P.T.M. Willem, B.C. Eikelboom, O.E. Elgersma, E. Buskens, M.M. Hunink, et al., *Preoperative diagnosis of carotid artery stenosis accuracy of noninvasive testing.* Stroke, 2002. **33**(8): p. 2003-2008.

133. U-King-Im, J., R. Trivedi, J. Cross, N. Higgins, M. Graves, P. Kirkpatrick, et al., *Conventional digital subtraction x-ray angiography versus magnetic resonance angiography in the evaluation of carotid disease: patient satisfaction and preferences.* Clinical radiology, 2004. **59**(4): p. 358-363.

134. Korosec, F.R., R. Frayne, T.M. Grist, and C.A. Mistretta, *Time‐resolved contrast‐enhanced 3D MR angiography.* Magnetic Resonance in Medicine, 1996. **36**(3): p. 345-351.

135. Kerwin, W., A. Hooker, M. Spilker, P. Vicini, M. Ferguson, T. Hatsukami, et al., *Quantitative magnetic resonance imaging analysis of neovasculature volume in carotid atherosclerotic plaque.* Circulation, 2003. **107**(6): p. 851-856.

136. Kerwin, W.S., K.D. O'Brien, M.S. Ferguson, N. Polissar, T.S. Hatsukami, and C. Yuan, *Inflammation in Carotid Atherosclerotic Plaque: A Dynamic Contrast-enhanced MR Imaging Study 1.* Radiology, 2006. **241**(2): p. 459-468.

137. Qiao, Y., M. Etesami, B. Astor, S. Zeiler, H. Trout, and B. Wasserman, *Carotid plaque neovascularization and hemorrhage detected by MR imaging are associated with recent cerebrovascular ischemic events.* American Journal of Neuroradiology, 2012. **33**(4): p. 755-760.

138. Barnett, H., D. Taylor, M. Eliasziw, A. Fox, G. Ferguson, R. Haynes, et al., *North American Symptomatic Carotid Endarterectomy Trial Collaborators Benefit of carotid endarterectomy in patients with symptomatic moderate or severe stenosis.* N Engl J Med, 1998. **339**(20): p. 1415-1425.

139. Zhu, C., *High resolution black blood magnetic resonance imaging of atherosclerotic plaque*, 2014, University of Cambridge.

140. Priest, A.N., I. Joubert, S. Hilborne, S. Hunter, D.J. Bowden, M.J. Graves, et al. *MR Direct Thrombus Imaging with optimised signal and improved lipid suppression*. in *Proceedings of the 21st scientific meeting, International Society for Magnetic Resonance in Medicine*. 2013. Salt Lake City.

141. Kitamura, A., H. Iso, H. Imano, T. Ohira, T. Okada, S. Sato, et al., *Carotid intima-media thickness and plaque characteristics as a risk factor for stroke in Japanese elderly men.* Stroke, 2004. **35**(12): p. 2788-2794.

142. Naylor, A., P. Rothwell, and P. Bell, *Overview of the principal results and secondary analyses from the European and North American randomised trials of endarterectomy for symptomatic carotid stenosis.* European Journal of Vascular and Endovascular Surgery, 2003. **26**(2): p. 115-129.

143. Kerwin, W., J. Cai, and C. Yuan, *Noise and motion correction in dynamic contrast‐enhanced MRI for analysis of atherosclerotic lesions.* Magnetic resonance in medicine, 2002. **47**(6): p. 1211-1217.

144. Li, L., J.T. Chai, L. Biasiolli, M.D. Robson, R.P. Choudhury, A.I. Handa, et al., *Black-blood multicontrast imaging of carotid arteries with DANTE-prepared 2D and 3D MR imaging.* Radiology, 2014. **273**(2): p. 560-569.

145. Team, R.C., *R: A language and environment for statistical computing. R Foundation for Statistical Computing, Vienna, Austria. 2013*, 2014.

146. Chen, H., J. Cai, X. Zhao, H. Underhill, H. Ota, M. Oikawa, et al., *Localized measurement of atherosclerotic plaque inflammatory burden with dynamic contrast–enhanced MRI.* Magnetic Resonance in Medicine, 2010. **64**(2): p. 567-573.

147. Truijman, M.T., R.M. Kwee, R.H. van Hoof, E. Hermeling, R.J. van Oostenbrugge, W.H. Mess, et al., *Combined 18F-FDG PET-CT and DCE-MRI to assess inflammation and microvascularization in atherosclerotic plaques.* Stroke, 2013. **44**(12): p. 3568-3570.

148. Sun, J., Y. Song, H. Chen, W.S. Kerwin, D.S. Hippe, L. Dong, et al., *Adventitial Perfusion and Intraplaque Hemorrhage A Dynamic Contrast-Enhanced MRI Study in the Carotid Artery.* Stroke, 2013. **44**(4): p. 1031-1036.

149. Kolodgie, F.D., H.K. Gold, A.P. Burke, D.R. Fowler, H.S. Kruth, D.K. Weber, et al., *Intraplaque hemorrhage and progression of coronary atheroma.* New England Journal of Medicine, 2003. **349**(24): p. 2316-2325.

150. Moreno, P.R., K.-R. Purushothaman, M. Sirol, A.P. Levy, and V. Fuster, *Neovascularization in human atherosclerosis.* Circulation, 2006. **113**(18): p. 2245-2252.

151. Wasserman, B.A., *Advanced Contrast-Enhanced MRI for Looking Beyond the Lumen to Predict Stroke Building a Risk Profile for Carotid Plaque.* Stroke, 2010. **41**(10 suppl 1): p. S12-S16.

152. Tudorica, L.A., K.Y. Oh, N. Roy, M.D. Kettler, Y. Chen, S.L. Hemmingson, et al., *A feasible high spatiotemporal resolution breast DCE-MRI protocol for clinical settings.* Magnetic resonance imaging, 2012. **30**(9): p. 1257-1267.

153. Bedair, R., M.J. Graves, A.J. Patterson, M.A. McLean, R. Manavaki, T. Wallace, et al., *Effect of radiofrequency transmit field correction on quantitative dynamic contrast-enhanced MR imaging of the breast at 3.0 T.* Radiology, 2015. **279**(2): p. 368-377.

154. Rödel, S. *Prostate: multiparametric magnetic resonance imaging (mpMRI) and MR-guided biopsy (MR-GB)*. 2014. European Congress of Radiology 2014.

155. Haeck, J., K. Bol, S. Bison, S. Tiel, S. Koelewijn, M. Jong, et al., *Optimized time‐resolved imaging of contrast kinetics (TRICKS) in dynamic contrast‐enhanced MRI after peptide receptor radionuclide therapy in small animal tumor models.* Contrast media & molecular imaging, 2015. **10**(6): p. 413-420.

156. Biasiolli, L., A.C. Lindsay, J.T. Chai, R.P. Choudhury, and M.D. Robson, *In-vivo quantitative T 2 mapping of carotid arteries in atherosclerotic patients: segmentation and T 2 measurement of plaque components.* Journal of Cardiovascular Magnetic Resonance, 2013. **15**(1): p. 1.

157. Biasiolli, L., J.T. Chai, L. Li, A. Handa, P. Jezzard, R. Choudhury, et al., *Histological validation of carotid plaque characterization by in-vivo T2 mapping in patients with recent cerebrovascular events: preliminary results.* Journal of Cardiovascular Magnetic Resonance, 2014. **16**(1): p. 1.

158. Proniewski, B., T. Miszalski-Jamka, and P. Jaźwiec. *In vivo T2-mapping and segmentation of carotid artery plaque components using magnetic resonance imaging at 1.5 T*. in *Computing in Cardiology 2014*. 2014. IEEE.

159. Yuan, J., A. Usman, S.A. Reid, K.F. King, A.J. Patterson, J.H. Gillard, et al., *Three-dimensional black-blood T2 mapping with compressed sensing and data-driven parallel imaging in the carotid artery.* Magnetic Resonance Imaging, 2017. **37**: p. 62-69.

160. Coolen, B.F., D.H. Poot, M.I. Liem, L.P. Smits, S. Gao, G. Kotek, et al., *Three‐dimensional quantitative T1 and T2 mapping of the carotid artery: Sequence design and in vivo feasibility.* Magnetic resonance in medicine, 2015.

161. Poon, C.S. and R.M. Henkelman, *Practical T2 quantitation for clinical applications.* Journal of Magnetic Resonance Imaging, 1992. **2**(5): p. 541-553.

162. Maier, C.F., S.G. Tan, H. Hariharan, and H.G. Potter, *T2 quantitation of articular cartilage at 1.5 T.* Journal of magnetic resonance imaging, 2003. **17**(3): p. 358-364.

163. Pai, A., X. Li, and S. Majumdar, *A comparative study at 3 T of sequence dependence of T 2 quantitation in the knee.* Magnetic resonance imaging, 2008. **26**(9): p. 1215-1220.

164. Li, B., H. Li, J. Li, Y. Zhang, X. Wang, J. Zhang, et al., *Relaxation enhanced compressed sensing three-dimensional black-blood vessel wall MR imaging: Preliminary studies.* Magnetic resonance imaging, 2015. **33**(7): p. 932-938.

165. Zhu, C., M.J. Graves, J. Yuan, U. Sadat, J.H. Gillard, and A.J. Patterson, *Optimization of Improved Motion-sensitized Driven-equilibrium (iMSDE) blood suppression for carotid artery wall imaging.* Journal of Cardiovascular Magnetic Resonance, 2014. **16**(1): p. 1.

166. Constantinides, C.D., E. Atalar, and E.R. McVeigh, *Signal‐to‐noise measurements in magnitude images from NMR phased arrays.* Magnetic Resonance in Medicine, 1997. **38**(5): p. 852-857.

167. Team, R.C., *R: A language and environment for statistical computing.* 2013.

168. Jinnan Wang, M.S., Chun Yuan, and Peter Börnert. *Inhomogeneity Insensitive MSDE (i2MSDE)*. in *Proc. Intl. Soc. Mag. Reson. Med. 22*. 2014.

169. Hu, B.S., S.M. Conolly, G.A. Wright, D.G. Nishimura, and A. Macovski, *Pulsed saturation transfer contrast.* Magnetic resonance in medicine, 1992. **26**(2): p. 231-240.

170. Alexander, A.L., H.R. Buswell, Y. Sun, B.E. Chapman, J.S. Tsuruda, and D.L. Parker, *Intracranial black‐blood MR angiography with high‐resolution 3D fast spin echo.* Magnetic resonance in medicine, 1998. **40**(2): p. 298-310.

171. Jara, H., B. Yu, S. Caruthers, E. Melhem, and E. Yucel, *Voxel sensitivity function description of flow‐induced signal loss in MR imaging: Implications for black‐blood MR angiography with turbo spin‐echo sequences.* Magnetic resonance in medicine, 1999. **41**(3): p. 575-590.

172. H. Smit, H.d.L., R. Pellicer Guridi, D.H.J. Poot, M. Vogel, A. van der Lugt, S. Klein and G. Kotek. *T2 mapping in the carotid artery with T2 prepared signal stabilized 3D fast spin echo*. in *European Society for Magnetic Resonance in Medicine and Biology*. 2013.

173. Zhao, X., N. Balu, J. Wang, H. Zhao, J. Xu, and C. Yuan. *Carotid Atherosclerotic Lesion Distribution in Patients with Cerebrovascular Events: A 3.0 Tesla Magnetic Resonance Vessel Wall Imaging Study Using Three-dimensional, Isotropic, Fast Sequence with Large Coverage*. in *Proc. Intl. Soc. Mag. Reson. Med. 19*. 2011.

174. Balu, N., B. Chu, T.S. Hatsukami, C. Yuan, and V.L. Yarnykh, *Comparison between 2D and 3D high‐resolution black‐blood techniques for carotid artery wall imaging in clinically significant atherosclerosis.* Journal of Magnetic Resonance Imaging, 2008. **27**(4): p. 918-924.

175. Majumdar, S., S. Orphanoudakis, A. Gmitro, M. O'donnell, and J. Gore, *Errors in the measurements of T2 using multiple‐echo MRI techniques. I. Effects of radiofrequency pulse imperfections.* Magnetic resonance in medicine, 1986. **3**(3): p. 397-417.

176. Bönner, F., N. Janzarik, C. Jacoby, M. Spieker, B. Schnackenburg, F. Range, et al., *Myocardial T2 mapping reveals age-and sex-related differences in volunteers.* Journal of Cardiovascular Magnetic Resonance, 2015. **17**(1): p. 1.

177. Chen, X., H. Zhang, Q. Yang, Z. Luo, Z. Zhang, Z. Cheng, et al., *Value of severe liver iron overload for assessing heart iron levels in thalassemia major patients.* Journal of Magnetic Resonance Imaging, 2016. **44**(4): p. 880-889.

178. Saam, T., J.G. Raya, C.C. Cyran, K. Bochmann, G. Meimarakis, O. Dietrich, et al., *High resolution carotid black-blood 3T MR with parallel imaging and dedicated 4-channel surface coils.* Journal of Cardiovascular Magnetic Resonance, 2009. **11**(1): p. 1.

179. Li, B., L. Dong, B. Chen, S. Ji, W. Cai, Y. Wang, et al., *Turbo fast three‐dimensional carotid artery black‐blood MRI by combining three‐dimensional MERGE sequence with compressed sensing.* Magnetic resonance in medicine, 2013. **70**(5): p. 1347-1352.

180. Yuan, J., A. Usman, S.A. Reid, K.F. King, A.J. Patterson, J.H. Gillard, et al., *Three-dimensional black-blood T 2 mapping with compressed sensing and data-driven parallel imaging in the carotid artery.* Magnetic Resonance Imaging, 2017. **37**: p. 62-69.

181. Lustig, M., D.L. Donoho, J.M. Santos, and J.M. Pauly, *Compressed sensing MRI.* IEEE signal processing magazine, 2008. **25**(2): p. 72-82.

182. King, K., D. Xu, A. Brau, P. Lai, P. Beatty, and L. Marinelli. *A new combination of compressed sensing and data driven parallel imaging*. in *Proceedings of 18th Annual Meeting of ISMRM, Stockholm, Sweden*. 2010.

183. Busse, R.F., A. Brau, A. Vu, C.R. Michelich, E. Bayram, R. Kijowski, et al., *Effects of refocusing flip angle modulation and view ordering in 3D fast spin echo.* Magnetic resonance in medicine, 2008. **60**(3): p. 640-649.

184. Priest, A.N., I. Joubert, S. Hilborne, S. Hunter, D.J. Bowden, M.J. Graves, et al. *MR Direct Thrombus Imaging with optimised signal and improved lipid suppression*. in *Proceedings of 21st Annual Meeting of ISMRM, Salt Lake City, Utah, USA*. 2013.

185. Larson, A.C., P. Kellman, A. Arai, G.A. Hirsch, E. McVeigh, D. Li, et al., *Preliminary investigation of respiratory self‐gating for free‐breathing segmented cine MRI.* Magnetic resonance in medicine, 2005. **53**(1): p. 159-168.

186. Team, R.C., *R: A language and environment for statistical computing. R Foundation for Statistical Computing, Vienna, Austria, 2012*, 2014, ISBN 3-900051-07-0.

187. Bland, J.M. and D. Altman, *Statistical methods for assessing agreement between two methods of clinical measurement.* The lancet, 1986. **327**(8476): p. 307-310.

188. Otazo, R., L. Feng, R. Lim, Q. Duan, G. Wiggins, D.K. Sodickson, et al., *Accelerated 3D carotid MRI using compressed sensing and parallel imaging.* Journal of Cardiovascular Magnetic Resonance, 2010. **12**(1): p. 1.

189. Tao, Y., G. Rilling, M. Davies, and I. Marshall, *Carotid blood flow measurement accelerated by compressed sensing: Validation in healthy volunteers.* Magnetic resonance imaging, 2013. **31**(9): p. 1485-1491.

190. Makhijani, M.K., N. Balu, K. Yamada, C. Yuan, and K.S. Nayak, *Accelerated 3D MERGE carotid imaging using compressed sensing with a hidden Markov tree model.* Journal of Magnetic Resonance Imaging, 2012. **36**(5): p. 1194-1202.

191. Grimm, J.M., A. Schindler, T. Freilinger, C.C. Cyran, F. Bamberg, C. Yuan, et al., *Comparison of symptomatic and asymptomatic atherosclerotic carotid plaques using parallel imaging and 3 T black-blood in vivo CMR.* J Cardiovasc Magn Reson, 2013. **15**: p. 44.

192. Sumi, T., M. Sumi, M. Van Cauteren, Y. Kimura, and T. Nakamura, *Parallel imaging technique for the external carotid artery and its branches: Comparison of balanced turbo field echo, phase contrast, and time‐of‐flight sequences.* Journal of Magnetic Resonance Imaging, 2007. **25**(5): p. 1028-1034.

193. Smit, H., H.d. Leeuw, R.P. Guridi, D.H.J. Poot, M. Vogel, A.v.d. Lugt, et al., *T2 mapping in the carotid artery with T2 prepared signal stabilized 3D fast spin echo.* Presentation at ESMRMB 2013, 2013.

194. Zhu, C., M.J. Graves, U. Sadat, V.E. Young, J.H. Gillard, and A.J. Patterson, *Comparison of Gated and Ungated Black-Blood Fast Spin-echo MRI of Carotid Vessel Wall at 3T.* Magnetic Resonance in Medical Sciences, 2015. **15(3)**(0): p. 266-72.

195. Chartrand, R. *Fast algorithms for nonconvex compressive sensing: MRI reconstruction from very few data*. in *2009 IEEE International Symposium on Biomedical Imaging: From Nano to Macro*. 2009. IEEE.
196. Badnjar, J., *Comparison of Algorithms for Compressed Sensing of Magnetic Resonance Images.* arXiv preprint arXiv:1502.02182, 2015.
197. Ma, S., W. Yin, Y. Zhang, and A. Chakraborty. *An efficient algorithm for compressed MR imaging using total variation and wavelets*. in *Computer Vision and Pattern Recognition, 2008. CVPR 2008. IEEE Conference on*. 2008. IEEE.
198. Lustig, M., M. Alley, S. Vasanawala, D. Donoho, and J. Pauly. *L1 SPIR-iT: autocalibrating parallel imaging compressed sensing*. in *Proc Intl Soc Mag Reson Med*. 2009.
199. Otazo, R., D. Kim, L. Axel, and D.K. Sodickson, *Combination of compressed sensing and parallel imaging for highly accelerated first‐pass cardiac perfusion MRI.* Magnetic Resonance in Medicine, 2010. **64**(3): p. 767-776.
200. Hollingsworth, K.G., *Reducing acquisition time in clinical MRI by data undersampling and compressed sensing reconstruction.* Physics in medicine and biology, 2015. **60**(21): p. R297.
201. Kuestner, T., C. Wurslin, S. Gatidis, P. Martirosian, K. Nikolaou, N. Schwenzer, et al., *MR image reconstruction using a combination of Compressed Sensing and partial Fourier acquisition: ESPReSSo.* IEEE transactions on medical imaging, 2016. **35(11)**: p. 2447-58.
202. Tamir, J.I., M. Uecker, W. Chen, P. Lai, M.T. Alley, S.S. Vasanawala, et al., *T2 shuffling: Sharp, multicontrast, volumetric fast spin‐echo imaging.* Magnetic resonance in medicine, 2016.
203. Cai, J.-M., T.S. Hatsukami, M.S. Ferguson, R. Small, N.L. Polissar, and C. Yuan, *Classification of human carotid atherosclerotic lesions with in vivo multicontrast magnetic resonance imaging.* Circulation, 2002. **106**(11): p. 1368-1373.
204. Liu, W., N. Balu, J. Sun, X. Zhao, H. Chen, C. Yuan, et al., *Segmentation of carotid plaque using multicontrast 3D gradient echo MRI.* Journal of Magnetic Resonance Imaging, 2012. **35**(4): p. 812-819.
205. Yoneyama, T., J. Sun, D.S. Hippe, N. Balu, D. Xu, W.S. Kerwin, et al., *In vivo semi-automatic segmentation of multicontrast cardiovascular magnetic resonance for prospective cohort studies on plaque tissue composition: initial experience.* The international journal of cardiovascular imaging, 2016. **32**(1): p. 73-81.
206. Edelman, R.R., H.P. Mattle, B. Wallner, R. Bajakian, J. Kleefield, C. Kent, et al., *Extracranial carotid arteries: evaluation with" black blood" MR angiography.* Radiology, 1990. **177**(1): p. 45-50.

207. Fan, Z., Z. Zhang, Y.C. Chung, P. Weale, S. Zuehlsdorff, J. Carr, et al., *Carotid arterial wall MRI at 3T using 3D variable‐flip‐angle turbo spin‐echo (TSE) with flow‐sensitive dephasing (FSD).* Journal of Magnetic Resonance Imaging, 2010. **31**(3): p. 645-654.

208. Zhu, C., U. Sadat, A.J. Patterson, Z. Teng, J.H. Gillard, and M.J. Graves, *3D high-resolution contrast enhanced MRI of carotid atheroma—a technical update.* Magnetic resonance imaging, 2014. **32**(5): p. 594-597.

209. Zhu, C., M.J. Graves, J. Yuan, U. Sadat, J.H. Gillard, and A.J. Patterson, *Optimization of Improved Motion-sensitized Driven-equilibrium (iMSDE) blood suppression for carotid artery wall imaging.* Journal of Cardiovascular Magnetic Resonance, 2014. **16**: p. 61.

210. Grimm, J.M., A. Schindler, T. Freilinger, C.C. Cyran, F. Bamberg, C. Yuan, et al., *Comparison of symptomatic and asymptomatic atherosclerotic carotid plaques using parallel imaging and 3 T black-blood in vivo CMR.* Journal of Cardiovascular Magnetic Resonance, 2013. **15**: p. 44.

211. Fan, Z., W. Yu, Y. Xie, L. Dong, L. Yang, Z. Wang, et al., *Multi-contrast atherosclerosis characterization (MATCH) of carotid plaque with a single 5-min scan: technical development and clinical feasibility.* Journal of Cardiovascular Magnetic Resonance, 2014. **16**: p. 53.

212. Lustig, M., D. Donoho, and J.M. Pauly, *Sparse MRI: The application of compressed sensing for rapid MR imaging.* Magnetic resonance in medicine, 2007. **58**(6): p. 1182-1195.

213. Li, H., B. Li, W. Huang, L. Dong, and J. Zhang, *Flow artifact removal in carotid wall imaging based on black and gray‐blood dual‐contrast images subtraction.* Magnetic resonance in medicine, 2016.

214. Pandit, P., J. Rivoire, K. King, and X. Li, *Accelerated T1ρ acquisition for knee cartilage quantification using compressed sensing and data-driven parallel imaging: A feasibility study.* Magnetic resonance in medicine, 2016. **75**(3): p. 1256-1261.

215. Donker, D., A. Hasman, and H. Van Geijn, *Interpretation of low kappa values.* International journal of bio-medical computing, 1993. **33**(1): p. 55-64.

216. Kang, X., N.L. Polissar, C. Han, E. Lin, and C. Yuan, *Analysis of the measurement precision of arterial lumen and wall areas using high‐resolution MRI.* Magnetic resonance in medicine, 2000. **44**(6): p. 968-972.

217. Yuan, C., L.M. Mitsumori, M.S. Ferguson, N.L. Polissar, D. Echelard, G. Ortiz, et al., *In vivo accuracy of multispectral magnetic resonance imaging for identifying lipid-rich necrotic cores and intraplaque hemorrhage in advanced human carotid plaques.* Circulation, 2001. **104**(17): p. 2051-2056.

218. Saam, T., W.S. Kerwin, B. Chu, J. Cai, A. Kampschulte, T.S. Hatsukami, et al., *Sample size calculation for clinical trials using magnetic resonance imaging for the quantitative assessment of carotid atherosclerosis.* Journal of Cardiovascular Magnetic Resonance, 2005. **7**(5): p. 799-808.

219. Cappendijk, V.C., K.B. Cleutjens, A.G. Kessels, S. Heeneman, G.W.H. Schurink, R.J. Welten, et al., *Assessment of human atherosclerotic carotid plaque components with multisequence MR imaging: initial Experience 1.* Radiology, 2005. **234**(2): p. 487-492.

220. Chu, B., X.Q. Zhao, T. Saam, V.L. Yarnykh, W.S. Kerwin, K.D. Flemming, et al., *Feasibility of in vivo, multicontrast‐weighted MR imaging of carotid atherosclerosis for multicenter studies.* Journal of Magnetic Resonance Imaging, 2005. **21**(6): p. 809-817.

221. Yarnykh, V.L., M. Terashima, C.E. Hayes, A. Shimakawa, N. Takaya, P.K. Nguyen, et al., *Multicontrast black‐blood MRI of carotid arteries: Comparison between 1.5 and 3 tesla magnetic field strengths.* Journal of magnetic resonance imaging, 2006. **23**(5): p. 691-698.

222. Li, F., V.L. Yarnykh, T.S. Hatsukami, B. Chu, N. Balu, J. Wang, et al., *Scan‐rescan reproducibility of carotid atherosclerotic plaque morphology and tissue composition measurements using multicontrast MRI at 3T.* Journal of Magnetic Resonance Imaging, 2010. **31**(1): p. 168-176.

223. Young, V., A. Patterson, E. Tunnicliffe, U. Sadat, M. Graves, T. Tang, et al., *Signal-to-noise ratio increase in carotid atheroma MRI: a comparison of 1.5 and 3 T.* The British journal of radiology, 2014. **85**(1015): p. 937-944.

224. Yuan, J., A. Usman, T. Das, A. Patterson, J. Gillard, and M. Graves, *Imaging Carotid Atherosclerosis Plaque Ulceration: Comparison of Advanced Imaging Modalities and Recent Developments.* American Journal of Neuroradiology, 2016.

225. Kröner, E., J. Westenberg, R. van der Geest, N. Brouwer, J. Doornbos, M. Kooi, et al., *High field carotid vessel wall imaging: a study on reproducibility.* European journal of radiology, 2013. **82**(4): p. 680-685.

226. Roberts, J.A., S.-E. Kim, H.-C. Yoon, J.S. McNally, J.R. Hadley, L.K. Findeiss, et al., *Reproducibility of Lumen and Vessel Wall Measurements in Carotid Magnetic Resonance Imaging.* The Open Cardiovascular and Thoracic Surgery Journal, 2012. **5**: p. 1-7.

227. Zhou, Z., R. Li, X. Zhao, L. He, X. Wang, J. Wang, et al., *Evaluation of 3D multi-contrast joint intra-and extracranial vessel wall cardiovascular magnetic resonance.* Journal of Cardiovascular Magnetic Resonance, 2015. **17**(1): p. 41.

228. Li, B., H. Li, H. Kong, L. Dong, J. Zhang, and J. Fang, *Compressed sensing based simultaneous black-and gray-blood carotid vessel wall MR imaging.* Magnetic resonance imaging, 2017. **38**: p. 214-223.

229. Zhou, Z.-W., B. Sharif, Z. Fan, Y. Xie, and D. Li, *High spatial and temporal resolution black-blood dynamic contrast-enhanced carotid artery wall MRI using compressed sensing.* Journal of Cardiovascular Magnetic Resonance, 2014. **16**(S1): p. W40.

230. Akçakaya, M., T.A. Basha, R.H. Chan, W.J. Manning, and R. Nezafat, *Accelerated isotropic sub‐millimeter whole‐heart coronary MRI: Compressed sensing versus parallel imaging.* Magnetic resonance in medicine, 2014. **71**(2): p. 815-822.

231. King, K. *Combining compressed sensing and parallel imaging*. in *proceedings of the 16th annual meeting, International Society for Magnetic Resonance in Medicine, Toronto*. 2008.

232. Bilgic, B., V.K. Goyal, and E. Adalsteinsson, *Multi‐contrast reconstruction with Bayesian compressed sensing.* Magnetic Resonance in Medicine, 2011. **66**(6): p. 1601-1615.

233. Westwood, M., L.J. Anderson, D.N. Firmin, P.D. Gatehouse, C.C. Charrier, B. Wonke, et al., *A single breath-hold multiecho T2* cardiovascular magnetic resonance technique for diagnosis of myocardial iron overload.* Journal of Magnetic Resonance Imaging, 2003. **18**(1): p. 33-39.

234. Kirk, P., T. He, L.J. Anderson, M. Roughton, M.A. Tanner, W.W. Lam, et al., *International reproducibility of single breathhold T2* MR for cardiac and liver iron assessment among five thalassemia centers.* Journal of Magnetic Resonance Imaging, 2010. **32**(2): p. 315-319.

235. Wood, J.C., C. Enriquez, N. Ghugre, J.M. Tyzka, S. Carson, M.D. Nelson, et al., *MRI R2 and R2* mapping accurately estimates hepatic iron concentration in transfusion-dependent thalassemia and sickle cell disease patients.* Blood, 2005. **106**(4): p. 1460-1465.

236. Alam, S.R., C. Stirrat, J. Richards, S. Mirsadraee, S.I. Semple, G. Tse, et al., *Vascular and plaque imaging with ultrasmall superparamagnetic particles of iron oxide.* Journal of Cardiovascular Magnetic Resonance, 2015. **17**(1): p. 1.

237. Richards, J.M., S.I. Semple, T.J. MacGillivray, C. Gray, J.P. Langrish, M. Williams, et al., *Abdominal aortic aneurysm growth predicted by uptake of ultrasmall superparamagnetic particles of iron oxide a pilot study.* Circulation: Cardiovascular Imaging, 2011. **4**(3): p. 274-281.

238. Patterson, A.J., T.Y. Tang, M.J. Graves, K.H. Müller, and J.H. Gillard, *In vivo carotid plaque MRI using quantitative T2* measurements with ultrasmall superparamagnetic iron oxide particles: a dose-response study to statin therapy.* NMR in Biomedicine, 2011. **24**(1): p. 89-95.

239. McBride, O.M., C. Berry, P. Burns, R.T. Chalmers, B. Doyle, R. Forsythe, et al., *MRI using ultrasmall superparamagnetic particles of iron oxide in patients under surveillance for abdominal aortic aneurysms to predict rupture or surgical repair: MRI for abdominal aortic*

aneurysms to predict rupture or surgery-the MA3RS study. Open heart, 2015. **2**(1): p. e000190.

240. Westwood, M.A., L.J. Anderson, D.N. Firmin, P.D. Gatehouse, C.H. Lorenz, B. Wonke, et al., *Interscanner reproducibility of cardiovascular magnetic resonance T2* measurements of tissue iron in thalassemia.* Journal of Magnetic Resonance Imaging, 2003. **18**(5): p. 616-620.

241. He, T., P.D. Gatehouse, P. Kirk, M.A. Tanner, G.C. Smith, J. Keegan, et al., *Black-blood T2* technique for myocardial iron measurement in thalassemia.* Journal of Magnetic Resonance Imaging, 2007. **25**(6): p. 1205-1209.

242. Smith, G.C., J.P. Carpenter, T. He, M.H. Alam, D.N. Firmin, and D.J. Pennell, *Value of black blood T2* cardiovascular magnetic resonance.* Journal of Cardiovascular Magnetic Resonance, 2011. **13**(1): p. 1.

243. Khater, N.H., H.M. El Shahat, H.S. Fahmy, and S.S. El Hadidy, *Comparative study between black blood T2∗ and conventional bright GRE sequences in assessment of myocardial iron concentration.* The Egyptian Journal of Radiology and Nuclear Medicine, 2016. **47**(2): p. 407-412.

244. Raman, S.V., M.W. Winner, T. Tran, M. Velayutham, O.P. Simonetti, P.B. Baker, et al., *In vivo atherosclerotic plaque characterization using magnetic susceptibility distinguishes symptom-producing plaques.* JACC: Cardiovascular Imaging, 2008. **1**(1): p. 49-57.

245. Kooi, M., V. Cappendijk, K. Cleutjens, A. Kessels, P. Kitslaar, M. Borgers, et al., *Accumulation of ultrasmall superparamagnetic particles of iron oxide in human atherosclerotic plaques can be detected by in vivo magnetic resonance imaging.* Circulation, 2003. **107**(19): p. 2453-2458.

246. Tang, T.Y., K.H. Muller, M.J. Graves, Z.Y. Li, S.R. Walsh, V. Young, et al., *Iron oxide particles for atheroma imaging.* Arteriosclerosis, thrombosis, and vascular biology, 2009. **29**(7): p. 1001-1008.

247. Sadeghi, M.M., D.K. Glover, G.M. Lanza, Z.A. Fayad, and L.L. Johnson, *Imaging atherosclerosis and vulnerable plaque.* Journal of Nuclear Medicine, 2010. **51**(Supplement 1): p. 51S-65S.

248. Usman, A., U. Sadat, A.J. Patterson, T.Y. Tang, K. Varty, J.R. Boyle, et al., *Use of ultrasmall superparamagnetic iron oxide particles for imaging carotid atherosclerosis.* Nanomedicine, 2015. **10**(19): p. 3077-3087.

249. Tang, T.Y., S.P. Howarth, S.R. Miller, M.J. Graves, A.J. Patterson, U. Jean-Marie, et al., *The ATHEROMA (Atorvastatin Therapy: Effects on Reduction of Macrophage Activity) Study: evaluation using ultrasmall superparamagnetic iron oxide-enhanced magnetic resonance imaging in carotid disease.* Journal of the American College of Cardiology, 2009. **53**(22): p. 2039-2050.

250. Su, S., Y. Ren, C. Shi, X. Zhang, H. Zheng, X. Liu, et al. *Black-Blood T2* Mapping with Delay Alternating with Nutation for Tailored Excitation*. in *Proceedings of the 24th scientific meeting, International Society for Magnetic Resonance in Medicine, Singapore*. 2016.

251. Newbould, R.D., D.R. Owen, J. Shalhoub, A.P. Brown, and G. Gambarota, *Motion-sensitized driven equilibrium for blood-suppressed T2* mapping.* Journal of Magnetic Resonance Imaging, 2011. **34**(3): p. 702-709.

252. Wang, J., V.L. Yarnykh, and C. Yuan, *Enhanced image quality in black-blood MRI using the improved motion-sensitized driven-equilibrium (iMSDE) sequence.* Journal of Magnetic Resonance Imaging, 2010. **31**(5): p. 1256-1263.

253. Li, L., K.L. Miller, and P. Jezzard, *DANTE-prepared pulse trains: A novel approach to motion-sensitized and motion-suppressed quantitative magnetic resonance imaging.* Magnetic resonance in medicine, 2012. **68**(5): p. 1423-1438.

254. Vu, A.T., *Method and apparatus for acquiring MR data with a segmented multi-shot radial fan beam encoding order*, 2007, Patent US7265547 B2.

255. Feiweier, T., *Magnetic resonance imaging data acquisition sequence and apparatus*, 2010, Patent US7728588 B2.

256. Team, R.C. *R: A language and environment for statistical computing. R Foundation for Statistical Computing, Vienna, Austria. 2013*. 2014; Available from: http://www.R-project.org/. .

257. Harteveld, A., N. Denswil, J. Siero, J. Zwanenburg, A. Vink, B. Pouran, et al., *Quantitative intracranial atherosclerotic plaque characterization at 7t mri: an ex vivo study with histologic validation.* American Journal of Neuroradiology, 2016. **37**(5): p. 802-810.

258. Sadat, U., V. Taviani, A. Patterson, V. Young, M. Graves, Z. Teng, et al., *Ultrasmall superparamagnetic iron oxide-enhanced magnetic resonance imaging of abdominal aortic aneurysms–a feasibility study.* European Journal of Vascular and Endovascular Surgery, 2011. **41**(2): p. 167-174.

259. Zhou, Q., K.R. Yang, P. Gao, W.L. Chen, D.Y. Yang, M.J. Liang, et al., *An experimental study on MR imaging of atherosclerotic plaque with SPIO marked endothelial cells in a rabbit model.* Journal of Magnetic Resonance Imaging, 2011. **34**(6): p. 1325-1332.

260. Trivedi, R.A., C. Mallawarachi, U. Jean-Marie, M.J. Graves, J. Horsley, M.J. Goddard, et al., *Identifying inflamed carotid plaques using in vivo USPIO-enhanced MR imaging to label plaque macrophages.* Arteriosclerosis, thrombosis, and vascular biology, 2006. **26**(7): p. 1601-1606.

261. Yang, Q., J. Liu, S.R. Barnes, Z. Wu, K. Li, J. Neelavalli, et al., *Imaging the vessel wall in major peripheral arteries using susceptibility-weighted imaging.* Journal of Magnetic Resonance Imaging, 2009. **30**(2): p. 357-365.

262. Yang, Q., K. Li, J. Liu, S. Barnes, Z. Wu, J. Neelavalli, et al., *Imaging the vessel wall in major peripheral arteries using susceptibility weighted imaging: visualizing calcifications.* Journal of Cardiovascular Magnetic Resonance, 2009. **11**(S1): p. O12.

263. Wang, C., S. Liu, S. Buch, H.S. Choi, E.-J. Hwang, Z. Fan, et al. *Quantitative Susceptibility Mapping of Atherosclerosis in Carotid Arteries*. in *Proceedings of the 24th scientific meeting, International Society for Magnetic Resonance in Medicine, Singapore*. 2016.

264. Biasiolli, L., A.C. Lindsay, J.T. Chai, R.P. Choudhury, and M.D. Robson, *In-vivo quantitative T2 mapping of carotid arteries in atherosclerotic patients: segmentation and T2 measurement of plaque components.* Journal of Cardiovascular Magnetic Resonance, 2013. **15**(1): p. 1.

265. Chai, J.T., L. Biasiolli, L. Li, M. Alkhalil, F. Galassi, C. Darby, et al. *Quantification of Lipid-Rich Core in Carotid Atherosclerosis Using Magnetic Resonance T2 Mapping: Relation to Clinical Presentation*. in *JACC: Cardiovascular Imaging*. 2016.

266. Viessmann, O., L. Li, P. Benjamin, and P. Jezzard, *T2-Weighted intracranial vessel wall imaging at 7 Tesla using a DANTE-prepared variable flip angle turbo spin echo readout (DANTE-SPACE).* Magnetic resonance in medicine, 2017. **77**(2): p. 655-663.

267. Bieri, O., M. Markl, and K. Scheffler, *Analysis and compensation of eddy currents in balanced SSFP.* Magnetic resonance in medicine, 2005. **54**(1): p. 129-137.

268. Liu, J. and D. Saloner, *Accelerated MRI with CIRcular Cartesian UnderSampling (CIRCUS): a variable density Cartesian sampling strategy for compressed sensing and parallel imaging.* Quantitative imaging in medicine and surgery, 2014. **4**(1): p. 57-67.

269. Chengcheng, Z., M.J. Graves, U. Sadat, V.E. Young, J.H. Gillard, and A.J. Patterson, *Comparison of gated and ungated black-blood fast spin-echo MRI of carotid Vessel Wall at 3T.* Magnetic Resonance in Medical Sciences, 2016. **15**(3): p. 266-272.

270. Saranathan, M., D.W. Rettmann, B.A. Hargreaves, S.E. Clarke, and S.S. Vasanawala, *DIfferential subsampling with cartesian ordering (DISCO): A high spatio‐temporal resolution dixon imaging sequence for multiphasic contrast enhanced abdominal imaging.* Journal of Magnetic Resonance Imaging, 2012. **35**(6): p. 1484-1492.

271. Wang, H., Y. Miao, K. Zhou, Y. Yu, S. Bao, Q. He, et al., *Feasibility of high temporal resolution breast DCE‐MRI using compressed sensing theory.* Medical physics, 2010. **37**(9): p. 4971-4981.

272. Clarke, S.E., R.R. Hammond, J.R. Mitchell, and B.K. Rutt, *Quantitative assessment of carotid plaque composition using multicontrast MRI and registered histology.* Magnetic resonance in medicine, 2003. **50**(6): p. 1199-1208.

273. Fan, Z., W. Yu, Y. Xie, L. Dong, L. Yang, Z. Wang, et al., *Multi-contrast atherosclerosis characterization (MATCH) of carotid plaque with a single 5-min scan: technical development and clinical feasibility.* Journal of Cardiovascular Magnetic Resonance, 2014. **16**(1): p. 53.

274. King, K., D. Xu, A. Brau, P. Lai, P. Beatty, and L. Marinelli. *A new combination of compressed sensing and data driven parallel imaging*. in *Proc., ISMRM, 18th Annual Meeting*. 2010.

275. Gibiino, F., S. Lechner‐Greite, T. Schirmer, V. Positano, A. Brau, J.A. Stainsby, et al., *Effects of inner volume field‐of‐view reduction on myocardial T2 mapping.* Journal of Magnetic Resonance Imaging, 2015. **42**(1): p. 175-179.

276. Degnan, A.J., A.J. Patterson, T.Y. Tang, S.P. Howarth, and J.H. Gillard, *Evaluation of ultrasmall superparamagnetic iron oxide-enhanced MRI of carotid atherosclerosis to assess risk of cerebrovascular and cardiovascular events: follow-up of the ATHEROMA trial.* Cerebrovascular Diseases, 2012. **34**(2): p. 169-173.

277. Patterson, A.J., T.Y. Tang, M.J. Graves, K.H. Müller, and J.H. Gillard, *In vivo carotid plaque MRI using quantitative T2* measurements with ultrasmall superparamagnetic iron oxide particles: a dose–response study to statin therapy.* NMR in Biomedicine, 2011. **24**(1): p. 89-95.

278. Haacke, E.M., Y. Xu, Y.C.N. Cheng, and J.R. Reichenbach, *Susceptibility weighted imaging (SWI).* Magnetic resonance in medicine, 2004. **52**(3): p. 612-618.

279. Wang, Y. and T. Liu, *Quantitative susceptibility mapping (QSM): decoding MRI data for a tissue magnetic biomarker.* Magnetic resonance in medicine, 2015. **73**(1): p. 82-101.

280. Warntjes, J., O.D. Leinhard, J. West, and P. Lundberg, *Rapid magnetic resonance quantification on the brain: Optimization for clinical usage.* Magnetic Resonance in Medicine, 2008. **60**(2): p. 320-329.

281. Ma, D., V. Gulani, N. Seiberlich, K. Liu, J.L. Sunshine, J.L. Duerk, et al., *Magnetic resonance fingerprinting.* Nature, 2013. **495**(7440): p. 187-192.